UNIVERSITY OF CALIFORNIA

SANTA CRUZ

HYDROGEN AND CARBON BEARING GEOMATERIALS AT NONAMBIENT CONDITIONS

A dissertation submitted in partial
satisfaction
of the requirements for the degree of

DOCTOR OF PHILOSOPHY

in

EARTH SCIENCES

by

Garrett Zeff

June 2024

The dissertation of Garrett Zeff
is approved:

_____
Professor Quentin Williams

_____
Professor Elise Knittle

_____
Martin Kunz PhD

_____
Peter Biehl
Vice Provost and Dean of Graduate Studies

Table of Contents

Abstract

Hydrogen and carbon bearing geomaterials at nonambient conditions

Garrett Zeff

Fractional crystallization of intermediate depth (~160-260 km), impact-induced magma oceans on Mars are examined. Residual liquids become denser than normal Martian mantle. Fractional crystallization near 3 GPa establishes inverted density distributions that can generate melt descent within the mantle. Liquid compositions produced by ~45-80 wt% crystallization become dense enough to descend to the core-mantle boundary (CMB) and could form a stably stratified thermochemical boundary layer (TCBL). If this layer crystallizes, its mineralogy would be dominated by either garnet and ferropericlase, or stishovite and ringwoodite. Although the size of Mars' core remains uncertain, the addition of such a thermal boundary layer would impede stabilization of (Mg, Fe)SiO_3-perovskite at the base of the mantle. A TCBL would both elevate the inferred temperature of the core and inhibit heat flow out of the core, with a potentially causal relation with the current lack of an internally generated Martian magnetic field.

A comprehensive analysis of experimental data and theoretical simulations on the partial molar volume of water in silicate melt indicates that finite strain theory successfully describes the compression of the H_2O component dissolved in silicate melt at high pressures and temperatures. However, because of the high compressibility of the water component, a fourth order equation of state fit is required to accurately simulate experimental results on water's volume in silicate melts at deep upper mantle,

transition zone and lower mantle pressures. Data from previous shock compression experiments on hydrous minerals in which melting occurs along the Hugoniot are used to provide an experimental constraint on the partial molar volume of water in silicate melt at deep mantle temperatures and pressures. The equation of state of the water component indicates that, depending on elastic averaging technique, the amount of water that could be present in neutrally or negatively buoyant mafic/ultramafic melts above the 410 km seismic discontinuity is upper-bounded at 5.6 wt%: smaller than previously inferred, and consistent with melt being confined to a narrow depth range above the 410 km discontinuity. If melt is predominantly distributed along grain boundaries in low aspect ratio films, extents of melting as low as 2% could produce observed seismic velocity reductions. The ability of the lowermost mantle to contain negatively buoyant hydrous liquids hinges on the trade-off between iron content and hydration: at these depths, substantially higher degrees of hydration could be present within partial melts.

The crystal structure and bonding environment of $K_2Ca(CO_3)_2$ bütschliite were probed under isothermal compression via Raman spectroscopy to 95 GPa and single crystal and powder x-ray diffraction to 12 and 68 GPa, respectively. A second order Birch-Murnaghan equation of state fit to the x-ray data yields a bulk modulus, $K_0 = 46.9$ GPa with an imposed value of $K_0' = 4$ for the ambient pressure-phase. Compression of bütschliite is highly anisotropic, with contraction along the *c*-axis accounting for most of the volume change. Bütschliite undergoes a phase transition to a monoclinic *C*2/*m* structure at around 6 GPa, mirroring polymorphism within

isostructural borates. A fit to the compression data of the monoclinic phase yields $V_0 = 322.2$ Å^3, $K_0 = 24.8$ GPa and $K_0' = 4.0$ using a third order fit; the ability to access different compression mechanisms gives rise to a more compressible material than the low-pressure phase. In particular, compression of the *C*2/*m* phase involves interlayer displacement and twisting of the [CO_3] units, and an increase in coordination number of the K^+ ion. Three more phase transitions, at ~28, 34, and 37 GPa occur based on the Raman spectra and powder diffraction data: these give rise to new [CO_3] bonding environments within the structure.

Raman spectra of $Na_2Ca_2(CO_3)_3$ shortite and $K_2Ca(CO_3)_2$ bütschliite were measured to 715°C and 740°C respectively, under vacuum. Shortite converts to nyerereite and calcite at 535°C. This assemblage is stable to ~700°C, where nyerereite begins to decompose. Bütschliite converts to isochemical fairchildite at 570°C. Fairchildite is stable to 665°C, where it decomposes to an assemblage of K_2CO_3 and CaO. The spectra of both fairchildite and nyerereite exhibit features consistent with extensive disordering.

Preface

Melting processes play many important roles in the evolution of rocky planetary bodies: chemical differentiation is enabled by extensive melting; crust formation occurs in the early stages of magma ocean crystallization (and can be accompanied by the formation of an early atmosphere), and cooling efficiency after chemical differentiation can significantly impact the geomagnetic properties of a planet. The Earth's present-day mantle geotherm lies far below the experimentally determined solidi of dry mantle rocks, and so it is perhaps not obvious that melting processes should persist in the mantle beyond an early magma ocean stage.

In the simplest terms, there are two ways to close the ~500 K gap between the geotherm and solidus: increase the temperature of the mantle or lower the melting temperature of the rocks. To a very good approximation the temperature gradient of the convecting mantle is adiabatic, and the solution to the differential equation $(\partial T/\partial P)_S = \gamma T/K_S$, where $\gamma = \alpha K_S/\rho C_P$ is the Grüneisen parameter and $K_S = -V(\partial P/\partial V)_S$ is the adiabatic bulk modulus, gives its trajectory in pressure-temperature space. In the absence of localized high temperature anomalies like mantle plumes, there is not much allowance for positive deviation from this trajectory. Plate tectonics, however, provides a very effective mechanism for depressing the melting temperature of mantle rock. Oceanic lithosphere remains stable on the surface of the Earth for up to ~180 million years, where it experiences extensive hydrothermal alteration and accumulates pelagic and sialic sediments, which host a variety of hydrous and carbonated mineral phases. Some of the sediments are scraped off to form an

accretionary wedge or prism in the subduction zone, and the remainder of the sediments are delivered into the mantle by the descending lithospheric slab, undergoing a series of dehydration and melting reactions that ultimately result in arc volcanism and mantle metasomatism; hydrated oceanic crust undergoes a similar sequence of reactions. The extent of devolatilization here is key, as it determines the amount of carbon and hydrogen available for flux melting deeper in the mantle. The stability of volatile bearing minerals and melts at high pressures and temperatures is therefore essential to understanding melting processes and chemical cycling in the deep Earth. Furthermore, H_2O and CO_2 substantially reduce melt density, and therefore act as effective controls on melt buoyancy, indicating that the fate of mantle derived melts (i.e., ascend, descend, or remain in place) depends strongly on their composition.

The cycling of carbon between the crust and mantle results in carbonatite volcanism at the Earth's surface. Carbonatitic melts differ from more common silicic melts in both structure and composition. Silicate melts are characterized by extensive polymerization of silicate tetrahedra, whereas carbonatites are essentially molten salts. Correspondingly, carbonatites have very low melting temperatures and viscosities: carbonatite lavas erupt at 500°C to 600°C and are less viscous than water. The only currently active carbonatite volcano is Oldoinyo Lengai, part of the East African Rift in the Arusha Region of Tanzania, which erupts natrocarbonatite lavas. These lavas are characterized by enrichment in Na, K, Ca and abundant crystallization of $Na_2Ca(CO_3)_2$ nyerereite and $(Na_2,K_2,Ca)CO_3$ gregoryite. Carbonatites are also frequently enriched in rare earth elements, which makes them important economic resources. Inclusions of

alkali carbonate minerals and quenched melts in mantle phases indicate that carbonate magmatism could play important roles in deep earth geological processes. Indeed, the identification of quenched carbonate melt along with the minerals eitelite ($Na_2Mg(CO_3)_2$) and bütschliite ($K_2Ca(CO_3)_2$) in a mantle-derived diamond suggests a genetic link between alkaline carbonate magmatism, diamond crystallization, and kimberlite petrogenesis.

Chapter 1 of this work is concerned with crystallization of impact-induced Martian magma oceans. Particular attention is given to the effects of water on the thermodynamic evolution of the melt/crystal system and the cooling history of Mars' core. Fractional crystallization of the magma oceans results in melts that are denser than coexisting solids. These dense melts sink to the base of the mantle and form a thermochemical boundary layer around the core. The absence of an internally generated magnetic field is explained in terms of the boundary layer. Chapter 2 continues in a similar vein and explores the effects of water on high-pressure melting in the Earth's mantle. Using data from previous experiments and simulations, models are formulated to quantify the effects of dissolved water on melt density as a function of pressure and the amount of hydrous melt in the low velocity layer overlying the Earth's mantle transition zone. Data from previous shock compression experiments on forsterite, enstatite, and serpentine are used to derive a value of the partial molar volume of water in silicate melts at very high pressures and temperatures. Chapter 3 marks a transition from calculational to experimental work: the high-pressure stability of the alkali-carbonate mineral bütschliite ($K_2Ca(CO_3)_2$) is explored via Raman spectroscopy and

synchrotron x-ray diffraction. High-pressure Raman spectroscopy measurements up to 94 GPa reveal extensive polymorphism, and the structure of the first high-pressure polymorph is solved via single crystal x-ray diffraction. High-temperature Raman spectroscopy measurements of shortite ($Na_2Ca_2(CO_3)_3$) and bütschliite ($K_2Ca(CO_3)_2$) are the focus of chapter 4. Upon heating, shortite undergoes two decomposition reactions: shortite first decomposes into an assemblage of nyerereite ($Na_2Ca(CO_3)_2$) and calcite, and then to a high-temperature polymorph of Na_2CO_3. Bütschliite converts to the high-temperature polymorph fairchildite before decomposing into an assemblage of K_2CO_3 and CaO.

Chapter 1: Fractional crystallization of Martian magma oceans and formation of a thermochemical boundary layer at the base of the mantle

1.1 Introduction

Magma oceans of varying depths, generated by heat from accretion and large impacts during early Martian history, have been widely invoked as having governed the early evolution of Mars (Reese & Solomatov, 2006; Elkins-Tanton et al., 2003). Elkins-Tanton (2012) generalized the work of Solomatov (2000) and proposed that cumulates resulting from the crystallization of a Martian magma ocean with an initially fully molten mantle could be gravitationally unstable, with denser material overlying less dense material, and ultimately overturning. This unstable density distribution results from a combination of enrichment of the liquids within the magma ocean in heavy elements (and particularly iron) as fractional crystallization progresses, Fe-Mg exchange in mafic minerals, and thermal expansivity. Bouvier et al. (2018) proposed that such a density instability and subsequent overturn in Mars' nascent mantle led to decompression melting, forming the planet's initial basaltic crust.

Beyond a possible mantle-wide magma ocean, there has long been the recognition that impacts during the later stages of planetary formation that were larger than later basin-forming events are likely to have melted variable depth ranges of the Martian mantle. Indeed, the anticipated size distribution of accreting objects indicates that multiple giant impact events were likely inevitable during Martian accretion (e.g., Agnor et al., 1999). Such events likely produced magma oceans that varied from localized to those that could have evolved to planetary-scale oceans accessing depths

of hundreds of km, or corresponding to roughly a quarter of the depth of the Martian mantle (Reese & Solomatov, 2006). On Earth, the prospective role of negatively buoyant melts at depth in the long-term differentiation of the planet has long been appreciated (e.g., Stolper et al., 1981; Lay et al., 2004). However, beyond early bulk melting of the entire Martian mantle, little attention has been paid to the possibility that partially differentiated dense silicate liquids arising from more limited impact-induced mantle melting could have been important for the evolution of Mars. Here, we examine the fractional crystallization behavior of intermediate depth magma oceans on Mars. Fractional crystallization is utilized as an endmember process because calculations on magma ocean crystallization processes indicate that melt-solid segregation is efficient at large solid fractions (>60% crystals), and fractional crystallization is expected to dominate for grain sizes greater than ~1 mm at lower solid fractions (Solomatov, 2007). Indeed, fractional crystallization has been previously deployed in probing the solidification behavior of a fully molten Martian mantle (Elkins-Tanton et al., 2003), and appears to be able to explain key aspects of lunar magma ocean solidification (Rapp and Draper, 2018). We document that residual liquids generated within magma oceans of limited depth extent ultimately become denser than normal Martian mantle, establishing unstable density distributions and generating melt descent within an evolving Mars. Specifically, we propose that fractional crystallization of local or intermediate depth magma oceans on Mars will produce Fe, Ca, and Al-enriched silicate liquids that are dense enough to descend to the core-mantle boundary (CMB) via diapiric down-welling, and could

form a stably stratified thermochemical boundary layer (TCBL) at the CMB. If this layer cooled sufficiently over Martian history to crystallize, its mineralogy would be dominated by either garnet and ferropericlase, or stishovite and ringwoodite, with changes in the descending liquid's bulk composition having only minor effects on the resulting phase assemblage. The presence of such a layer would reduce the likelihood of an (Mg, Fe)SiO_3-perovskite layer at depth in Mars, although such a TCBL would contain elevated amounts of $CaSiO_3$-perovskite. If present, a compositionally distinct thermal boundary layer at the base of the Martian mantle would substantially elevate the inferred temperature of the Martian core, and also impede heat flow from the top of the Martian core, with potential major implications for the current lack of an internally generated Martian magnetic field. Notably, this means for generating a TCBL is independent of possible lithospheric foundering/descent to the CMB induced by basin-forming impacts (Ruedas and Breuer, 2019). It also differs in its physical mechanism, but may have similar overarching effects as large impact-induced thermal perturbations in the Martian mantle generating possible causal links between impacts and cessation of the Martian dynamo (Lillis et al., 2008; Roberts et al., 2009).

We calculate possible seismic velocity anomalies that would be expected to arise from such a layer and find that the shift in mineralogy at depth should produce a seismic discontinuity that could prospectively be detectable by current or future Martian seismic deployments. As such, the eventual ability to resolve core-mantle boundary structures on Mars (such as have been observed on both Earth and the Moon) could either verify or falsify whether melts have occurred at great enough

depths and undergone fractional crystallization to produce negatively buoyant melts, and hence deep chemical stratification, within the Martian interior. Indeed, previous modeling of the deep Martian interior has generally assumed that the mantle is chemically homogeneous (e.g., Bertka & Fei, 1997; Khan & Connolly, 2008; Rivoldini et al., 2011; Khan et al., 2018; Samuel et al., 2019).

1.2 Modeling melting of the Martian mantle

The densities of silicate liquids were modeled with the third-order Birch-Murnaghan equation of state. We deployed two well-documented calculational packages, pMELTS and BurnMan (Ghiorso et al., 2002 and Cottaar et al., 2014, respectively), to model the Martian mantle and properties of the crystallizing magma ocean. While the pMELTS calibration is optimized for terrestrial mantle compositions, and its indiscriminate application to disparate chemistries can result in misleading analyses, Balta & McSween (2013) note, from an analysis of the applicability of pMELTS to Martian compositions, that "application of the pMELTS calibration to Martian mantle compositions is a fertile path for additional research." Correspondingly, while Burnman was originally constructed for applications to Earth's lower mantle, it has been updated to incorporate both terrestrial upper and lower mantle phases (and can treat iron-enriched phases, as occur within model Martian mineralogies).

BurnMan was used to calculate thermodynamic and seismic properties of the mantle for depths corresponding to pressures greater than 3 GPa. For calculational simplicity, the mantle was subdivided into seven mineralogically distinct layers, and

the Martian phase equilibria used is shown in Figure 1.1. The output from the pMELTS simulation was replicated as closely as possible within BurnMan to construct the uppermost layer of the model (i.e., 3 GPa). The Stixrude & Lithgow-Bertelloni (2011) mineral library was used to model the mantle phase assemblages in BurnMan. Gravity as a function of depth was computed self-consistently using BurnMan, with reference points taken from Zharkov & Gudkova (2005): our results are not particularly sensitive to modest variations in the gravity model. We modeled density for both a "hot" and "cold" (though hotter than present) primordial Martian mantle. The temperature at the top of the "hot" mantle adiabat was matched to the liquidus temperature at 3 GPa (1920 K) in a model Martian mantle, as derived from a pMELTS simulation. Reference temperatures in deeper layers were calculated from an adiabatic temperature gradient:

$$\left(\frac{\partial \mathrm{T}}{\partial \mathrm{P}}\right)_{\mathrm{S}} = \gamma \mathrm{T}/\mathrm{K_S} \tag{1.1}$$

where γ is the Grüneisen parameter, T is temperature in K, and K_S is the adiabatic bulk modulus in GPa.

For multi-hundred km depth magma oceans, we generated magmatic bulk compositions and mineralogy of the upper mantle by calculating the fractional crystallization of a bulk Martian composition taken from Elkins-Tanton et al. (2003), modified after Bertka & Fei (1997), where fO_2 was constrained along a QFM redox-buffer at 3 GPa (Table 1.1). Although typical estimates of Martian mantle compositions report total iron as Fe^{2+} (e.g., Dreibus & Wänke, 1984), the amount of

Fe^{3+} that is calculated for a Martian mantle assemblage is not negligible along a QFM buffer (Righter et al., (2010)), with significant amount of Fe_2O_3 distributed primarily into spinel (detailed mineral compositions, reported in wt% oxides, can be found in the our archived supplementary information).The presence of volatiles (H_2O + CO_2) within the volatile-bearing HM55 model depressed the liquidus temperature by 30 K. While estimates of redox conditions of Mars' mantle and its evolution over time are not well-constrained, we note that changes in fO_2 produce only minor changes in the composition of the magma ocean liquid as it crystallizes (Wadhwa, 2001; Herd et al., 2002; Righter et al., 2008; Udry et al., 2014). We focus our simulations on liquids at 3 GPa, or ~250 km depth, in the Martian interior; the trend of results at lower pressure indicate, in accord with the markedly larger compressibilities of melts relative to solids, that fractionated liquids at higher pressures than 3 GPa will be more likely to be negatively buoyant. Hence, our results are focused on impact events that are large enough to generate pervasive mantle melting at 250 km depth and below. Marinova et al. (2008) showed that for an impactor consistent with the Borealis Basin (i.e., 1600-2700 km in radius hitting obliquely at a speed of 6-10 km/s), melt is largely contained within the area of impact for at least the first 25 hours following the impact: it is unclear whether the melt ultimately globally redistributes (e.g., Reese & Solomatov, 2006). Accordingly, impactors during Martian accretion that are comparable in size to, or larger, than those associated with the formation of the Borealis Basin are those that are likely to generate the magma oceans of interest for this study.

The volatile abundance in such impact-generated magmas exercises a major effect on the depth of onset of negative buoyancy. Accurate constraints on the volatile concentrations in Mars' deep interior are difficult to derive. Crystallization of local magma oceans with H_2O + CO_2 concentrations less than 1 wt% can generate atmospheres with partial pressures of up to hundreds, or even thousands, of bars (Elkins-Tanton, 2008). Mars' current atmosphere (~6 mbar) is predominantly composed of CO_2 with only minor amounts of H_2O (10^{-3} mbar). Even the most rudimentary mass balance calculations of H_2O partitioning between the interior and atmosphere are complicated by the fact that early Martian atmospheres could have been effectively stripped away by large impacts and solar winds during the Noachian period (Jakosky & Phillips, 2001).

Figure 1.2a illustrates the density contrast between liquid and coexisting solids: unlike the terrestrial case, the onset of negatively buoyant magmas occurs at substantially lower pressures on Mars, primarily due to the higher iron content of the Martian mantle and the partitioning of iron into the liquids. Indeed, Ohtani et al. (1993) found the density crossover between olivine and a terrestrial peridotitic melt to occur at ~7 GPa. Figure 1.2b shows the density contrast between liquid and coexisting solid phases as a function of pressure for different extents of melting. Importantly, the curves do not represent isochemical compositions, as the liquid compositions depend on pressure. Each given point on a curve is derived from a single pMELTS fractional crystallization simulation carried out at a fixed pressure. A broad range of melt compositions become negatively buoyant in the depth range 170-

260 km. While pMELTS is not calibrated for pressures greater than 3 GPa, a simple extrapolation of Figures 1.2(a,b) indicates that at pressures between 3 and 4 GPa, a near 100 wt.% melt will become negatively buoyant relative to its coexisting solids. Since such a melt is isochemical with the solid mantle, descending melts that have not undergone fractional crystallization will not generate compositional or density anomalies upon recrystallization deeper in the mantle. The role of precipitating phases (Figure 1.2c) is of key importance: the density difference between precipitating solids and residual liquid for the volatile-bearing and volatile-free magmas do not increase monotonically as the liquid crystallizes. The inclusion of volatiles suppresses the negative buoyancy of liquids: while the inclusion of H_2O and CO_2 in the mantle composition neither notably affects the order nor composition of precipitating phases, nor the compressibility of the melts, it does markedly lower the low-pressure density of the liquids (Figure 1.3a). Indeed, a sufficiently volatile-rich melt will not sink directly to the CMB but will rather pool at a depth corresponding to ~14 GPa, where olivine transitions into wadleysite and ringwoodite (Figure 1.3). If the liquid undergoes further partial crystallization at this depth, the resulting density increase could push the residual liquid off of the density "shelf" associated with the $(Mg, Fe)_2SiO_4$ phase transitions and allow it to sink deeper into the mantle.

Figure 1.3a illustrates the density contrast of residual partial melts with respect to the Martian mantle density. This is in comparison to Figure 1.2 that shows the densities of a Martian magma ocean relative to the precipitating phases that appear during fractional crystallization. Figure 1.2 displays where solid phases

crystallizing in regions in which $\Delta\rho > 0$ will float to the top of a magma chamber. So, Figure 1.2 illustrates where melts are negatively buoyant within the magma chamber, and Figure 1.3 shows the conditions in which they descend in the mantle. The change in melt compositions between Figures 1.2 and 1.3 reflects the fact that the respective maxima of $\Delta\rho$ and ρ_{liquid} occur at different extents of melting. Two Martian mantle density profiles are shown in Figure 1.3a, one reflecting an earlier, hotter Mars, and the other reflecting a possible recent areotherm. The two curves reflect the tradeoffs between the volumetric effects of thermal expansion and adiabatic compression. The volumetric effects of thermal expansion on the solid mantle, even for moderate temperature increases, become smaller around 10 GPa. Hence, as long as the mantle is solid, the negative buoyancy of the melts seems to be largely independent of the temperature of the mantle.

A total of 8 unique TCBL assemblages are shown in Figure 1.3(b-f). Two normative mineralogies for the solidified TCBL were examined for compositions corresponding to four different degrees of fractional crystallization (55, 40, 30 and 20% residual liquid; the maximum liquid-solid density difference for the volatile-bearing composition occurs at 55 wt% liquid). All of the solidified assemblages contain varying amounts of majoritic garnet, $CaSiO_3$-perovskite, and ferropericlase near the Martian CMB. However, substantial ringwoodite and stishovite were preferentially crystallized in Assemblage 1, while majoritic garnet dominated in Assemblage 2 (Table 1.2): the pervasive coexistence, and hence close stability ranges, of ringwoodite and majorite in the deep Martian mantle has long been recognized

(e.g., Bertka and Fei, 1997). Whether a ringwoodite or majorite-garnet dominated assemblage should be stabilized for our liquid compositions at the Martian CMB is unclear. The boundary between ringwoodite- and majorite-dominated assemblages occurs near 7 mole % Al_2O_3 in the $Mg_4Si_4O_{12}$-$Mg_3Al_2Si_3O_{12}$ system (Akaogi et al., 2002). Increases in iron content appear to modestly expand the ringwoodite-dominated field (Ohtani et al., 1991), and changes in temperature do not appear to greatly affect the transition (Akaogi et al., 2002). This ambiguity in the deep mantle phase equilibria for compositions close to that of the bulk Martian mantle has been previously recognized (Verhoeven et al., 2005), and we thus report the elastic properties of both ringwoodite-dominated (Assemblage 1) and majorite-dominated (Assemblage 2) assemblages for our crystallized liquid compositions.

Figure 1.3 shows the shift in density and P- and S-wave velocities across a ~150 km thick TCBL layer with a 500 K superadiabatic temperature change: for this magnitude of temperature change and depth, self-compression and thermal expansion almost entirely tradeoff, with thermal expansion having a slightly larger effect. Importantly, the thickness of the TCBL in Figure 1.3 is intended to be illustrative: the thickness of such a layer would hinge on the number and size distribution of impactors that produced magma oceans of limited depth extent within the Martian mantle, as well as the efficiency of melt drainage from such crystallizing magma oceans. The 150 km thickness we illustrate assumes that the TCBL forms a uniform thin spherical shell around the core, and is derived from descent of ~30% melt from a layer between 150 and 275 km depth. Given the uncertain impact history of Mars, we

do not preclude that a Martian TCBL layer could be thinner or thicker than that shown in Figure 1.3: we simply note that if such a layer is ultimately observed, its thickness will provide insight into the amount (and possible average chemistry) of such descending melts. Our choice of 500 K for the temperature jump across this layer is also not well-constrained, but a gradient of near 3 K/km is in general accord with simple boundary layer theory (McKenzie et al., 1974) for a core heat flux of order 10 mW/m^2 (Sandu and Kiefer, 2012). The shift in density across the TCBL layer is modulated by the magnitude of the temperature jump across the layer.

Because the melt-generated TCBL compositions are enriched in iron (and, at these depths, also $CaSiO_3$-perovskite), the density contrast associated with this possible basal layer is substantial: depending on mineralogy and degree of fractional crystallization, density increases associated with the TCBL lie between 3 and 11% (Figure 1.3d). Therefore, the buoyancy number (the ratio of chemical to thermal buoyancy) is expected to be substantially greater than 1, and entrainment of the layer (regardless of mineralogy or level of fractional crystallization) within overlying Martian mantle convection is thus not anticipated (e.g., Tackley, 1998). Notably, the expected velocity contrasts (Fig. 3c, d) at the top of the layer are uniformly negative, largely because of the enhanced density of the layer: decreases of -1 to -7% are anticipated for compressional wave velocity, and -1 to -10% for shear velocities. As an important aside, these velocity structures are calculated for a fully solidified TCBL. If such a deep, iron-enriched thermal boundary layer exists, it is distinctly possible that the lower portion of such a layer may not have fully solidified over

Martian history: this depends critically on the temperature increase across the layer, and thus the thermal state of the Martian core. If the basal region of the layer remains molten, then a more complex velocity structure (with a deeper negative velocity discontinuity) would be anticipated.

The impedance contrasts that we calculate for a solidified melt-generated TCBL (Figure 1.3e, f) are highly dependent on the mineralogy of the layer: in this instance, the high densities of the garnet-dominated assemblages actually generate impedance increases across the TCBL boundary. The shear wave impedance contrasts (which are of the order of ±8% for the two possible mineralogies) could prospectively generate (depending on the size of Martian seismic sources) seismic reflections that could be detected with current or future Martian seismic deployments. Based on the core model of Khan et al. (2018), the transition from the boundary layer to a fluid core would be accompanied by a 100% reduction in S-wave velocity and impedance, a 45% to 48% decrease in P-wave velocity, a 34% to 45% increase in density, and an 18% to 38% decrease in P-wave impedance.

1.3 Possible implications of a TCBL for the Martian dynamo

Convection in the core is a necessary, but not sufficient, condition for a planet's ability to sustain a dynamo. Put more restrictively, a dynamo cannot be sustained if there is not sufficient heat flow out of the core (compositional buoyancy as a dynamo driver typically relies on core crystallization, which also hinges on heat removal from the core (e.g., Suehiro et al., 2017). Core crystallization can help to drive convection through buoyancy forces generated at the crystallization front (Lay

et al., 2008). However, although the presence of an inner core on Mars is not precluded, current thermal models suggest that the core of Mars is entirely molten (e.g., Breuer et al., 2010). Therefore, heat flow into the mantle is likely the main driver of core convection and, by extension, the dynamo. While core convection may persist with a subcritical Rayleigh number (Stanley & Glatzmaier, 2010), it is generally assumed that dynamo activity ceases once driving forces weaken enough that the Rayleigh number becomes subcritical. Therefore, if the core is only weakly convecting with a loss of heat predominantly through conduction, small perturbations in temperature or composition could cause the dynamo to cease. However, if the core is convecting vigorously and heat flow out of the core is substantial, there could be a substantial prospect for dynamo generation.

A number of models, ranging from early rapid heat transport associated with plate tectonics to impact-induced shock heating of the core, have been put forward to explain the initiation and early cessation of a Martian dynamo (e.g., Nimmo & Stevenson, 2000; Arkani-Hamed & Olson, 2010). The mechanism we propose differs from, but is complementary to, that proposed by Roberts et al. (2009), in which thermal perturbations in the mantle associated with impacts end the dynamo. The generation of a magmatically-induced, compositional boundary layer at Mars' CMB would establish a wider depth range conductive boundary layer on the mantle side of the core-mantle boundary. The existence of large thermal boundary layers at both the base and surface of the mantle would, because of the presence of multiple thermal boundary layers, result in a core that is hotter than inferred from models with a single

boundary layer. Since heat flow is driven by temperature differences, heat flow out of the core would be decreased compared to a completely convective deep Martian mantle that is juxtaposed directly with the core absent a compositionally distinct boundary layer. The precise effects of such a layer on heat flow from the core are difficult to assess, since it is unclear whether this layer would currently be solid, liquid or partially molten; what is clear is that at its onset, it would be molten. Simple scaling relations (e.g., Labrosse, 2002), $q \propto Ra^{.25}\Delta T$, indicate that the flux across a conductive bottom boundary layer is proportional to the change in temperature across the layer. In the case of a molten or partially molten basal layer, internal convection within this hot, low-viscosity layer might be anticipated, and hence the bulk of the temperature rise associated with a core-mantle temperature contrast could be elevated to the top of the compositionally distinct molten zone/bottom of the solid mantle (e.g., Lay et al., 2004). In this scenario, the heat flux from the core could be reduced dramatically when a melt layer initially forms at the CMB, and the subsequent heat flow history modulated by the solidification and convective history within the compositionally distinct basal mantle layer. In passing, we note that partially molten zones overlying the core-mantle boundary have been proposed to be present on both Earth and the moon based on seismic data (e.g., Williams & Garnero, 1996; Weber et al., 2011). If a compositionally distinct layer is present on Mars, the present-day core heat flow will be governed by whether it is fully solid (as was assumed in Figure 1.3) or not, and whether the TCBL might internally convect: as such, if such a layer exists, the heat flow conditions at the Martian CMB will critically hinge on its physical and

dynamic state, which ultimately may be illuminated by Martian seismic measurements. Therefore, the expectation is that the early generation of a TCBL will reduce heat flow from the Martian core. Moreover, if a TCBL exists that is generated from impact events involving limited melting of the mantle, deep sequestration of radiogenic elements, as invoked to occur within a separate geochemical reservoir within the deep Martian mantle by Kiefer (2003), could also occur. Such radiogenic internal heating of a deep mantle layer could similarly reduce the heat flow out of the Martian core.

There are also implications of a deep TCBL for bulk planetary structure. If the core temperature is hotter than previously inferred, more mass would be needed at depth to match the moment of inertia and mean density. This shift in the concentration of mass within the Martian interior could manifest itself via a larger core, smaller amounts of light alloying components within the core, and/or the enrichment of iron in lower mantle phases. From the perspective of mantle mineralogy, we do not preclude that an early, primordial perovskite layer, stabilized by a hotter Martian interior and the negative Clapeyron slope of the perovskite transition, could have complex dynamic interactions with our postulated deep melt-derived layer, as Mars undergoes secular cooling and any perovskite layer thins through time. A detailed treatment of such effects on the chemistry and mineralogy of the core and mantle is beyond the scope of this paper.

1.4 Implications of a TCBL for geodynamics and volcanism

Mantle plumes have been commonly invoked as sources for volcanism (and particularly the Tharsis rise) and the northern-southern hemisphere crustal dichotomy on Mars. The interplay between deep mantle structure and the genesis and stability of plumes on Mars has been extensively probed (e.g., Weinstein, 1995; Harder & Christensen, 1996; Wenzel et al., 2004; Zaranek & Manga, 2007; Sekhar and King, 2014), although such an interplay has not been uniformly accepted as important (van Thienen et al., 2006). Harder & Christensen (1996) and Weinstein (1995) demonstrate that a phase transition at the base of the mantle can focus multiple upwellings into one or two plumes. Wenzel et al. (2004) and Zaranek & Manga

(2007) suggest that a gravitationally stable layer at the base of the mantle (generated as a result of crystallization of a mantle-wide magma ocean: Elkins-Tanton, 2003) could provide a relatively fixed locus for plumes and hence for long-lasting localized volcanism. In particular, Zaranek and Manga (2007) found that the density differences required to keep layers stable for a variety of thicknesses and heat productions were less than those predicted by bulk magma ocean crystallization and overturn, demonstrating in accord with our simple buoyancy number analysis that dense layers are unlikely to be entrained within the Martian mantle. Our results provide a mechanism through which a deep, chemically distinct mantle layer could be generated that would both be stable through Martian history, and potentially contribute to plume stability.

1.5 Conclusions

Fractional crystallization of impact-induced magma oceans that access depths of ~250 km and deeper in the Martian mantle were modeled. Fractional crystallization of such liquids results in negatively buoyant melts that could descend to the core-mantle boundary of Mars, producing an iron, calcium and incompatible element-enriched thermochemical boundary layer. The likely thickness of such a chemically distinct layer is unclear, but as one example, we present the effects on seismic velocity and impedance of a 150 km thick thermochemical boundary layer at the CMB of Mars. If such a layer fully solidifies over Martian history, the shear and compressional wave velocities should each decrease at the top of the layer: the magnitude of the prospective discontinuity is such that it could prospectively be most

readily detected in shear wave studies. Such a layer, as an impediment to heat flow from the core, could play a role in the present lack of a Martian dynamo and, as a dense basal layer, potentially contribute to the fixity of mantle plumes on Mars.

A TCBL generated via melting associated with smaller (but still planet-disrupting) impactors provides a means by which deep stratification could be generated within the Martian interior that is complementary to stratification that could emerge from whole-mantle melting (e.g., Elkins-Tanton, 2003). Our results imply that the high iron content of the Martian mantle could generate a different style of magmatically-induced deep mantle stratification from the other terrestrial planets: for example, larger, less iron-enriched bodies such as Earth and Venus could trap fractionated melts within their transition zone (e.g., Sakamaki et al., 2006): for these bodies, either mantle-wide melting or lower mantle magmatic differentiation may be required to generate a TCBL (Lay et al., 2004; Labrosse et al., 2007). For comparison, the low pressures and possibly lower iron content of the mantle of Mercury (vander Kaaden & McCubbin, 2015) would limit negatively buoyant melts on this body to highly iron-enriched, extremely fractionated liquids.

Acknowledgments

BurnMan scripts, pMELTS output files, and plotting data used in this work can be found at https://doi.org/10.7291/D1CM1M.

Chapter 2: Thermoelasticity of water in silicate melts: Implications for melt buoyancy in Earth's mantle

2.1 Introduction

Although water is present in relatively low abundance in Earth's mantle compared to the major rock-forming oxides, it plays a critical role in the evolution of Earth's silicate interior. Water facilitates basalt petrogenesis at hot spots and mid-ocean ridges via melting point depression of peridotite in the upper mantle (e.g., Hirth and Kohlstedt, 1996); acts as a control on the density driven transport of magmas; and in its fluid phase can act as a metasomatizing agent, redistributing incompatible elements throughout the mantle and crust. While the effects of water are perhaps most conspicuous at shallow depths, there are indications that water contributes significantly to the structure of the deeper silicate Earth as well. Seismological studies have identified the presence of a regionally observed, but unlikely to be ubiquitous, low velocity layer (LVL) above the 410 km mantle transition zone (MTZ) discontinuity (e.g., Revenaugh and Sipkin, 1994; Song et al., 2004; Tauzin et al., 2010; Wei and Shearer, 2017). And, indeed, a general consensus has emerged from seismic, mineralogic and geodynamic analyses that this velocity anomaly is associated with the presence of potentially hydrated partial melt (Revenaugh and Sipkin, 1994; Nolet and Zielhuis, 1994; Matsukage et al., 2005; Sakamaki et al., 2006; Leahy and Bercovici, 2007; Bagley et al., 2009; Jing and Karato, 2012; Freitas et al., 2017). Deeper still, at the base of the lower mantle, hydrogen enrichment in the D'' layer has been invoked as a possible control on the eutectic temperature of silicates near the core mantle

boundary (CMB), prospectively generating partial melting within the mantle's basal layer (e.g., Lay et al., 2004; Du et al., 2019).

Experimental investigations of the thermoelastic properties of water dissolved in silicate melts date back to at least the early 1970's, as illustrated by the pioneering furnace-heated compression studies of hydrous albite melt (Burnham and Davis, 1971; B&D71 hereafter). A broad suite of later studies, summarized in Table 2.1, have sampled diverse melt compositions and utilized a variety of experimental techniques to probe hydrous silicate liquids under compression, including X-ray absorption, Brillouin spectroscopy, relative density comparisons (the "sink/float" technique), and low-pressure dilatometry of hydrous melts and glasses near the glass transition. And, at deep lower mantle/outer core pressures, there are a few shock Hugoniot data on possible melts of a hydrous phase. Advances in computing over the past few decades have resulted in the introduction of numerical methods, with first principles molecular dynamics (FPMD) also providing substantial insights into the properties of hydrous silicate melts at high pressures and temperatures. These simulations employ molecular dynamics to sample the configuration space of a dynamically evolving system whose total energy is calculated from potentials generated by quantum mechanical methods (Stixrude, 2001).

Although the pressure-dependence of the volume of water dissolved in silicate melts has been the focus of studies that deployed results derived from subsets of these experimental probes (e.g., Ochs and Lange, 1999; Tkachev et al., 2005; Malfait et al., 2014a; Ueki and Iwamori, 2016; Sakamaki, 2017), there does not yet appear to have

been a comprehensive analysis of the entire $\bar{v}_{H_2O}$ (partial molar volume of water in silicate liquids) dataset as a function of pressure and temperature. Additionally, a substantial portion of the conditions relevant to Earth's interior are largely unconstrained by experiments on hydrous silicate liquids, and hence inferences about the value of the volume of water in melts hinges on theoretical simulations under these extreme conditions. Indeed, there are both experimental and theoretical indications that the structural role of hydroxyl units/water within silicate melts may shift markedly at high pressures (Closmann and Williams, 1995; Mookherjee et al., 2008): whether these structural shifts substantially impact the thermoelastic properties of silicate liquids (or those of the constituent hydrous component within the liquids) is unclear. Moreover, whether there are shifts in the speciation of water between hydroxyl units and water molecules, as has been documented to occur at modest pressures as a function of water content (e.g., Stolper, 1982), is also not certain, although FPMD simulations strongly indicate that the hydroxyl unit (at times present in extended structures: Mookherjee et al., 2008; Bajgain et al., 2019) is the dominant means of sequestration of water within hydrous melts at mid-upper mantle pressures and higher. Thus, the central goals of this study are:

1) Analyze the available data and formulate a thermodynamically consistent and statistically robust model for describing the effects of compression and high temperature on the thermoelastic properties of water dissolved in compositionally diverse silicate melts. And, determine whether there is any

resolvable compositional dependence of the volume of water dissolved in silicate melts under compression and, if so, characterize it.

2) Incorporate and recalculate experimentally determined constraints (from previous shock compression experiments, but incorporating newer experiments on anhydrous compositions) on the partial molar volume of the dissolved water component in silicate melts at the high pressures and temperatures of the deep mantle. Here, the thermal expansion of the water component at the extreme conditions of Earth's deepest mantle is of particular interest.

3) Evaluate the degree to which the partial molar volume of water dissolved in silicate melts may differ from the volume of fluid water: the two values have been hypothesized to be nearly equivalent at high pressures (e.g., Malfait et al., 2014a), which would imply that the volume of mixing of water into silicate melts is near zero.

4) Most importantly, deploy our integrated results on the effect of water on silicate melt density and derive constraints on the formation and composition of possible melts that could explain the seismically observed properties of the LVL above the MTZ and ultra-low velocity zones (ULVZs) at the base of Earth's mantle. In particular, our goal is to determine both the possible and likely ranges of water contents of magmas at these depths that are compatible with current seismic observations. As we show, an accurate assessment of potential water contents in deep, partially molten zones in Earth's mantle hinges on constraints

on both higher order elastic constants associated with dissolved water, and thermal effects on water mixing in silicate melts.

2.2 Review of the $\bar{v}_{H_2O}$ data

The studies of Bouhifd et al. (2015) and Ochs and Lange (1997, 1999; O&L97, 99 hereafter) comprise the data set of ambient pressure $\bar{v}_{H_2O}$ measurements. Bouhifd et al. (2015) determined $\bar{v}_{H_2O}$ in albite, tephrite, trachyte, foidite, and phonolite glasses and melts with up to 11 mol% water between 300-1050 K: this temperature range exceeded the glass transition temperature in these compositions, and hence provided a measurement of the volume of water within a metastable hydrated liquid regime at ambient pressure. O&L97 similarly determined $\bar{v}_{H_2O}$ in albite melt with 2-6 wt% water between 500-770 K, while O&L99 determined $\bar{v}_{H_2O}$ in rhyolite and KCS (K_2O-CaO-SiO_2) melt with up to 6 wt% water between 450-1100 K. Each of these studies resolved no compositional dependence of $\bar{v}_{H_2O}$ or its temperature derivative at 1 bar. Relative uncertainties in $\bar{v}_{H_2O}$ for these experiments are between 1-2% (~0.4 cm^3/mol).

B&D71 and Tkachev et al. (2005) presented fits to their measurements (volumes and Brillouin-derived moduli/volumes, respectively) under compression to 1 and 6 GPa, respectively; we report their isotherms and evaluate their compatibility with fits to the discrete volumetric determinations. B&D71 employed a furnace-heated bellows compression technique, in which pressure was read from a handheld gauge, to determine $\bar{v}_{H_2O}$ under pressure in albite melt with 11 wt% water. B&D71 report uncertainties in pressure less than 0.01 GPa and uncertainties in volume of 0.8 cm^3/mol (3-5%). Tkachev et al. (2005) determined $\bar{v}_{H_2O}$ in an extensively depolymerized

hydrous sodium-disilicate liquid containing 46 wt% water. We utilize their 457 K isotherm between 0 and 6 GPa. Higher temperature measurements were made in their experiments, but pressure-volume data are not available for these. A notable aspect of the current data sets is the variability in the estimates of the ambient pressure volume of $\bar{v}_{H_2O}$: for the experiments, this value varies from ~23-28 cm^3 at ca. 1200 K (Figure 2.1, star symbols). As is discussed below, this variability/uncertainty in the zero-pressure volume results in a direct and critical trade-off between the zero-pressure volume and the elasticity inferred for water in silicate melts under compression. Larger values of the zero pressure volume typically result in smaller fit values of the bulk moduli, yielding a more compressible dissolved water component.

X-ray absorption experiments have been conducted on rhyolite, andesite, peridotite and phonolite melts with 5-10 wt% water (Malfait et al., 2014a, 2014b; Sakamaki et al., 2009; Seifert et al., 2013). These measurements span pressures and temperatures of 0-4 GPa and 1200-2000 K. Uncertainties in volume range from 5-30% (1.0-3.5 cm^3/mol) and uncertainties in pressure range from 1-12% (~0.01-0.10 GPa), depending on the data set. While Malfait et al. (2014b) suggest that $\bar{v}_{H_2O}$ could exhibit a compositional dependence at higher pressures, none of the data from X-ray absorption experiments require a strong compositional dependence of $\bar{v}_{H_2O}$: we also assess this hypothesis in greater detail. The highest pressure and temperature static experimental data come from sink/float experiments. All of the melts in the sink/float experiments contained iron (FeO) and range in composition from mid-ocean ridge basalt (MORB) to Fe-rich ultramafics (Sakamaki et al., 2006; Agee, 2008a,b) and close-to-eutectic

melts of peridotite (Jing and Karato, 2012; Matsukage et al., 2005). The MORB melts contained 2 and 8 wt% water and $\bar{v}_{H_2O}$ was determined at 17 and 20 GPa (both at 2473 K). The ultramafic melts varied in water content between 2-7 wt% and experiments were conducted at pressures and temperatures from 2-15 GPa and 1773-2473 K. Uncertainties in volume vary between 8-25% (0.6-2.0 cm^3/mol) and uncertainties in pressure vary between 4-25% (0.5-1.0 GPa).

The preponderance of static compression data hence lie below 6 GPa, and comparatively few sink-float points access transition zone pressures (Figure 2.1). Indeed, the maximum pressure of 20 GPa achieved in the static compression experiments corresponds to a depth mid-way into the MTZ or ~575 km total depth. The bottom of the transition zone at ~660 km depth delineates the boundary between the bottom of the upper mantle, where majorite and ringwoodite are the predominant (Mg,Fe)-silicate phases, and the lower mantle, where bridgmanite and ferropericlase are the most abundant mineral phases. Because of the current pressure limitations of the static experiments, the FPMD simulations therefore provide primary constraints on the dissolved water component of hydrous silicate melts at conditions relevant to Earth's lower mantle. We incorporate data from six different FPMD simulations on hydrous basalt, jadeite, primitive mantle eutectic-like, $(Mg,Fe)SiO_3$ and $(Mg,Fe)_2SiO_4$, and pyrolite melts (Bajgain et al., 2015, 2019; Du et al., 2019; Mookherjee et al., 2008; Karki et al., 2021; Solomatova and Caracas, 2021). Water contents and major oxide bulk compositions in FPMD simulations are determined exactly, *ab initio*, by definition of a supercell (~10^2 atoms). The melts in the FPMD simulations are typically annealed

at very high temperatures (1000's of K above T_{Melt}) to ensure thermodynamic equilibrium, and then are typically cooled to lower temperatures. The (Mg,Fe)-silicate and pyrolite melt simulations at 2000 K from Karki et al. (2021) and Solomatova and Caracas (2021) include the lowest temperature simulations of the FPMD dataset that we consider. There is thus overlap in temperature between the hottest experimental measurements (2473 K from Sakamaki et al., 2006) and the FPMD studies of Bajgain et al. (2015); Karki et al. (2021); and Solomatova and Caracas (2021). For the FPMD simulations, the quoted uncertainties in the volume of the H_2O component range from 1-21%; uncertainties in pressure, associated with the equation of state, typically vary from less than 1 to 20%.

Recently, Yuan et al. (2020) conducted simulations on hydrous Mg_2SiO_4 melt with water contents between 6-27 wt%. The melts in their study were annealed at 8000 K and then quenched to 1800 K and 2200 K: the lower of these temperatures closely approaches the experimental solidus. At 1 bar and 1800 K, Yuan et al. (2020) report $\bar{v}_{H_2O} = 15.53$ cm^3/mol, and the bulk modulus and its pressure derivative of the water component as $K_{0,T} = 13.34\ GPa$, and $K'_{0,T} = 3.62$. This suggests a dissolved water component that has a substantially smaller initial volume and is stiffer than is reported in other experimental and theoretical studies. For comparison, Tkachev et al. (2005) determined $\bar{v}_{H_2O} = 13.60\ cc/mol$ and $K_{0,T} = 4.30\ GPa$ at 1 bar and a substantially lower temperature of 460 K for the bulk modulus of water in the melt, and Malfait et al. (2013) report $\bar{v}_{H_2O} = 20.60$ cm^3/mol, $K_{0,T} = 4.60\ GPa$, and $K'_{0,T} = 5.50$ at 1 bar and 1673 K. Yuan et al. (2020) observed a homogenous liquid phase for the entirety of

their simulations, but they also note that this does not ensure that the liquid phase was in thermodynamic equilibrium. Because these results closely approach the solidus, deviate towards notably stiffer and denser properties of the water component relative to both experimental and other theoretical studies, and might not be in thermodynamic equilibrium, these FPMD results are excluded in the equation of state fits that we conduct. Nevertheless, it is possible that these lower temperature simulations may represent an outlier in the trade-off between $\bar{v}_{H_2O}$ and $K_{0,T}$ for the partial molar volume of water under compression.

2.3 Constraints from shock melting of minerals in the system SiO_2-MgO-H_2O

Serpentine (srp) is a magnesium phyllosilicate commonly formed from the hydrothermal alteration of olivine (Mg-endmember forsterite; fo) and pyroxene (Mg-endmember enstatite; en), and its Mg-endmember varieties antigorite, chrysotile, and lizardite accommodate ~13 wt% water in their crystal structures. Here, we calculate the partial molar volume of water ($\bar{v}_{H_2O}$) in srp melt at deep mantle pressures using Hugoniot data from previous shock compression experiments that accessed an apparently molten state (Tyburczy et al., 1991). These calculations augment those conducted originally by Tyburczy et al. (1991), as they are enabled by more recent shock measurements of forsterite and pyroxene (Akins et al., 2004; Mosenfelder et al., 2007; 2009). Accurate extraction of $\bar{v}_{H_2O}$ values from the shock data is contingent upon three suppositions. First, the system SiO_2-MgO-H_2O is assumed to mix linearly with respect to volume. That is, $\bar{V}_{Total} = \sum_i \chi_i \bar{v}_i$, where χ_i and $\bar{v}_i$ are the mole fraction and partial molar volume of component *i*: this assumption has long been recognized to hold

for most components of silicate liquids at ambient pressure (e.g., Lange and Carmichael, 1987). Second, the composition of srp and its isochemical melt is expressed in terms of fo, en, and H_2O components:

$$Mg_3Si_2O_5(OH)_{4\ (srp)} = MgSiO_{3\ (en)} + Mg_2SiO_{4\ (fo)} + 2H_2O \qquad (2.1)$$

Finally, a transition to a dense melt phase has been inferred along each of the en, fo, and srp Hugoniots around 150-200 GPa and ~5000 K (Akins et al., 2004; Mosenfelder et al., 2007, 2009; Tyburczy et al., 1991). With these conditions satisfied, it follows that the partial molar volume of water in serpentine melt can be expressed linearly in terms of the total molar volumes of the shock generated en, fo, and srp melts when corrected to isothermal conditions:

$$\bar{v}_{H_2O} = \frac{1}{2}(\overline{V}_{srp} - \overline{V}_{en} - \overline{V}_{fo}) \qquad (2.2)$$

Thus, Hugoniot pressures for each composition were thermally corrected to isotherms and $\bar{v}_{H_2O}$ evaluated at common pressures. The pressure correction from the Hugoniot to an isotherm is $P_{Isotherm} = P_{Hugoniot} + \left(\frac{\partial P}{\partial T}\right)_V \Delta T$, where $\left(\frac{\partial P}{\partial T}\right)_V = \alpha K_{T,0} = \gamma \rho C_V$ is the thermal pressure; α is the coefficient of thermal expansion; K_T is the isothermal bulk modulus; γ is the Grüneisen parameter; ρ is density; C_V is the isochoric heat capacity, and $\Delta T = T_{Isotherm} - T_{Hugoniot}$. We calculated a series of regularly spaced isotherms for the silicates in Equation 1 between 1000 K and 6400 K. The shock isotherms we calculate are in general agreement with the FPMD data at the initial pressure of each isotherm, but they display substantially greater compressibility with increasing pressures (Supplement 1). This may be a reflection of uncertainties in the EOS slope

within the highest pressure phase along the serpentine Hugoniot (which has been associated with melt: Tyburczy et al., 1991). The serpentine Hugoniot has neither been characterized to as high pressures nor with comparable data density as those of enstatite or forsterite: the properties of its highest pressure, molten phase are dictated by only a few Hugoniot points, and hence its EOS slope (as opposed to its general density) is not well determined. In Figure 2.1, we plot an approximate isochor ($\bar{v}_{H_2O} = 5.57 \pm 0.03$ cm^3/mol) between 1000 and 6400 K and 114-144 GPa, derived from the initial pressure-volume points from each isotherm. Pressures and volumes are evaluated at temperature steps of 200 K. The primary goal of this calculation is to provide an experimental constraint on $\bar{v}_{H_2O}$ at deep lower mantle pressures; the phase equilibria and sparse data of the silicates of Equation 1 in a molten regime preclude deploying a standard shock wave equation of state by previously established methods (Jeanloz, 1989; Ahrens, 1993), since melting only occurs at the highest pressures probed to date along the Hugoniot of serpentine. Because of the limited data availability, further experiments on the Hugoniots of both hydrous and corresponding anhydrous silicates would improve the current constraints on the thermoelastic properties of water in silicate melts at the high pressures and temperatures of Earth's lowermost mantle. Nevertheless, our shock-derived isochor of water in srp melt is in relatively good

accord with volumes of water in silicates from FPMD simulations under comparable conditions (Figure 2.1).

2.4 Equations of state and thermal expansion of the dissolved water component: Comparison with liquid water

A principal challenge in fitting these data is illustrated in Figure 2.1: the typical magnitude of volumetric compression of the H_2O component in silicate melts in the 0 to ~100 GPa range is approximately four-fold. Compressions of this magnitude have typically been challenging for standard equations of state: higher order terms than are usually deployed are often required to accurately treat data that span such large strains. Nevertheless, equations of state derived from both finite strain theory (the Birch-Murnaghan EOS) and a binding energy/potential-associated formulation (the Vinet EOS) have each previously been used to model compression of the dissolved water component in silicate melts (e.g., Malfait et al., 2014a,b; Sakamaki, 2017). A key observation here is that, for deep mantle applications, the fourth order terms of these equations of state appears to be critical for modeling compression of the H_2O component in a portion of the experimental studies. Previous modeling of the experimental data has been at the second and third order level, while some of the FPMD studies have employed fourth order equations of state.

We apply both the equations of state of Birch (1978) and Vinet et al. (1987) to the present dataset. Birch's description of finite strains is rooted in Eulerian continuum mechanics, and we consider here two forms of the EOS commonly seen in geophysics: the third order Birch-Murnaghan equation of state:

$$P = \frac{3K_{0,T}}{2}(X^{-7} - X^{-5})[1 + \frac{3}{4}(K'_{0,T} - 4)(X^{-2} - 1)] \quad (2.3)$$

and the fourth order Birch-Murnaghan equation of state:

$$P = \frac{3K_{0,T}}{2}(X^{-7} - X^{-5})\left[1 + \frac{3}{4}\left(K'_{0,T} - 4\right)(X^{-2} - 1) + \frac{1}{24}\left(9K'^{2}_{0,T} - 63K'_{0,T} + 9K_{0,T}K''_{0,T} + 143\right)(X^{-2} - 1)^2\right] \quad (2.4)$$

where $X = (V/V_0)^{1/3}$. Vinet deploys a "universal" relationship between binding energies and interatomic distances, derived via a Rydberg potential. The so-called "Vinet" equation of state is formulated as

$$P = 3K_{0,T}\frac{(1 - X)}{X^2}exp[\eta(1 - x)] \quad (2.5)$$

where $\eta = \frac{3}{2}(K'_{0,T} - 1)$. To discretize fitting the equations of state across different thermal regimes and data types, we split the data into experimental and FPMD subsets, and then binned each subset within different temperature ranges (Figure 2.2). The distribution of the data into bins is informed by the tradeoff between minimizing the temperature spread in a given bin and including enough points to ensure convergence of the fit routines, which deployed both non-linear least squares and orthogonal distance regression (e.g., Boggs et al., 1992; Figures S1-S3). Because of their different temperature ranges, bins (a-c) contain experimental data and bins (d-h) contain FPMD data. Bins (e-h), which are entirely derived from FPMD simulations, are isothermal while bins (b-d) have standard deviations in temperature of ~130 K, 230 K, and 210 K, respectively. While the deviations from the mean bin temperature are clearly not

negligible, the combination of limited data, the likely rapid decrease of thermal expansion with pressure, and the large uncertainties in some volume measurements motivated us to bin these data together, while recognizing that there is a variability/error associated with deviations from the mean temperature of the bin. The experimental data, and especially the x-ray absorption and sink/float measurements, display considerable scatter that appears unrelated to any simple compositional variation. While the large uncertainties and scatter associated with the experimental measurements could possibly mask subtle unresolved compositional dependences of $\bar{v}_{H_2O}$, the high-pressure FPMD data show no discernible compositional dependences. For comparison, a compositional dependence of the low-pressure thermal expansion of the water component has been proposed to exist based on FPMD simulations (Dufils et al., 2020). As we discuss below, our equation of state inversions indicate that any compositional dependence of thermal expansion is expected to be markedly reduced by even shallow upper mantle pressures.

The optimized fit parameters for the EOS curves in Figure 2.2 are summarized in Table 2.2. The parameters reported for bin 1 (Figure 2.2a) describe the 457 K isotherm from the Brillouin spectroscopy study of Tkachev et al. (2005). Using their reported value of $(dV/dP) =$ -3.16 cm^3 mol^{-1} GPa^{-1} and estimating $\bar{v}_{0,457\,K} = 13.60$ cm^3/mol from their Figure 15 results in an approximate value of $K_{0,T} = 4.30$ GPa at this relatively low temperature. This is substantially smaller than the estimated volume of fluid water at the same temperature and 12 bar: $\bar{V}_{H_2O}$ = 20.44 cm^3/mol (Haar et al., 1984). In the 1440 K bin (Figure 2.2b), we used the volume maxima of the ambient

pressure and x-ray absorption measurements at relevant temperatures to bracket $\bar{v}_{0,H_2O}$ between 20 and 25 cm^3/mol. The change in $\bar{v}_{0,H_2O}$ from 20 to 25 cm^3/mol is associated with a ~50% decrease in $K_{0,T}$ and ~60% decrease in $K'_{0,T}$, illustrating the extreme dependence of inferred elastic properties on the initial volume of the water component. Our calculated value of $\bar{v}_{0,H_2O} = 25.10$ cm^3/mol is an order of magnitude lower than the calculated supercritical fluid volume of pure water, $\bar{V}_{H_2O}$ = 532.82 cm^3/mol at 230 bar and 1473 K (Haar et al., 1984). This pressure is just above the critical point of water, and is in a regime of both large volume and large compressibility of fluid water. At 1440 K, the Vinet and Birch-Murnaghan equations fit the data equivalently well up to about 4 GPa, where the Vinet equation trends towards a "denser" dissolved H_2O component than the Birch-Murnaghan EOS. Bin 3 (Figure 2.2c, 1873 K) contains all of the sink/float measurements, a large portion of the high-pressure x-ray absorption measurements, and a single ambient pressure measurement. A third order Birch-Murnaghan fit performs poorly on this subset of the data: best fit values of $K_{0,T}$ = 1.0 GPa and $K'_{0,T}$ = 3.5 yield a physically implausible compression curve that reverses on itself at higher pressures (i.e., reductions in volume are associated with reductions in pressure), so we use a fourth order Birch Murnaghan EOS to fit the data in bin 3. The reason for the unphysical behavior of the third order Birch-Murnaghan EOS is due to the small value of $K_{0,T}$ resulting in a large negative default value of $K''_{0,T}$ in the third order equation, which produces a reversal in sign of $K'_{0,T}$ under modest compression. For the 1873 K data, the fourth order Birch compression curve is initially stiffer than the Vinet curve until they intersect at 1 GPa (~22 cm^3/mol). The Vinet compression

curve remains above the Birch curve until they intersect again at about 15 GPa (~7.5 cm^3/mol). The Birch curve continues to decrease gently, reaching a value of $\bar{v}_{H_2O} = 5.17$ cm^3/mol at 136 GPa while the Vinet curve decreases more rapidly, reaching a value of $\bar{v}_{H_2O} = 1.85$ cm^3/mol at the same pressure (high pressure extensions of these curves can be seen in Figure 2.3).

The results of the FPMD simulations show strong internal consistency, which is anticipated based on their deployment of similar potentials (and, indeed, the usage of the standardized VASP calculational code across most of the FPMD studies). As Figure 2.1 shows, they are also in general agreement with the experimental measurements. Except for bins 3 and 4 (1873 and 2150 K), the bulk moduli returned by the Vinet and Birch fits are generally small and comparable, and show a trend of decreasing moduli with increasing temperature. The fit $K'_{0,T}$ values do not follow a simple monotonic trend for either equation, but the $K'_{0,T}$ values from the Birch fits in each case are systematically less than those from the Vinet fits at the same temperature (see Supplement 2). One aspect is, however, robust between all of the equation of state inversions: values of $K_{0,T}$ are extremely small at high temperatures, indicating that the compression curves are virtually entirely modulated by the first and second derivatives (whether the default $K''_{0,T}$ values of the EOS, or fit by a 4th order EOS) of the bulk modulus. Such values are not unprecedented for end-member phases: H_2 at ambient temperatures has similarly low bulk moduli derived from Vinet and B-M fits (e.g., Cohen et al., 2000). Within the Vinet EOS, the values of $K'_{0,T}$ markedly increase from the lower temperature (2150 K and below) to the higher temperature bins; this pattern

is not replicated in the B-M EOS results. The precise origin of this difference is unclear, but it is very likely associated with the differing default $K'_{0,T}$ values embedded within the 3rd order formulations of each equation of state.

The density of a geological melt that undergoes no change in composition (from crystallization, assimilation, or degassing, for example) along an adiabat reflects a tradeoff between the volumetric effects of thermal expansion and adiabatic compression. Thermal expansion decreases rapidly with increasing pressure, but at low pressures can serve as an effective control on the density (and hence, buoyancy) of melts, and is therefore a critically important parameter for predicting the movement of melts through the Earth. Hence, we model the thermal expansion of the dissolved water component as a function of volume. The Anderson-Grüneisen parameter,

$$\delta_T = -\left(\frac{1}{\alpha K_{0,T}}\right)\left(\frac{\partial K_{0,T}}{\partial T}\right)_P = \left(\frac{\partial ln\alpha}{\partial lnV}\right)_T \tag{2.6}$$

describes the normalized temperature dependence of the bulk modulus along an isobar (the first equality), or alternatively (and equivalently), the percent change in the coefficient of thermal expansion with the percent change in volume along an isotherm (the second equality). Anderson (1967) showed that if δ_T is independent of pressure and temperature, the coefficient of thermal expansion $\alpha = (1/V)(dV/dT)$ can be expressed as a function of volume:

$$\alpha = \alpha_0 (V/V_{0,T})^{\delta_T} \quad (2.7)$$

where $\alpha_0 = (1/V_{0,T})(dV_{0,T}/dT)$. Anderson and Isaak (1993) showed that for the quasiharmonic approximation at high temperature, δ_T can be written in terms of the pressure derivative of the isothermal bulk modulus $K'_{0,T}$:

$$\delta_T = K'_{0,T} + q - 1 \quad (2.8)$$

where $q = (\partial ln\gamma/\partial lnV)_T$. Combining Equations 7 and 8 yields an expression for α which is expressed entirely in terms α_0, which has been determined in low pressure experiments, and EOS parameters:

$$\alpha = \alpha_0 (V/V_{0,T})^{(K'_{0,T}+q-1)} \quad (2.9)$$

We determine the temperature derivative of $\bar{v}_{H_2O}$ at ambient pressure from the data in Figure 2.3a by fitting the volume-temperature measurements of O&L97,99 and Bouhifd et al. (2015); previously determined values of $(dV_{0,T}/dT)$ are summarized in Table 2.3 as well. We find $\left(\frac{dV_{0,T}}{dT}\right) = 11.4\ (\pm 0.4) \times 10^{-3}$ cm^3/K, and our preferred value of α_0 is given in Table 2.2. As with Agee (2008b), we use a pressure-dependent thermal expansion term due to both the extended pressure range of the data and simulations that we incorporate in our inversions, coupled with the empirical observation that thermal expansion decreases under compression (e.g., Figure 2.1). For comparison, Malfait et al. (2014a,b) and Seifert et al. (2013) assume $V_0(T) = V_0 exp(\alpha \Delta T)$. Key assumptions embedded in our usage of Equations 7-9 for the behavior of water in silicate liquids include: (1) that liquids behave quasiharmonically; and (2) that properties of melt components, and specifically dissolved water, adhere to

thermodynamic relations that are derived for bulk systems. The latter is a statement that ideal mixing occurs even with respect to thermodynamic derivative properties: that is, no anomalous coupling occurs between water and other components in the liquid. This assumption is consistent with both the lack of resolution of a significant compositional dependence in the elastic properties of water (Figure 2.1), and the lack of observation of any obvious anomalous behavior of the equation of state of the water component. The former assumption neglects the possible effects of major configurational changes. Nevertheless, when properties are assessed over a limited pressure/temperature range (such as near ambient pressure), an expectation is that dramatic structural changes may be limited.

The definition of q in terms of γ and V dictates that $q > 0$ if γ decreases during isothermal compression. A common assumption for the high pressure compression of solids is $q \approx 1$, where $q = 0.5 \pm 0.5$ captures a reasonable degree of variation for mantle minerals (Duffy and Ahrens, 1993). In contrast, high pressure studies on fluid water and silicate melt (from both laboratory experiments and FPMD simulations), have shown that γ can variably increase or decrease during compression, depending largely on changes in the first nearest neighbor configuration of the liquid (Stixrude and Karki, 2005; Mosenfelder et al., 2007). An increase in γ with compression implies that $q < 0$. For the water component, increases in hydrogen-bonding under compression are expected to increase the anharmonicity of the hydrogen bonding environment (e.g., Larsen and Williams, 1998): hence, pressure-induced increases in γ, and negative values of q, for the H_2O component are plausible and perhaps even

expected. In Figure 2.3d, we plot α as a function of pressure for $q = -0.5$. We used both Vinet and Birch equations to parameterize Equation 9 with respect to pressure and provide values of $K'_{0,T}$ (Bin 2 /1440 K and Bin 3/1873 K parameters from Table 2.2). When Equation 9 is calibrated with the 1440 K bin 2 data, $\left(\bar{\alpha}_{H_2O}\right)_{Birch}$ decreases more rapidly than $\left(\bar{\alpha}_{H_2O}\right)_{Vinet}$ (Figure 2.3d, blue curves). At 14 GPa, $\left(\bar{\alpha}_{H_2O}\right)_{Birch}^{1440\,K} = 2.88 \times 10^{-5} K^{-1}$ and $\left(\bar{\alpha}_{H_2O}\right)_{Vinet}^{1440\,K} = 5.18 \times 10^{-5} K^{-1}$ and the thermal expansion is treated as depending linearly on pressure: $\left(\frac{\partial \bar{\alpha}_{H_2O}}{\partial P}\right)_{Birch}^{1440\,K} = -1.81 \times 10^{-6}$ GPa^{-1}K^{-1} and $\left(\frac{\partial \bar{\alpha}_{H_2O}}{\partial P}\right)_{Vinet}^{1440\,K} = -3.38 \times 10^{-6}$ GPa^{-1}K^{-1}. When Equation 9 is calibrated with the 1873 K bin 3 data, in contrast with the 1440 K data, $\left(\bar{\alpha}_{H_2O}\right)_{Vinet}$ decreases much more rapidly than $\left(\bar{\alpha}_{H_2O}\right)_{Birch}$ (Figure 2.3d, red curves). At 14 GPa $\left(\bar{\alpha}_{H_2O}\right)_{Birch}^{1873\,K} = 1.65 \times 10^{-4}$ K^{-1} and $\left(\bar{\alpha}_{H_2O}\right)_{Vinet}^{1873\,K} = 4.78 \times 10^{-5}$ K^{-1}. Again, the pressure derivatives here are linear with $\left(\frac{\partial \bar{\alpha}_{H_2O}}{\partial P}\right)_{Birch}^{1873\,K} = -1.29 \times 10^{-6}$ GPa^{-1}K^{-1} and $\left(\frac{\partial \bar{\alpha}_{H_2O}}{\partial P}\right)_{Vinet}^{1873\,K} = -2.65 \times 10^{-6}$ GPa^{-1}K^{-1}. The substantially enhanced thermal expansion at high pressure associated with the Birch-Murnaghan equation calibrated to the 1873 K data appears to be a direct consequence of the more severe curvature enabled by the 4th order Birch-Murnaghan EOS as compared to the Vinet and 3rd order Birch-Murnaghan equations (e.g., Figure 2.2b-c). Figure 2.3d also shows the effect of pressure on the

coefficient of thermal expansion of fluid H_2O and the empirical formula of Agee (2008b), each of which lie between the 1440 K and 1873 K $\left(\bar{\alpha}_{H_2O}\right)_{Birch}$ curves.

Given the lack of a resolvable compositional dependence of the volume of water in silicate melts, a single function that relates pressure, volume, and temperature of H_2O in silicate melt based on the currently available experimental dataset can be generated. This function is designed to be straightforward to deploy, and to be able to be refined as more experimental and theoretical constraints are generated. Our means of producing such a uniform equation for both the Vinet and Birch equations is by introducing a thermal correction term $(\frac{\partial P}{\partial T})_V \Delta T = \alpha K_T \Delta T$, where both α (Equation 9) and K_T are expressed as functions of volume. The functional form of K_T depends on the equation of state. For the Vinet EOS we use the form provided by Vinet et al. (1987):

$$K_T(X) = \left(K_{0,T}/X^2\right)[2 + (\eta - 1)X - \eta X^2]exp[\eta(1 - X)] \tag{2.10}$$

And for the Birch equation we use a truncated version of the form presented by Birch (1978):

$$K_T(X) = K_{0,T}X^{-5}\left[1 + \frac{1}{2}(X^{-2} - 1)\left(7 - 3\left\{4 - K'_{0,T}\right\}\right)\right] \tag{2.11}$$

The general form of our temperature dependent finite strain equations is thus

$$P(X,T) = p(X) + \alpha(X)K_T(X)\Delta T \tag{2.12}$$

where $p(X)$ is the Vinet or fourth order Birch-Murnaghan EOS. The temperature dependent Vinet EOS is

$$P(X,T) = 3K_{0,T}\frac{(1-X)}{X^2}exp[\eta(1-x)] + (T - T_{ref})\{(K_{0,T}/X^2)[2+(\eta-1)X-\eta X^2]exp[\eta(1-X)]\}\alpha_0 X^{3(K'_{0,T}+q-1)} \quad (2.13)$$

The temperature dependent fourth order Birch-Murnaghan EOS is

$$P(X,T) = \frac{3K_{0,T}}{2}(X^{-7}-X^{-5})[1+\frac{3}{4}(K'_{0,T}-4)(X^{-2}-1) + \frac{1}{24}(9K'^2_{0,T}-63K'_{0,T}+9K_{0,T}K''_{0,T}+143)(X^{-2}-1)^2] + (T-T_{ref})K_{0,T}X^{-5}\left[1 + \frac{1}{2}(X^{-2}-1)(7-3\{4-K'_{0,T}\})\right]\alpha_0 X^{3(K'_{0,T}+q-1)} \quad (2.14)$$

We plot a series of isotherms using Equations 13 and 14 calibrated with the 1440 K and 1873 K data in Figure 2.3b and c,e and f. In Figure 2.3b and c, we use the 1440 K data to generate isotherms at 1273 K, 1473 K, and 1673 K. At ambient pressure, our isotherms are in good agreement with the experimentally determined values of $\bar{v}_{H_2O}$ at 1273 K and 1673 K from Bouhifd et al. (2015) and O&L97,99 (shows as stars in Figure 2.3b-c). The Vinet and Birch-Murnaghan isotherms fit the X-ray absorption data comparably between 0.5-3 GPa, with the Birch-Murnaghan equation suggesting a slightly weaker temperature dependence of $\bar{v}_{H_2O}$ and hence a more compressible dissolved H_2O component. In Figure 2.3e and f we use the 1873 K data to generate a

series of isotherms at 1873 K, 2073 K, and 2273 K. While there are not available ambient pressure measurements of $\bar{v}_{H_2O}$ at these temperatures, the isotherms are in good agreement with values generated by our 1 bar fit in Figure 2.3a. In accord with Figure 2.3d, the Vinet isotherms show a much weaker temperature dependence than the Birch isotherms. Our temperature dependent fourth order Birch-Murnaghan EOS is in generally good agreement with the high pressure FPMD data and our shock isochor: at 1000 K and 114 GPa there is a difference in volume of 6% and at 6000 K and 142 GPa there is a difference in volume of <1% (Figure 2.3f inset). Of the two temperature dependent finite strain equations calibrated to the experimental data from the 1873 K bin, we find that Equation 14 (Birch) is in better agreement with our shock isochor and the high pressure FPMD data. We note, however, that this is the bin for which the two equations yield the most disparate results, and is the only bin of the data for which a fourth order Birch-Murnaghan fit was required. Based on the good agreement between the Birch and Vinet equations in the other bins, we do not preclude the possibility that the equations will converge should less scattered data become available. Importantly, the net improved fit here associated with the Birch-Murnaghan equation of state does not, we believe, provide a statement on the general utility or applicability of either equation of state, but likely primarily reflects that the $K''_{0,T}$ inverted for in the 4th order Birch-Murnaghan equation generates a better fit to the present data set on the pressure-

dependence of the partial molar volume of water than the default $K''_{0,T}$ dependence on $K_{0,T}$ and $K'_{0,T}$ embedded within the 3rd order Vinet formalism.

Both calculational and experimental studies have suggested a convergence or near-convergence of the compression curves of the dissolved water component in silicate melt and fluid water at high pressures (Bajgain et al., 2015; Mookherjee et al., 2008; Du et al., 2019; Sakamaki et al., 2006, 2009; Malfait et al., 2014a). Accordingly, in Figure 2.3c we plot an 1873 K isotherm of fluid H_2O. The compression curves shown in Figure 2.3c indicate that the dissolved H_2O component is "denser" than fluid H_2O at pressures relevant to a large portion of the Earth's mantle; a possible cross-over is possible in the 90 GPa range, but this is not well-resolved by the data itself. Such a density cross-over, with its commensurate consequences for the $P\Delta V$ term associated with water dissolution in melts, would potentially have major implications for both the solubility of water within silicate melts and the possible presence of free fluid phases in the deepest mantle.

2.5 Hydrous silicate melt densities and their implications for melt atop the 410-km discontinuity and within ULVZs

The inferred density of a hydrous melt in the Earth's mantle depends not only on the composition of the melt, but on both the manner in which the thermodynamic variables of the two component melt-water system are assumed to mix, and on the endmember properties of the silicate melt and water components. The coordination number of iron in silicate melts has been shown to be compositionally dependent (Guo et al., 2013), but we assume a constant zero-pressure partial molar volume for each

oxide (Lange and Carmichael, 1987) in each melt composition. Here, we assess two mixing models (Figure 2.4a-d), which bear a resemblance to Voigt and Reuss averaging of the elastic properties of aggregates (e.g., Watt et al., 1976), with the notable difference being in the weighting of the components by mole fraction rather than volume. The advantage of such molar weighting is that, if zero pressure volumes and elastic properties of the component oxides are known, in principle, the volume of the melt at both ambient and high pressures can be determined from the melt composition. Moreover, utilizing mole fractions has a long tradition within silicate melt studies for modeling the compositional dependence of thermodynamic parameters (e.g.,

Carmichael et al., 1977; Bottinga et al., 1982). In the first model (Figure 2.4b,d), volume is assumed to mix linearly so that

$$\bar{V}_{Hydrous\ melt} = X_{H_2O}\bar{v}_{H_2O} + \left(1 - X_{H_2O}\right)\bar{V}_{Dry\ melt} \tag{2.15}$$

differentiating once with respect to pressure, the pressure dependence of the volume, dV/dP, emerges as an additive quantity; that is,

$$\left(\frac{d\bar{V}}{dP}\right)_{Hydrous\ melt} = X_{H_2O}\left(\frac{d\bar{v}_{H_2O}}{dP}\right) + \left(1 - X_{H_2O}\right)\left(\frac{d\bar{V}}{dP}\right)_{Dry\ melt} \tag{2.16}$$

The bulk modulus is $K_T = -V(\partial P/\partial V)_T$, thus

$$-\left(\frac{\bar{V}}{K}\right)_{Hydrous\ melt} = X_{H_2O}\left(\frac{d\bar{v}_{H_2O}}{dP}\right) + \left(1 - X_{H_2O}\right)\left(\frac{d\bar{V}}{dP}\right)_{Dry\ melt} \tag{2.17}$$

Or

$$-\frac{1}{K_{Hydrous\ melt}} = \frac{X_{H_2O}}{\bar{V}_{Hydrous\ melt}}\left(\frac{d\bar{v}_{H_2O}}{dP}\right) + \frac{1 - X_{H_2O}}{\bar{V}_{Hydrous\ melt}}\left(\frac{d\bar{V}}{dP}\right)_{Dry\ melt} \tag{2.18}$$

Since this approach casts the volume of a hydrous melt along a compression curve as a weighted average of the compression curves of dry melt and dissolved H_2O component, there is no requirement that the EOS of the dry melt and H_2O be of the same type or order. Once the compression curve of the hydrous melt is calculated, numerical differentiation or curve fitting techniques can be employed to determine EOS parameters. Such linear compositional mixing of volumes and compressibilities has been commonly invoked for silicate melts (e.g., Rivers and Carmichael, 1987; Jing and Karato, 2008; Sakamaki, 2017). As such, this formalism has been widely deployed to model the compression of silicate melts of variable compositions, including those incorporating water. Indeed, the difference in volume between dry and hydrous melts

has been the canonical method used to generate $\bar{v}_{H_2O}$ under compression (e.g., Bajgain et al. 2015, 2019; Du et al., 2019; Solomatova and Caracas, 2021; Agee 2008a,b; Sakamaki et al., 2006, 2009; Malfait et al., 2014a,b). For example, Sakamaki (2017) used this approach to show that the compression curve of the IT8720 composition, an extensive partial melt of peridotite generated at high pressure, may intersect the PREM density profile at the top of the MTZ with a quite hydrous 8 wt% (20 mol%) H_2O composition. However, the equation of state used by Sakamaki et al. (2006, 2009) and Sakamaki (2017) to describe the compression curve of the dissolved H_2O component in silicate melt does not appear to match the "Universal" EOS based on the Rydberg potential proposed by Vinet et al. (1986, 1987; Equation 5 above). For example, in Equation 1 of Sakamaki (2017), the pre-exponential factor $(\bar{v}_{H_2O}/\bar{v}_{H_2O,0})^{2/3}$ should, we believe, be in the denominator of the right-hand side of the equation: we are only able to reproduce the curvature of his equation of state of water in silicate melts with this factor in the numerator (as in Sakamaki, 2017). Using the volume-based mixing model and the anhydrous IT8720 peridotite partial melt composition, we find that a melt with a maximum value of 5.6 wt% H_2O will intersect the PREM density profile at the top of the MTZ. Importantly, higher water contents will generate buoyant melts,

and hence dictating that silicate melts lying above the 410 km seismic discontinuity be gravitationally stable at this depth likely limits them to moderate degrees of hydration.

An alternative approach to modeling hydrous melt density is to assume that the elastic moduli of the hydrous melt follow linear mixing so that

$$K^*_{Hydrous\ melt} = X_{H_2O} K^*_{H_2O-component} + \left(1 - X_{H_2O}\right) K^*_{Dry\ melt} \quad (2.19)$$

where K^* represents the bulk modulus and its pressure derivatives (Figure 2.4a,c), as assessed at high pressures. This can be viewed as an approximate extension of Vegard's Law to elastic properties, or equivalently an expression of linear compositional dependence of moduli: such assumptions have been deployed on a range of mixtures/alloys (e.g., Chizmeshya et al., 2004; Hallstedt et al., 2007). In this approach, K^* is determined algebraically, so the order of the hydrous melt EOS is dictated by the component with the lowest order EOS, since K^* must be consistently defined in order to conduct the mixing calculation. This approach thus has a significant limitation for hydrous silicate liquids, since the EOS's of the anhydrous melts we consider here have only been determined to second and third order, while a fourth order equation may be necessary to capture the large compressions of the dissolved H_2O component at the conditions of the transition zone and lower mantle. Furthermore, if different types of EOS are used to represent the melt and water components issues of compatibility arise since, for example, the canonical default value of $K'_{0,T} = 4$ has different implications for the Birch and Vinet third order EOS's, and particularly for the default fourth order term. In this approach, the addition of water to melt has the same effect on ρ_0 as in the previous approach, but the reductions in the elastic moduli of melts due to added water

are less pronounced. Hence, the density reduction associated with the water component at low pressures is less offset by decreased bulk moduli of the mixture, and the effect of water on the density of melts under pressure is larger than in the volumetric approach. This approach is predicated on linear mixing of elastic constants and their derivatives, and the validity of such linear mixing of higher order elastic properties has not been validated for molten silicate-water systems. Nevertheless, with this EOS approach, we find that the IT8720 melt composition can only intersect the PREM density profile at the top of the MTZ (producing a stably stratified melt) if $H_2O <$ 1.75 wt% (5 mol%), providing an even more stringent possible constraint on the hydration of melts at this depth. Using this mixing model, silicate melts with larger amounts of water are buoyant just above the 410 km discontinuity, and would not be expected to become stably stratified at this depth. Thus, the amount of water that can be present within neutrally or negatively buoyant melts above 410 km is, depending on the averaging method, *upper* bounded at between 1.75 wt% and 5.6 wt% (5 and 15 mol%): values that are each substantially less than prior estimates (e.g., Sakamaki, 2017), but the volumetric method with its inferred less than 5.6 wt% water content for neutral or negative buoyancy of the IT8720 composition is presently preferred. Our approach here differs conceptually from that of Freitas et al. (2017): we examine the effects of water on the density of known partial melts of peridotite (basaltic and the IT8720 compositions) that are generated within the upper mantle, whereas they probed partial melting undergone by upwelling hydrated transition zone material. Yet, the degree to which the transition zone is hydrated is controversial (e.g., Houser, 2016),

and estimates of melt layer thicknesses that can be generated by such upwellings are substantially thinner than many seismic observations: near 7 km (Hirschmann et al., 2007). And, a substantial number of seismic studies have emphasized the strong spatial correlation between the LVL on top of the 410 km discontinuity and nearby subduction zones (Revenaugh and Sipkin, 1994; Nolet and Zielhuis, 1994; Song et al., 2004; Courtier and Revenaugh, 2007; Gao et al., 2007; Hier-Majumder et al., 2014). Hence, a potential genetic connection of this layer with upper mantle subduction and descent of moderately hydrated melts appears to provide a viable means of producing this layer in near-subduction environments (and, lateral transport could advect subduction-generated hydrated melt into more distant, not-obviously-subduction-associated locales: e.g., Leahy and Bercovici, 2007).

The main panel of Figure 2.4f illustrates the long-standing recognition that estimates of the present-day adiabatic mantle geotherm lie far below the experimentally determined solidi of typical dry mantle rocks within most of the upper mantle and transition zone. While localized high temperature geothermal anomalies like mantle plumes could plausibly initiate melting near the MTZ, the apparent lack of global extent and seemingly limited lateral connectivity of the LVL on top of the 410 km discontinuity indicate that mineralogical/compositional heterogeneities almost certainly play a key role in initiating any melting at these depths at temperatures near the average mantle geotherm. Previous studies have shown that both H_2O and CO_2, introduced into the mantle at subduction zones via sialic and pelagic sediments or serpentinization of oceanic crust, can remain stable in solid phases to varying depths to

temperatures that approach the upper mantle geotherm within subduction zones. For example, Kawamoto and Holloway (1997) determined the solidus of water-saturated KLB-1 peridotite (reproduced in Figure 2.4f), and found that between 5-11 GPa the onset of melting remains constant at ~1273 K. The chemistries of melts generated along the solidus of water-saturated peridotite vary strongly with pressure, with melts becoming increasingly mafic at higher pressures. Melts generated at 1 GPa have an andesitic composition, and by 10 GPa the melts are more mafic than the starting material, with an approximately kimberlitic composition. This compositional crossover could play an important role in constraining the depths at which dense hydrous melts are produced, as the oxides that can most effectively depress the peridotite solidus (e.g., H_2O, CO_2, K_2O, Na_2O) have large low-pressure partial molar volumes in the liquid phase, are highly compressible, and are generally incompatible in the major mantle solid phases. For comparison, Ghosh et al. (2014) determined the solidus of carbonated peridotite between 10-20 GPa (reproduced in Figure 2.4f) and found that silicate melt first appears at 440-470 K lower than within volatile-free peridotite. Between 10-20 GPa, near-solidus melts in these carbonated systems generated between 1670-1940 K gradually change from carbonatitic to CO_2-rich silicate compositions with increasing temperature. The water storage capacity of eclogite at pressures and temperatures near the geotherm in the MTZ is less than that of peridotite (Litasov and Ohtani, 2010), and de facto H_2O concentrations in eclogite are sensitive to the degrees of water circulation to which they have been exposed in different tectonic environments. The destabilization of lawsonite (11.47 wt% H_2O), for example, can begin at ~6 GPa, but

along a cold mantle geotherm lawsonite may persist to depths of ~300 km (Ono, 1998). But, even in the absence of hydrous minerals, eclogites may still be able to transport significant amounts of water to the deep upper mantle along colder paths: H_2O enrichment in the nominally anhydrous minerals omphacite and pyrope, and isolated inclusions of immobile hydrous liquid, have each been suggested as effective transport methods (Mibe et al., 2003; Katayama et al., 2006; Matsukage et al., 2017).

Although the petrology of melts that could generate the LVL above 410 km depth is ill-constrained, our results do highlight a key, unresolved ambiguity. If simple linear mixing of volumes is appropriate for the water component, then the density of hydrous melts at the 410 km LVL is such that somewhat wet melts could be negatively buoyant at this depth (those containing up to 1.5 wt% water for a basaltic melt, as opposed to 5.6 wt% for the IT8720 composition); if a molar weighting of elastic properties instead obtains, then the limitation is near 0.5 wt% for basalt (and 1.75 wt% for IT8720). The seminal observation here is that the window in which negatively buoyant hydrous melts can occur on top of 410 km is both narrow in pressure (confined to *at most* 3 GPa, or ~90 km above the 410 km discontinuity: Figure 2.4e), and narrow in compositional space (with at most a few percent water). Carbon may well play a role in these liquids; but, because of the low densities of compressed hydrous carbonatites (Ritter et al., 2020), the carbon content of liquids is also likely to be limited by the dynamic requirement of neutral or negative buoyancy. Hence, our net interpretation is that hydrous melts (within fairly strict limits) can stably exist above 410 km depth: but, should they partially crystallize, or be progressively enriched in water by ongoing

subduction, they will likely buoyantly escape. As such, this region should probably be viewed as a rather narrow density trap for mildly volatile-enriched liquids.

In order to determine how much melt (and hence water) might be sequestered at depth above 410 km, we examine the interplay between seismic velocity reductions and melt contents. Seismic wave velocity reductions associated with partially molten rocks are a function not only of the extent of melting, but of the geometry and distribution of melt in the solid rock matrix. At low degrees of melting, there are two endmember partial melt topologies to consider: isolated melt inclusions and connected melt films, with tubules representing an intermediate geometry. In Figure 2.5a,b we show estimated P- and S-wave velocity reductions associated with melt tubes, spheres, and interconnected films, as calculated from the formulae of Walsh (1969) and Watt et al. (1976). Our range of aspect ratios varies from 0.005 to 0.05; characteristic experimental aspect ratios for anhydrous melt in olivine-dominated assemblages is ca. 0.1 (e.g., Faul, 1997; Daines and Kohlstedt, 1997), and the effect of water (which also lowers the viscosity of melts) is anticipated to lower this value. S-wave velocities are much more sensitive to the presence of melt than P-waves, and for both P- and S-waves, films are most effective at reducing velocity. Indeed, 10% melting can result in velocity reductions of ~20% and 60% for P- and S-waves if the melt forms low-aspect ratio films along grain boundaries. Previous seismic studies have resolved velocity reductions above the MTZ of ~1-5% in P-waves (Dahm et al., 2017; Li et al., 2014, 2017, 2019) and ~4-10% in S-waves (Revenaugh and Sipkin, 1994; Song et al., 2004; Gao et al., 2006; Vinnik and Farra, 2007; Jasbinsek and Dueker, 2007; Jasbinsek et al.,

2010; Schaeffer and Bostock, 2010; Wei and Shearer, 2017). These velocity reductions correspond to a wide possible range of melting, hinging on the geometry of the melt at depth. However, based on the temperature estimates of the mantle above the MTZ, the apparent reductions in P- and S-wave velocities, and observed textures in deformed hydrous partial melts within mantle assemblages (e.g., Mei et al., 2002; Ohuchi et al., 2012), it is likely that low aspect ratio melt films play an important role in generating the LVL, suggesting that melt on top of the MTZ is, where it occurs, present at less than ~5% by volume. Accordingly, we reproduce the PREM and IASP91 reference models in Figure 2.5c,d along with velocity estimates of partially molten mantle rock with 2 vol% melt distributed in films of varying aspect ratios. While we do not preclude the existence of a possible "melt layer", we emphasize that the seismic LVL can plausibly be explained by a relatively small amount of melt distributed throughout a ~ 25-50 km layer of solid rock above the MTZ, and that this mode of melt distribution is compatible with the seismically observed apparently poor lateral connection of the layer (e.g., Bagley and Revenaugh, 2008; Tauzin et al., 2010; Schmandt et al., 2011), and its depth extent, which in some instances exceeds 25 km thick (Gao et al., 2006; Vinnik and Farra, 2007; Jasbinsek and Dueker, 2007; Wei and Shearer, 2017; Hier-Majumder and Tauzin, 2017). A layer with 2% melting, in which melt is distributed in films with a 0.05 aspect ratio, produces general agreement with the velocity decrements observed in previous seismic studies (Figure 2.5c). Beginning at a depth of ~390 km, these conditions result in an S-wave velocity profile that is colinear with the model of Jasbinsek & Dueker (2007) to a depth of ~405 km. The best fit profile of Wei and

Shearer (2017) shows a larger velocity reduction than that of Jasbinsek and Dueker (2007), suggesting that the layer in the regions that they probe may have slightly higher degrees of melting or lower aspect ratio films (0.01-0.05). Hier-Majumder and Courtier (2011) similarly modeled the shear impedance contrast at the top of the LVL beneath the South Pacific (~350 km depth). Their model indicates that a layer with 1% melting can reproduce the observed -2.7% shear impedance contrast. The extent of melting required to produce the impedance contrast in their model depends on the dihedral angle: an increase in dihedral angle from 25º to 30º corresponds to a 0.1% increase in melt content. Nevertheless, the effective aspect ratio of films (or range of dihedral angles in the polymineralic deep upper mantle) remains a principal uncertainty: for example, Yoshino et al. (2007) proposed that the dihedral angle in the forsterite-water system may approach zero at deep upper mantle conditions. However, such fully wetted behavior, if present, does not appear to extend to the volumetrically important garnet and clinopyroxene components of the deep upper mantle (e.g., Liu et al., 2018).

In terms of the Earth's water budget, it is notable how singularly small an amount of water is necessary to generate a layer of such low-degree partial melting with modest hydration perched on top of the 410 km discontinuity. If we presume that there is 2% melting of a 25 km thick LVL (extending from 385-410 km depth), and that the melt contains 3 wt% water, the net total amount of water sequestered in the layer would be of order 2.4×10^{19} kg, or 1-2% of the surficial ocean's mass of ~1.37 x 10^{21} kg. Indeed, although it has been proposed that the LVL above the MTZ might be global with strong lateral variations in thickness (Tauzin et al., 2010), Wei and

Shearer (2017) have estimated it as being present at the 33-50% level underneath the Pacific (the region in which they had the best data coverage). As such, it is likely that this estimate of the potential water retention of this layer may well be overestimated by a factor of 2-3. In this regard, a notable conclusion is that a relatively tiny fraction of the Earth's surface hydrosphere, if present at depth within the mantle, could generate a notable, broadly observed seismic anomaly. And, these small melt quantities render the long-term geologic history of this layer difficult to infer. The layer involves a sufficiently subtle compositional and density variation that melt at this depth is unlikely to have persisted through Earth history. Indeed, in a hotter mantle in the past, the window in which melt at this depth is dynamically stable is likely to have been smaller: this is simply because the thermal expansion of silicate liquids remains greater than those of solids at this depth. Yet, possibly higher mantle temperatures in the past may have enhanced the net abundance of melt in the more narrow depth range where it was both compositionally and dynamically stable. In fact, the evolution of partial melt within this region may be Darwinian in nature: melts generated at this depth with too high a water content will buoyantly ascend into the upper mantle, and this region will thus only trap rather modestly hydrated melts. And, if there is subduction-associated influx of further volatiles into the region, non-buoyant trapped magmas may become more water-enriched and escape.

If solid state transport of bound water (or, more speculatively, trapped hydrated melt) can occur to mid-lower mantle depths through subduction, then the genesis (or release) of hydrous melts within the mid-lower mantle is likely to generate melts that

descend. Indeed, we find that the addition of small amounts of water to natural melt compositions, perhaps with even less than 1 wt% H_2O, can generate melts that become negatively buoyant at pressures greater than 50-90 GPa (Figure 2.4e). Accordingly, depending on the efficiency with which hydrous materials are subducted to these depths, descending melts may either metasomatize deeper-seated mantle, or ultimately descend to the core-mantle boundary. The potential of such melts to migrate downward, and ultimately coexist with dense solids in the lowermost mantle produces an obvious possible outcome of melt presence at the base of the mantle: a result fully in accord with the likely presence of partial melting within ULVZ's at the base of the mantle (e.g., Williams and Garnero, 1996; Rost et al., 2005; Du et al., 2019). Here, the compositional constraints on hydrous melts are less apparent than those for the LVL on top of the MTZ. In particular, as Du et al. (2019) note, there are trade-offs between iron-content and the water content in terms of the bulk density of the region. Nevertheless, the densities of peridotite-derived partial melts with ~3 wt% H_2O are, because of the high compressibility of silicate liquids, ~4% greater than the PREM density distribution at the base of the mantle. For comparison, Rost et al. (2005; 2006) derive a density for particularly well-probed ULVZ locations of ~10% greater than that of the PREM mantle. As such, the amount of iron within this layer is clearly elevated; the absolute amount of (density-enhancing) iron can trade-off with the inferred amount of (density-depressing) water in the liquids. We estimate the density of variably FeO- and H_2O-enriched silicate melt at 136 GPa and 4000 K to determine the critical ratio of FeO to H_2O (wt%) for which neutral buoyancy will be maintained at the base of the

mantle. In order to isolate the volumetric contributions of FeO and H_2O, initial anhydrous melt compositions are considered in an idealized MgO-FeO-SiO_2 system, with compositions varying according to $X_{SiO_2} = 40\ mol\%$ and $X_{FeO} = 100 - X_{SiO_2} - X_{MgO}$. Ambient pressure densities and bulk moduli of the anhydrous melts are calculated with the models of Lange and Carmichael (1987) and Kress and Carmichael (1991), and a value of $K'_{0,T}$ = 5 is used for each composition (published values of $K'_{0,T}$ for peridotite melts range between 4-7.3; Sakamaki et al., 2010). Anhydrous melt with less than ~15 wt% FeO (~10 mol%) is buoyant with respect to the PREM density profile at the CMB, but linear mixing of an anhydrous melt with water with a partial molar volume of 5.42 cm^3/mol indicates that initially anhydrous melt with ~25 wt% FeO (~20 mol%) will maintain negative buoyancy upon addition of up to ~10 wt% H_2O. More precisely, we find that a tradeoff of 1.25 wt% FeO per 1 wt% H_2O constrains the composition of melt along the CMB density isopleth: this is in general accord with the results of a similar calculation by Du et al. (2019).

2.6 Conclusions

Both Birch and Vinet equations of state were fit to the available data on the volume of the H_2O component in silicate melts under pressure. Sink-float, X-ray absorption, low-pressure volumetric measurements, Brillouin spectroscopy data, first principles molecular dynamics, and a new isochor for the dissolved water component in silicate melt derived from previous shock experiments are included within the overarching analysis. A fourth order Birch-Murnaghan equation of state calibrated to the sink-float and X-ray absorption data was found to be in good agreement with the

shock isochor and first principles molecular dynamics data at high pressures; a general thermal expansion term is also derived. At this juncture, no clear dependence of $\bar{v}_{H_2O}$ on bulk melt composition is resolved. Additionally, the volume of dissolved water in silicate melts is consistently less than that of fluid water at the same temperature, although the two become difficult to distinguish from one another near ~90 GPa. The effects of different mixing models on hydrous melt densities were examined, and mafic to ultramafic melts containing an upper bound of between 1.75 and 5.6 wt% H_2O (with the higher value preferred) can become neutrally/negatively buoyant above the mantle transition zone. A seismic velocity model using these results, and taking into account the effects of melt texture and geometry on P- and S-wave velocity reductions, indicates that extents of melting as low as 2% can generate detectable seismic signals above the mantle transition zone. The low velocity layer on top of the 410 km discontinuity is hence interpreted as a density trap for moderately volatile-enriched silicate melts, with the trap being dictated by a narrow window of dynamic stability in both pressure and composition space for hydrous melts. In contrast, the inferred enrichment of iron in deep mantle ULVZ's suggests that substantially wetter melts could be neutrally buoyant at the core mantle boundary: at these depths, the criterion of neutral or negative density contrasts for stability of partial melts results in a direct tradeoff between iron content and water content. As such, absolute water amounts cannot be readily constrained based on density criteria alone.

Chapter 3: High pressure Raman spectroscopy and X-ray diffraction of $K_2Ca(CO_3)_2$ bütschliite: Multiple pressure-induced phase transitions in a double carbonate

3.1 Introduction

The rare carbonate mineral bütschliite (also spelled buetschliite), with chemical formula $K_2Ca(CO_3)_2$, has been observed to form in highly disparate geological environments. First discovered and named in 1947, the mineral was initially found in wood-ash stones from the western United States (Milton and Axelrod, 1947). More recently, bütschliite has been identified as an inclusion/daughter phase in mantle-derived olivine and diamond crystals (Abersteiner et al. 2022; Logvinova et al. 2019). Occurrences of bütschliite in granitic pegmatites have also been reported (Bermanec et al. 2011).

The identification of bütschliite inclusions not only in diamond, but in mantle-derived olivine as well, suggests that alkaline carbonate melts and solid mineral phases could play an important role in the petrogenesis of kimberlites and carbonatites. Indeed, Chayka et al. (2021) suggests that even alkaline-poor carbonatites may be derived from substantially alkaline-enriched parental magmas. Candidates for potassium-bearing mineral phases in the mantle are limited: the phyllosilicate mineral phlogopite and the amphibole richterite have been identified in a number of mantle-derived xenoliths and within the results of experiments on hydrated and carbonated peridotite (e.g., Harlow and Davies, 2004; Meltzer and Kessler, 2023), but in terms of potassic carbonate minerals, only bütschliite has been reported in mantle assemblages. Several studies have explored the stability of the related synthetic material $K_2Mg(CO_3)_2$ (Brey et al.

2011; Golubkova et al. 2015; Arefiev et al. 2018), but this compound has not been identified as a mineral phase in nature.

Investigations into the stability and structure of bütschliite at non-ambient conditions have been limited. McKie (1990) studied the system $K_2Ca(CO_3)_2$-$Na_2Mg(CO_3)_2$ and determined that fairchildite, the intrinsically-disordered high-temperature polymorph of bütschliite, and eitelite ($Na_2Mg(CO_3)_2$) can form an extensive solid solution, while bütchsliite and eitelite are almost completely immiscible (limited to < 2 mol% solid solution). Arefiev et al. (2019) and Shatskiy et al. (2015) studied the K_2CO_3-$CaCO_3$ system at high temperatures and 3 and 6 GPa, respectively, and observed the presence of bütschliite as a sub-solidus phase at each pressure. Hou et al. (2022) and Tian et al. (2023) employed first-principles simulations via the VASP calculational package (Kresse and Furthmüller, 1996) to examine the structure of bütschliite under isothermal compression to ~22 and ~26 GPa, respectively, and both studies calculated transitions to monoclinic and triclinic phases, albeit with different sequences and at different pressures. Zhuravlev (2022) deployed the CRYSTAL17 *ab initio* package to calculate the elastic constants of bütschliite under compression. He noted that the C_{44} shear elastic constant appeared to be soft, trending towards zero at 5.8 GPa, thus indicating that an unspecified phase transition is anticipated at this pressure. In this study, we present the results of the first in-situ high-pressure, ambient-temperature Raman spectroscopy and synchrotron x-ray diffraction experiments on bütschliite to 95 GPa. These delineate the transition pressures and properties of the high-pressure phases of this material. Our results shed light on the crystal structures

and bonding environments of low symmetry carbonate minerals at high pressures, as well as the role played by cations in the compressibilities of these minerals.

3.2 Methods and Sample Synthesis

Bütschliite crystals were synthesized following the method of Pabst (1974), in which millimeter-scale cleavage rhombs of optical-quality calcite are immersed in a saturated K_2CO_3 solution and heated to between 50 to 70°C for several days. Crystals grown in this manner are typically euhedral and free of inclusions, making them suitable for both optical and x-ray-based measurements. While bütschliite was the most abundant phase produced by this method, small amounts of other (possibly hydrated) potassium/calcium carbonate phases were sporadically detected in Raman spectroscopy measurements. Bütschliite is hygroscopic and deliquesces readily in air over the course of a few hours. Samples were stored in toluene after synthesis; crystals stored in this organic liquid remain stable indefinitely. As a mildly non-hydrostatic pressure medium, silicone oil was chosen for some experiments over a methanol/ethanol solution to minimize the risk of crystal degradation due to hydration; neon, which more closely approaches hydrostaticity at high pressures, was used as a pressure medium for a large number of the experiments. Notably, crystals stored in high purity methanol/ethanol solutions (< 0.01% water) at slightly elevated pressure did not show any signs of degradation over the course of a few weeks.

3.2.1 Raman Spectroscopy

Ambient and high-pressure Raman spectra were collected on a LabRAM HR Evolution spectrometer equipped with a 532 nm excitation laser nominally rated at 50

mW. A grating of 1200 lines/mm was employed and spectral resolution is ~1 cm^{-1}. Samples were loaded into symmetric-style diamond anvil cells equipped with 250 or 350 μm culet diamonds. Rhenium gaskets were used for all Raman experiments, and silicone oil or neon were used as pressure transmitting media in different runs. Ruby spheres or small amounts of ruby powder were loaded into the sample chamber and the calibration of Shen et al. (2020) was used for pressure determination. Ruby emission lines became unresolvable at pressures above ~85 GPa, and pressures were determined from the Raman shift of the diamond anvil measured at the center of the culet (Akahama and Kawamura, 2006). Peak fitting and deconvolution were carried out with the Horiba LabSpec 6 software.

3.2.2 Synchrotron Single Crystal X-ray Diffraction

The high-pressure single-crystal x-ray diffraction experiments were performed at ambient temperature using short symmetric, Merrill-Bassett, and BX-90 diamond anvil cells equipped with 300–400 μm culet Boehler-Almax diamond anvils and c-BN/WC seats providing a ~90° opening angle. Re and Inconel gaskets were indented to ~30–50 μm, and sample chambers were drilled with diameters of 150–180 μm with a laser-milling system. Single-crystal samples, measuring ~50×50×10 μm, were mounted directly onto the diamond culet with a small amount of vacuum grease to minimize movement of the crystal during loading of the pressure media. Neon or silicone oil were used as pressure transmitting media in different runs. Pressure media were loaded into the sample chambers immediately after sample loading to avoid the risk of sample degradation.

The high-pressure diffraction data were collected at end-station 2 of beamline 12.2.2 of the Advanced Light Source at Lawrence Berkeley National Laboratory using synchrotron x-rays monochromated by silicon (111) with an energy of 30 keV ($\lambda = 0.4132(1)$ Å), focused to a 10×10 μm spot. The diffraction spots were collected on a Pilatus3 S 1M fast detector. Exposure times ranged from 1 to 8 sec/º. Detector distance and wavelength calibration were performed using CeO_2 powder and a NIST single-crystal ruby sphere. The sample was aligned to the rotational center of the goniometer, and data were collected throughout the range of $\theta = -35°$ to $35°$ (in $0.50°$ and $1.00°$ increments) for a total coverage of ~$70°$ sample rotation. The diffraction data were corrected for the reduction of reflection intensities due to the DAC-gasket shadowing and indexed and reduced to *hkl* sorted structure factors by integration using the program SAINT v8.34A in APEX3 (Bruker, 2016). Before structure solution steps, a few individual reflections (with negative and almost zero intensities) were removed from the data set because their intensities were affected by simultaneous diffraction events in the diamond anvils. A total of ~150–250 unique reflections were available for subsequent structural analysis. The structure solutions were carried out with SHELXS (embedded in APEX) using direct methods and refined with SHELXT (Sheldrick, 2008) by full-matrix least-squares on F^2. For every structure, ~34 parameters including overall scale factor, isotropic atomic displacement factors, and fractional coordinates of the atoms were refined; for bütschliite-II, the greater number of distinguishable atoms within the unit cell increased the number of parameters solved. Ball and stick structural models were produced in *VESTA 3* (Momma and Izumi, 2011).

3.2.3 Synchrotron Powder X-ray Diffraction

High-pressure powder x-ray diffraction measurements were also collected at ALS beamline 12.2.2, using BX-90, symmetric, and Merrill-Bassett diamond anvil cells with diamond culet sizes ranging between 300–500 μm. Diamonds were mounted on c-BN or WC seats. Inconel and rhenium foils were used for gasket materials, and silicone oil or neon were employed as pressure media in different runs. An exposure time of 30 sec was used and x-ray beam energies of 25 and 30 keV were used in different runs. Powder patterns were indexed with the LeBail method in GSAS-II (Toby and Von Dreele, 2013). Peterson (2004) suggests that the LeBail method can be inappropriate for low symmetry phases; however, this method was preferable to the Rietveld method for these samples since the acquired powder patterns were highly textured due to apparent preferred orientation of grains of the first high pressure phase.

3.3 Results and Discussion

3.3.1 Single Crystal and Powder X-ray Diffraction of Bütschliite

X-ray diffraction measurements were previously made on bütschliite-I under ambient conditions. Mrose et al. (1966) erroneously reported, due to a misprint in the original publication, that bütschliite crystallizes in the $R\bar{3}$ space group. Pabst (1974) determined that bütschliite crystallizes in the $R\bar{3}m$ space group (reported as $R\bar{3}2/3$) with a = 5.38 Å, c = 18.12 Å, and Z = 3, and has a structure very similar to that of eitelite, despite the difference in space groups (eitelite belongs to the $R\bar{3}$ space group and lacks a mirror plane due to rotation of the carbonate anions). The ambient bütschliite structure is characterized by planar sheets of [CO_3] units separated by

alternating interstitial layers of Ca^{2+} and K^{+} cations (Figure 3.1a,b). Pabst (1974) reports a unit cell volume of 454.2 $Å^3$, which is in excellent agreement with our measured value of 453.9 $Å^3$. Compression of bütschliite is strongly anisotropic, with contraction of the *c*-axis accounting for most of the volume change (Figure 3.2a–c). The contraction of the unit cell along the *c*-axis follows a steeply linear trend up to the first phase transition, with $\Delta c/\Delta P$ = 0.23 Å/GPa. This style of anisotropy has also been observed in the isostructural synthetic compound $K_2Mg(CO_3)_2$, and is a result of the greater compressibility of the [KO_9] polyhedra compared to the alkaline earth cation polyhedra and trigonal planar [CO_3] units (Golubkova et al., 2015). Most of the reduction in the bütschliite unit cell volume occurs via reductions of the K-Ca and K-O distances. The C-O, O-O, and Ca-O distances remain largely unchanged during compression (Figure 3.1).

The combined single crystal and powder pressure-volume data were recast into Eulerian stress-strain coordinates and fit with a Birch-Murnaghan equation of state (Figure SI 1). The equation of state was fit to the stress-strain data using an orthogonal distance regression to account for uncertainties in both pressure and volume resulting in a bulk modulus of $K_0 = 46.9(17)$ GPa with an imposed value of $K_0' = 4$ (Figure 3.2f). The equation of state fit to the x-ray diffraction data indicates that the structure is more compressible than the results from the first principles calculations of Hou et al. (2022), but close to the results of Zhuravlev (2022). Our values of K_0 is 23% smaller than the value calculated by Hou et al. (2022). Notably, our measurements of the bütschliite low-pressure phase extend to higher pressures than the calculations of Hou

et al. (2022), as their calculations yield a $P\bar{1}$ phase intermediate between the $R\bar{3}m$ and *C*2/*m* phases at pressures between 3.3 and 10.3 GPa: this phase is not seen in the x-ray diffraction data in this pressure range. In terms of elasticity, the discrepancy between the theory and experiment appears to primarily involve the compressibility of the c-axis: the calculations of Hou et al. (2022) underpredict the experimentally observed compressibility of this axis.

3.3.2 Single Crystal and Powder X-ray Diffraction of Bütschliite-II

Bütschliite undergoes a phase transition between 5.5 and 6.0 GPa. Our lowest pressure refinement of the bütschliite-II phase from the single crystal data is at 6.3 GPa. The high-pressure phase crystallizes in the monoclinic system with *C*2/*m* symmetry (space group #12) and Z = 2, with cell parameters at this pressure of a = 9.182(7) Å, b = 5.299(6) Å, c = 6.354(11) Å, and $\beta = 120.06(3)°$. The volume change across the phase transition on a formula unit basis is small but discontinuous, indicating that the transition is first-order (Figure 3.2e). This is in accord with hysteresis observed in the transition using Raman spectroscopy, described below. Based on the single-crystal data, there is a 2% density increase associated with the transition from the hexagonal to monoclinic phase between 5.5 and 6.3 GPa. The small ΔV across the phase transition indicates that the Clapeyron slope between the two phases is likely to be relatively flat, which in turn suggests that the pressure of the phase transition is unlikely to have a robust temperature dependence. The transition from the hexagonal to monoclinic phase is reversible, with the high-pressure phase reverting to bütschliite on decompression below ~2 GPa. Following the method of Jeanloz (1981), an equation of state was fit to

the high-pressure bütschliite-II phase (Figure SI 2) with parameters $V_0 = 322.2$ Å^3, $K_0 = 24.8(44)$ GPa, and $K_0' = 4.0(11)$ (Figure 3.2f). Our fit bulk modulus is 50% smaller than the value calculated by Hou et al. (2022). And, the bulk modulus of bütschliite-II is substantially less than the bulk modulus of $K_2Mg(CO_3)_2$-II, $K_0 = 58.4$ GPa, reported by Golubkova et al. (2015). The bulk moduli of the bütschliite-I and -II phases are low relative to most other carbonates, but that of the low-pressure phase is comparable to the bulk moduli of $BaCO_3$-witherite and Ag_2CO_3 (Wang et al. 2015; Santamaria-Perez et al. 2023). Similarly, the lower bulk modulus of the high-pressure phase is unusual, but not unprecedented for carbonates: a high-pressure phase in layered Ag_2CO_3 has a bulk modulus of 26 GPa (Santamaria-Perez et al. 2023). A key aspect here is that the *C*2/*m* symmetry phase appears to be stabilized at high pressures by its high compressibility.

Notably, there is not particularly good agreement between the volumes and phase transition pressures of the theoretical calculations and experiments plotted in Figure 3.2. The first principles simulations of Hou et al. (2022) and Tian et al. (2023), carried out at 0 K, both predict phase transitions near 3.5 and 10.5 GPa, but the order of the transitions is different. Hou et al. (2022) reports a transition from the $R\bar{3}m$ phase to a triclinic $P\bar{1}$ structure at 3.3 GPa followed by a transition to the monoclinic *C*2/*m* structure at 10.3 GPa, while Tian et al. (2022) reports a transition to the monoclinic *C*2/*m* structure at 3.3–3.5 GPa and a transition to the triclinic $P\bar{1}$ structure at 10.3–10.5 GPa. The source of this disparity is unclear, as both simulations were conducted using the VASP software package, and the cut-off and convergence criteria of their

calculations seem to be essentially identical. That said, the reported differences in enthalpies between the three phases at 0 K are quite small: near 10 GPa, less than 0.08 eV/formula unit reported by Hou et al. (2022), and less than 0.07 eV/atom according to Tian et al. (2023). The difference between the *C*2/*m* and the $P\bar{1}$ structures is even smaller, being less than 0.01 eV/formula unit (Hou et al. 2022) or 0.01 eV/atom (Tian et al. 2023) up to 12 GPa. As such, calculations at 0 K without thermal corrections might not accurately predict phase stabilities for such energetically close phases even at ambient temperatures. For comparison, Zhuravlev (2022) (using a different *ab initio* software package) predicts a shear instability to an unspecified structure at 5.8 GPa. There is also likely an effect of kinetics on the experimentally observed bütschliite-I to -II phase transition at 300 K: the transition is observed on the up-stroke near 6 GPa, and the reversion is observed on the down-stroke near 2 GPa. Accordingly, the equilibrium transition may occur close to 4 GPa (from the mid-point between the up-stroke and down-stroke transition pressures) at 300 K. Consideration of kinetic effects thus might somewhat improve the agreement between theory and experiment with respect to the pressure of the first transition in this material.

In contrast to the low-pressure phase, where compression occurs predominantly along the *c*-axis of the hexagonal cell, rotation and interlayer shifting seem to be almost entirely responsible for the enhanced compressibility of the bütschliite-II phase. The trend of $3c\sin(\beta)$ in Figure 3.2c serves as an analogue for the interlayer spacing within the low-pressure phase, and shows that the interlayer compression is largely monotonic across the transition. The change in slope of the $3c\sin(\beta)$ trend is likely a result of

changing K-O bond lengths (discussed below). All axial parameters follow relatively flat linear trends on compression while the β-angles follow an increasing quadratic trend, with $\beta(P) = -0.033P^2 + 1.371P + 113.204$ (Figure 3.2d). This increase in β-angle directly reflects the pressure-induced lateral shifting between layers (e.g., Fig. 1d). It is this interlayer shifting that likely renders the high-pressure phase elastically softer than the low-pressure bütschliite phase: the complementary effects of carbonate group rotation and layer shifting provide additional means of compaction that are unavailable to the low-pressure phase. Beyond the rotation and layer shifting, the overarching structural similarities of the two phases produce pressure-induced trends of bond valence sums (Kunz and Brown 1995) that appear continuous between the two phases under compression: both cations and the oxygen ions have bond valence sums that increase over the pressure range of our single-crystal measurements (Figure SI 3).

The phase transition to bütschliite-II results in the bifurcation of several atomic distances and bond lengths (Figure 3.1f, g, j, k). The high-pressure phase gives rise to two unique C-O and Ca-O bond lengths. The evolution of the K-O bond lengths is more complex. Within both the bütschliite and *C*2/*m* phases, potassium has been generally viewed as being in nine-fold coordination: in the *C*2/*m* phase, the 9-coordinate geometry is that of a distorted tri-capped trigonal prism (e.g., Akella and Keszler 1995a,b). However, within the $K_2Ca(CO_3)_2$ *C*2/*m* phase, depending on the radius of the coordination sphere of potassium, the K^+ cations may be viewed as undergoing a coordination change, initially forming elongated [KO_{12}] cuboctahedra (perhaps more appropriately viewed as 9+3 coordination), with the longer K-O bond lengths being

coupled to the rotation of the [CO_3] anions (Figure 3.1h). Here, we view K-O distances of 3.3 Å and less as being clearly within the coordination sphere of the K ion, based on the maximum eight-fold K-O distances in a survey of K-bearing compounds being 3.17 Å (Wood and Palenik 1999), and the typical difference in bond distance between eight and twelve-fold coordination being 0.13 Å (Shannon 1976). Such distances are accessed by additional oxygens above ~8 GPa (Figure 3.1h); the general trajectory of the more distant K-O distances (Fig. 1h) indicates that this transition to higher coordination is progressive following the transition to the high pressure phase (with those distances closer than ~3.5-3.6 Å potentially being viewed as part of a secondary coordination distance, giving rise to 9+2 or 9+3 coordination).

With increasing compression, the [CO_3] units become more oblique with respect to the a-axis and, as shown in Figure 3.3, there is a direct line-of-sight interaction between the K^+ ion and the neighboring carbon ion that is coordinated to the three additional oxygens that approach the coordination sphere of the potassium. Repulsion between the C and K atoms likely contribute to the rotation of the [CO_3] units, as the C-K distance remains constant around 3.25 Å during compression: increasing pressure does, however, induce a rotation of the carbonate units. This shift in geometry rotates two oxygens closer to the potassium ion, and one further away: as such, at 9.5 GPa, the local coordination of potassium might be viewed as 11-fold, or 9+2 coordinated. Notably, if the C-K distance is indeed near some minimum critical value, then the rotation of [CO_3] units and change in β-angle can be interpreted as structural distortions which serve to maintain this value. We quantify the degree of

tilting of the [CO_3] units by measuring the angle θ, formed by the intersection of the (001) plane with a plane passing through the three oxygens atoms of the [CO_3] unit, as a function of pressure. This trend is well characterized by a quadratic polynomial in pressure, with $\theta(P) = -66.86 + 15.95P - 0.79P^2$ (Figure 3.4).

Our powder diffraction data on bütschliite access considerably higher pressure conditions, up to 67.5 GPa (Figure SI 4). These data show strong evidence for multiple higher pressure phase transitions, for which the pressures of occurrence are more accurately determined by Raman spectroscopy. Nevertheless, clear evidence is seen for three transitions between ~26 and 40 GPa, although indexing of these phases proved challenging due to poor crystallinity/weak diffraction patterns, as well as probable preferred grain orientation in the high-pressure phases. New diffraction peaks associated with these phases are shown by arrows in Figure SI 4b. A key aspect here is that there is continuity of several features in the diffraction patterns throughout the pressure range to 67.5 GPa (Figure SI 4). This observation provides a general indication that the overall layered topology of the structure persists, with moderate symmetry changes, to the highest pressures of these measurements at 300 K.

3.3.3 Raman Spectroscopy Overview

Our ambient spectrum of the synthesized bütschliite (Figure 3.5) is in good agreement with previous measurements (Arefiev et al., 2019) and calculations (Caracas and Bobocioiu, 2011). Representative spectra taken on compression up to 94 GPa, along with mode shifts, are plotted in Figure 3.6. Our Raman measurements access substantially higher pressures than the XRD measurements, and we documented

multiple phase transitions at elevated pressures in detail in the Raman spectral experiments which are discussed in the following sections.

3.3.4 Raman Spectra of Bütschliite-I

Factor group analysis of bütschliite-I yields

$$\Gamma_{optic} = 4\mathrm{A_{1g}} + \mathrm{A_{1u}} + \mathrm{A_{2g}} + 4\mathrm{A_{2u}} + 5\mathrm{E_u} + 5\mathrm{E_g}. \quad (3.1)$$

In this irreducible representation, the A_{1g} and E_g modes are Raman-active. We observe 10 peaks in the ambient bütschliite spectrum (Figure 3.5), with eight first order ($5E_g$, $3A_{1g}$) and two second order modes (assignments are derived from Caracas and Bobocioiu, 2011): six of these peaks are resolvable once the sample is loaded into the DAC with a pressure medium.

All observed modes exhibit positive linear frequency shifts with pressure up to the first phase transition to the *C*2/*m* structured phase (Figure 3.7 and Table 3.1). The symmetric (ν_1) and asymmetric (ν_3) stretches have similar pressure shift rates: 5.44 and 5.78 cm^{-1}/GPa, respectively. The in-plane bend shifts at a considerably slower rate, with a value of 2.48 cm^{-1}/GPa. The lattice modes exhibit larger variations in their pressure shifts and are, based on their mode-Grüneisen parameters, more anharmonic. The A_{1g} lattice mode with an initial frequency of 224 cm^{-1} shows the largest deviation from harmonicity among all observed modes: the large pressure-shift of this mode, which is associated predominantly with translations of the carbonate group along the c-axis of the structure (Caracas and Bobocioiu, 2011), likely directly reflects the large compressibility of the *c*-axis observed within the diffraction experiments. Although the lack of thermal expansion data on bütschliite precludes calculation of a bulk

thermodynamic Grüneisen parameter for this phase, it is clear from Table 3.1 that the largest contributors to this parameter are, as expected, among the lattice vibrations.

3.3.5 Raman Spectra of Bütschliite-II

The first signs of a phase transition observed in the Raman data occur at 6.5 GPa, and the spectrum at this pressure likely corresponds to a mixed-phase regime. At this pressure, the first hint of three new lattice modes appears between 110 to 150 cm^{-1}. The highest frequency lattice mode broadens asymmetrically prior to splitting into three peaks, and ν_4 and ν_3 broaden asymmetrically prior to splitting into two peaks each. By 7.2 GPa the sample appears to be fully converted to the bütschliite-II phase. While the ν_2 vibration is weakly present in the ambient bütschliite spectrum, it becomes, for the most part, unresolvable once the sample is loaded into the DAC with a pressure medium. The change in symmetry to *C*2/*m* in the high-pressure phase results in a substantial increase in the amplitude of the ν_2 peak during compression (Figure 3.8b).

Factor group analysis of the bütschliite-II structure yields

$$\Gamma_{optic} = 9\mathrm{A_g} + 6\mathrm{A_u} + 6\mathrm{B_g} + 9\mathrm{B_u}. \quad (3.2)$$

Here, the A_g and B_g modes are Raman active. Symmetry assignments and pressure shifts of the bütschliite-II carbonate modes are reported in Table 3.2 and Figure 3.9. The mode Grüneisen parameters are calculated at high pressure using a Taylor expansion of $K(P)$ with a truncating value of K_0'' (i.e., $K_0'' = \frac{1}{9K_0}[63K_0' - 9K_0'^2 - 143]$: Birch, 1978). The frequency shifts with pressure of all modes are positive, except for the ν_2 and $2\nu_2$ vibrations (the CO_3 out-of-plane bend and its

overtone). The negative frequency shift of the ν_2 mode during compression has previously been explained for the aragonite structure (*Pmcn* symmetry) as resulting from the dominance of a negative force constant, produced by coupling between neighboring carbonate anions, over the positive force constant associated with the bending vibration of an isolated carbonate ion during compression (Decius, 1955; Kraft et al., 1991).

Negative frequency shifts of the ν_2 or $2\nu_2$ mode during compression have also been observed in a range of carbonate minerals, including calcite, strontianite, magnesite, dolomite, shortite, and bästnasite (Gillet et al., 1993; Vennari and Williams, 2018; Bayarjargal et al. 2018; Vennari et al., 2018; Efthimiopoulos et al., 2019; Vennari and Williams, 2019). The trajectory of the ν_2 mode toward lower frequencies upon compression has substantial consequences for the evolution of the bütschliite spectrum, contributing to the development of a complex resonance phenomenon between the ν_2 and ν_4 vibrations observed at higher pressures.

The spectrum of bütschliite-II is remarkably similar to the ambient-pressure spectrum of $Sr_2Mg(BO_3)_2$ presented by Lv et al. (2018), which also belongs to the *C*2/*m* space group, providing independent confirmation of our single-crystal refinements. In order to semi-quantitatively compare the spectra of the borate relative to the carbonate in $Sr_2Mg(BO_3)_2$ and $K_2Ca(CO_3)_2$, we use the quantity

$$\xi_{A-B} = \sqrt{\frac{Z_A Z_B}{r^3 \mu}} \tag{3.3}$$

where A and B are bonded elements, Z is the charge, r is the bond length (with values taken from Shannon, 1976), and $\mu = m_A m_b/(m_A + m_B)$ is the reduced mass. This relation is simply derived from Coulombic interactions coupled with harmonic oscillators. For the anions under consideration, $\xi_{B-O} = 0.61$ and $\xi_{C-O} = 0.75$. The ratio of these quantities,

$$\chi = \frac{\xi_{C-O}}{\xi_{B-O}} \tag{3.4}$$

serves as a scaling factor with $\chi = 1.23$. Application of this scaling factor to the ambient pressure fits of the bütschliite-II carbonate modes recovers the borate mode frequencies of $Sr_2Mg(BO_3)_2$ to within 0.2 to 7.5%, with the largest deviation being for the asymmetric stretching vibration of the carbonate group (ν_3), which is anticipated to be substantially affected by the surrounding cations.

The spectra of bütschliite-II also show some novel spectroscopic features (Figure 3.10). Specifically, Fermi resonance occurs when the wave functions of two vibrational modes with the same symmetry and similar energies mix. In vibrational spectra, the phenomenon manifests as the frequencies of two resonating peaks, ν_- and ν_+, following a hyperbolic trajectory and exchanging intensity. We observed a Fermi resonance in the lattice modes of bütschliite-II, spanning from 9 to 29 GPa (Figure 3.10). By comparing the spectra of the bütschliite-II with the calculated spectrum of $Sr_2Mg(BO_3)_2$ from Lv et al. (2018), we are able to infer that the resonating modes each have A_g symmetry and involve vibrations of K^+ against $[CO_3]$ units. The coupling constant, representing the semi major axis of the hyperbola in pressure-frequency

space, is δ = 9.27 cm^{-1} and the maximum resonance occurs at 19.7 GPa. Following Shimizu (1985), we calculated the unperturbed frequencies ν_a and ν_b (Figure 3.10b), which represent the frequency trajectories the peaks would follow in the absence of resonance:

$$\nu_a = \frac{\nu_+ + \nu_- + \sqrt{(\nu_+ - \nu_-)^2 - 4\delta^2}}{2} \tag{3.5}$$

$$\nu_b = \nu_+ + \nu_- - \nu_a \tag{3.6}$$

A notable feature of the bütschliite-II Fermi resonance is the nearly linear trajectory of the high frequency resonating peak, ν_+ (Figure 3.10b). Despite the asymmetric trajectories of the resonating peaks, the diagnostic intensity exchange between the peaks is clearly present over the duration of the resonance (Figure 3.10c). The resonating modes, and indeed all Raman-active lattice modes in the *C*2/*m* phase, only involve motion of the carbonate and potassium ions. The ν_+ vibration involves intralayer motion, while the ν_- vibration involves interlayer stretching and is dominated by the K-CO_3 motion mostly along the *c*-axis. This axial direction is more compressible than the direction associated with the vibration in the *ab*-plane of ν_+, resulting in the pronounced stiffening of the ν_- mode during compression. Hence, this resonance provides separate confirmation of the relative compressibilities of the different axes of the crystal that were characterized using single-crystal diffraction, and verifies that these structural trends persist to substantially higher pressures than the single-crystal data probe.

3.3.6 Subsequent phase transitions

We observe three more phase transitions in the Raman spectra, which are also manifested in the powder diffraction data (Figure SI 4): because of their narrow spacing in pressure, the Raman data provide better constraints on the transition pressures. There are two transitions to phases with limited stability ranges, bütschliite-III and bütschliite-IV, followed by a transition to bütschliite-V, which appears to be stable up to our highest-pressure measurement at 94.1 GPa. The first indications of a transition from bütschliite-II to bütschliite-III occur at 27.8 GPa, with the appearance of a low-frequency peak associated with the ν_1 vibration at 1179 cm^{-1} (Figure 3.11c). In the next pressure step, at 28.9 GPa (shown in Figure 3.11c), the lattice modes broaden and decrease in intensity, a new high-frequency component associated with the ν_2 vibration grows in at 898 cm^{-1}, the low-frequency component of the $\nu_1$vibration increases in intensity, and high-frequency components of both ν_3 peaks appear. The ν_1 peak of bütschliite-II loses intensity with increasing pressure and is fully absent by 35.2 GPa. Hence, the increase in band multiplicity of the ν_2 and ν_3 peaks are compatible with an expanded unit cell and/or a larger number of distinct carbonate groups within bütschliite-III relative to the *C*2/*m* structured bütschliite-II. This inferred decrease in symmetry is supported by the x-ray data, which show a bifurcation of the d-spacing associated with the $(20\bar{2})$ plane at ~26 GPa (Figure SI 4a). The lower frequency of the symmetric stretch (ν_1) in bütschliite-III might be associated with a lower force constant/longer distance of the C-O bonds, while the higher frequency components of the asymmetric stretches (ν_3) might indicate a stronger interaction with neighboring cations (possibly within a subset of carbonate sites). The net decrease in symmetric

stretching (ν_1) frequency at this transition is roughly 15 cm^{-1}; this is a substantially smaller decrement than that associated with the onset of 3+1 coordination of carbonate groups (Vennari and Williams 2018; Vennari et al., 2018), which generates a decrement of ~50 cm^{-1}. This could be the triclinic $P\bar{1}$ structure predicted by Hou et al. (2022) to occur at 3.3 GPa, and Tian et al. (2023) to become stable at 10.3 or 10.5 GPa. While we do not preclude this possibility, it is notable that Hou et al. (2022) predicts essentially constant C-O distances between the *C*2/*m* and $P\bar{1}$ phases, which does not seem fully consistent with the change in the frequency of the symmetric stretch (ν_1) that we observe. In passing, we note that the clear doublet associated with the ν_4 vibrations likely precludes this phase from being associated with the nyererite ($Na_2Ca(CO_3)_2$) structure: only a single ν_4 band is observed in this structure (Vennari et al. 2018; Rashchenko et al. 2018).

The transition to bütschliite-IV occurs around 30.4 GPa in Ne. The onset of this phase is marked by the concomitant splitting of the ν_2 vibration into a triplet and of the ν_3 vibration into a multiplet of peaks, as well as a bifurcation of the $(11\bar{1})$ spacing in the x-ray data at ~32 GPa (Figure SI 4a). There is also an increase in the intensity of the lattice mode around 400 cm^{-1}. By 35.2 GPa only a hint of the lowest frequency peak of the ν_2 triplet remains. At 38.4 GPa ν_3 reverts back to two peaks and the low frequency peak associated with ν_4 starts to broaden. By 39.3 GPa, the components of the ν_4 doublet have become substantially asymmetric. In this instance, the transition is relatively subtle: no major shifts in vibrational bands occurs, but there are changes in band multiplicities, with new bands being observed.

The transition to bütschliite-V is more dramatic, and occurs between 37.4 and 39.7 GPa in silicone oil and above 39.3 GPa in Ne. At 45.3 GPa, ν_1 has split into several peaks (with at least two new components emerging on its low frequency side), and the ν_4 and ν_2 peaks become significantly broadened and distorted. Splitting of the ν_1 vibration indicates the presence of multiple (possibly 4) distinct carbonate units within the unit cell, and the lowered frequency of these bands implies that a portion of the C-O bonds in the structure have weakened. The ν_3 vibration becomes unresolvable beyond 50.6 GPa. The convergent trajectories of the ν_2 and ν_4 vibrations result in a complex resonance phenomenon that initiates at around 70 GPa (Figure 3.6b).

The separation between the ν_2 and ν_4 vibrations vanishes near 70 GPa, and the coalesced peaks move together as a single unit upon further compression. While there is no evidence to suggest that the wave functions of the two vibrations are mixing, the energy of the vibrations are clearly becoming similar. In effect, the in-plane and out-of-plane bending vibrations of the carbonate unit have become energetically identical, and components associated with the two types of molecular vibrations span across a frequency range approaching 150 cm^{-1}. Given the breadth of this bending region, it is certainly possible that combination bands of lattice modes as well as possible difference modes may be resonance enhanced by the bending vibrations, contributing minor, and possibly broad, peaks to this spectral region. A similar phenomenon was observed in dolomite-III (Vennari and Williams, 2018) at similar pressures, and could possibly be an intrinsic feature of low-symmetry double carbonates subjected to very large compressions.

Notably, there is no indication of an increase in coordination associated with the carbonate group towards a 3+1 coordination, as has been observed in dolomite-III and shortite under pressure (Vennari and Williams 2018; Vennari et al. 2018). The principal manifestation of this change, a softening or lowered frequency of the ν_1 symmetric stretching vibration, does not occur up to 94 GPa in this material. This maintenance of the three-fold coordinate carbonate unit can likely be correlated with the maintenance of the layered-like overarching structure associated with the two lowest pressure phases: the next-closest oxygen to the carbonate units typically defines the edge of a cation polyhedron (e.g., Figure 3.1).

3.3.7 Compressibility of compositionally and structurally diverse carbonate phases

The evident rigidity of trigonal [CO_3] units in solid carbonate phases indicates that the cations play a dominant role in volumetric reduction during isothermal compression. Here, we explore the relationship between cation radius and compressibility for three groups of compositionally diverse and geologically important carbonate mineral structures: the broadly-defined "double carbonates" including bütschliite, the calcite-structured group, and the aragonite-structured group.

Figure 3.12 shows the relationship between the isothermal bulk modulus, K_T, and average non-carbon cation radius (a proxy for bond strength) for minerals belonging to each of the three carbonate groups listed above. In the case of the double carbonates, the cation radius is determined by weighting each cation radius by its stoichiometric subscript and dividing by the total number of cations (excluding carbon)

in the chemical formula. It can clearly be seen that the value of the bulk modulus decreases with increasing cation radius. A linear fit to the double carbonate data yields $K_T = -94.7(21)r + 175.0(20)$ and a linear fit to all data points yields $K_T = -82.4(11)r + 161.3(12)$. While the separate structures and stoichiometries present in Figure 3.12 may each have modestly different trends (with the trend of the transition metal-bearing calcites having been noted previously by Sawchuk et al. 2021), the overarching trends are roughly comparable. Figure 3.12 thus illustrates a rather simple effect: the compaction of the carbonates is largely modulated by their charge-balancing cations. Deviations from this general trend (such as might be the case for bütschliite-II) may reflect the presence of more complex compressional mechanisms beyond simple compaction of the cation sites (such as angle changes, carbonate group rotations, and/or coordination changes).

3.4 Conclusions

Bütschliite is a highly compressible mineral that undergoes a series of four high-pressure phase transitions during isothermal compression up to 95 GPa. Compression of the ambient-pressure phase is highly anisotropic, with contraction along the *c*-axis (i.e., reductions in K-O and K-Ca distances) accounting for most of the volume change in this material. Our results suggest that the ambient-pressure bütschliite phase is likely stable to a depth of about 180 km within the Earth; this stability range in depth is likely to be largely independent of geothermal variations.

Bütschliite converts to a monoclinic phase with *C*2/*m* symmetry at ~6 GPa. Compression of this phase is controlled by interlayer shifting and rotation of the

carbonate groups. This new compression mechanism provides additional means of compaction that are unavailable to the low-pressure phase, and results in a more compressible structure. The enhanced compressibility of the *C*2/*m* structure likely augments the stability of the bütschliite-II phase, as the large $P\Delta V$ difference between the $R\bar{3}m$ phase (in its metastable region above ~6 GPa) and the more compressible *C*2/*m* phase (and possibly the hypothesized $P\bar{1}$ phase) will result in an expanded stability field in the phase diagram. A Fermi resonance observed in the lattice modes of bütschliite-II provides independent confirmation of the relative compressibilities of different axes that were characterized with single-crystal x-ray diffraction. Our results, when kinetic effects are considered, indicate that bütschliite inclusions found in deep-formed diamonds (e.g., Logvinova et al., 2019) likely initially crystallized as the *C*2/*m* phase and reverted to the $R\bar{3}m$ phase during ascent through the mantle or following emplacement. Furthermore, our results also indicate that previous phase equilibrium experiments in alkali carbonate systems (e.g., Shatskiy et al., 2015) may not have crystallized bütschliite at 6 GPa, but rather the *C*2/*m* phase, which reverts to bütschliite upon quenching.

Subsequent phase transitions observed in the Raman data show progressive distortion of carbonate units, ultimately giving rise to new distinct carbonate units within the structure and possibly expansion of the unit cell. Nevertheless, the overarching layer-type structure appears to be maintained at 300 K across these transitions. The stability of bütschliite-V to very high pressures suggests that this phase

could, if stable at high temperatures, play an important role in deep Earth alkaline carbonate storage and magmatism.

Chapter 4: High-temperature Raman spectroscopy of $K_2Ca(CO_3)_2$ bütschliite and $Na_2Ca_2(CO_3)_3$ shortite

4.1 Introduction

Bütschliite and shortite are alkali-calcium carbonate minerals with chemical formulas $K_2Ca(CO_3)_2$ and $Na_2Ca_2(CO_3)_3$, respectively; they each represent structurally different manifestations of double carbonates. Bütschliite crystallizes in the hexagonal system (space group: $R\bar{3}m$) with three formula units per unit cell and shortite crystallizes in the orthorhombic system (space group: $Amm2$) with two formula units per unit cell. The structure of bütschliite is characterized by sheets of planar [CO_3] units stacked on interstitial Ca^{2+} and K^+ cations (Pabst, 1974). The lower symmetry of shortite is in accord with its more complex structure, which is characterized by the presence of three distinct cation sites (one Ca^{2+} and two Na^+ sites) and two distinct [CO_3] sites (Dickens et al., 1971). While bütschliite and shortite do not form a solid solution, minerals that they convert to at high temperatures, fairchildite and nyerereite ($Na_2Ca(CO_3)_2$), do. Indeed, nyerereite samples from the natrocarbonatites of Oldoinyo Lengai in Tanzania have been reported with between 6-9 wt% K_2O (Zaitsev et al., 2009). Shortite has been observed in the groundmass of magmatic carbonatites (Zaitsev and Chakhmouradian, 2002), and both phases have been observed within melt inclusions in olivine and/or diamond (Mernagh et al., 2011; Logvinova et al., 2019; Abersteiner et al., 2022). Thus, the behavior of these two phases at extreme conditions of pressure and/or temperature are highly relevant to the behavior of alkali-rich carbonate materials, and hence carbon cycling, within Earth's interior.

Previous studies have documented extensive high-pressure polymorphism in both shortite and bütschliite. In a high-pressure study on shortite, Vennari et al. (2018) reported a transition to a crystalline monoclinic phase, shortite-II (space group: *Pm*), at 15 GPa followed by a transition to an amorphous phase above 22 GPa. Additionally, they report the existence of a high-temperature/high-pressure crystalline phase, shortite-III, generated at pressures between 12 and 30 GPa and $T > 1300$°C. Below 12 GPa, shortite-III decomposes into a mixture of shortite, nyerereite, and aragonite. In their high-pressure study of bütschliite, Zeff et al. (2024) documented four phase transitions up to 94 GPa. At 6 GPa, bütschliite converts to a monoclinic phase (space group: *C*2/*m*); this lowest pressure transition was also observed in other Raman experiments (Likhacheva et al., 2024). Raman measurements from Zeff et al. (2024) indicate the onset of subsequent phase transitions at 28, 34, and 37 GPa.

High-temperature phase transitions have been previously documented in both bütschliite and shortite. In synthesizing samples of bütschliite for his x-ray diffraction measurements, Pabst (1974) bracketed the isochemical bütschliite-fairchildite transition between 505°C and 585°C at ambient pressures. A novel feature of this transition is that it involves partial disordering of the carbonate ions in the quenched high-temperature phase, fairchildite (Pertlik, 1981): at 300 K, one of the two crystallographically distinct carbonate sites (C(2)) shows orientational disordering of the oxygens around the carbon location. Cooper et al. (1975) studied the K_2CO_3-$CaCO_3$-Na_2CO_3 ternary system and reported a bütschliite-fairchildite transition temperature of 547°C at 1 kbar. Calorimetry measurements conducted by Navrotsky et

al. (1997) determined enthalpy and entropy changes of $\Delta H_{büt \rightarrow fc} = 33.6 \pm 4.2$ kJ/mol and $\Delta S_{büt \rightarrow fc} = 40.9 \pm 5.1$ J/mol·K. Assuming that bütschliite and fairchildite have similar thermal expansions, this value of the entropy change and the density difference reported by Pabst (1974) yield a Clapeyron slope of $dT/dP \sim 145$ K/GPa for this transition, implying an enhanced stability field of bütschliite at high pressures relative to fairchildite. This slope is in general accord with the lack of observation of fairchildite stability at 3 GPa (Arefiev et al., 2019). The thermal properties of shortite were measured at The Bureau of Mines, with the decomposition reaction:

$$Na_2Ca_2(CO_3)_3 \text{ (shortite)} \rightarrow Na_2Ca(CO_3)_2 \text{ (nyerereite)} + CaCO_3 \text{ (calcite)} \quad (4.1)$$

being observed at 470°C. Using differential scanning calorimetry, they determined $\Delta H_{shor \rightarrow nyer+cal} = 28.8$ kJ/mol (Johnson et al., 1974).

In order to examine the nature of *in situ* disordering processes within these phases at high temperatures, we have conducted high-temperature Raman spectroscopy measurements on bütschliite and shortite under vacuum. We document the spectroscopic signature of two high-temperature phase transitions in each mineral: the previously thermochemically characterized transitions, and their subsequent decarbonation reactions. Notably, both shortite and bütschliite convert to disordered phases before undergoing decomposition reactions at higher temperatures. These results shed light on not only the behavior of vibrational modes at high temperatures in these phases, but also the stability of alkali double carbonate minerals at high temperatures.

4.2 Methods and sample synthesis

The shortite sample used in this study is from the FMC Westvaco mine in Sweetwater County, Wyoming, USA. Crystals of bütschliite were synthesized via the hydrothermal *method (E)* of Pabst (1974). Briefly, small chunks of optical quality calcite were immersed in a saturated solution of K_2CO_3 and held at ~70°C. In this method, crystals of $K_2Ca(CO_3)_2$ begin to grow on the cleavage surfaces of the calcite within a few days. Raman spectra were collected with a Labram HR Evolution spectrometer and a 532 nm diode excitation laser nominally rated at 50 mW. A diffraction grating with a grating density of 1200 lines/mm was used for all measurements with a spectral resolution on the order of 1 cm^{-1}. Samples were heated under vacuum in a Linkam TS1500 heating stage with temperature controlled by a T96 system controller. The typical precision of the temperature control is < 1°C. All high-temperature data were collected on samples that were initially single crystals. Typical heating rates of the samples were 20-40°C/min, with the sample held at temperature for 10-60 minutes while spectra were taken. A thin layer of platinum foil was placed between the sample and sapphire sample holder to prevent chemical reactions from occurring with the samples at high temperatures.

4.3 Ambient Raman spectra of bütschliite and shortite

The ambient Raman spectra of bütschliite and shortite are shown in Figure 4.1. The spectra agree well with previous ambient pressure Raman spectra of these materials (Arefiev et al., 2019; Vennari et al., 2018). Factor group analysis of bütschliite yields

$$\Gamma_{\text{optic}} = 4A_{1\text{g}} + A_{1\text{u}} + A_{2\text{g}} + 4A_{2\text{u}} + 5E_{\text{u}} + 5E_{\text{g}} \quad (4.2)$$

Here, the A_{1g} and E_g symmetry modes are Raman active. Similarly, factor group analysis of shortite yields:

$$\Gamma_{\text{optic}} = 14A_1 + 7A_2 + 10B_1 + 14B_2. \quad (4.3)$$

For the lower symmetry shortite structure, all modes are Raman active. Notably, the factor group analysis carried out here for shortite proceeds from a primitive unit cell containing 16 atoms ($Z = 1$), while the crystallographic unit cell for shortite contains 32 atoms ($Z = 2$). Hence, there are fewer than the anticipated $3N - 3$ optic vibrations associated with the X-ray unit cell.

4.4 High-temperature Raman spectra of bütschliite

All of the observed Raman modes of bütschliite shift to lower frequencies upon heating except for the lowest frequency lattice mode that lies initially at 68 cm^{-1} and the υ_4 in-plane bending vibration (Figure 4.2 and Table 4.1). The υ_4 in-plane bending vibration remains essentially constant in frequency during heating. Such near-constant-frequency or positive thermal shifts of vibrations of this type have been observed for aragonite-structured phases (e.g., Gillet et al., 1993; Wang et al., 2019), but not for calcite-related phases or, notably, other double carbonates (e.g., Gillet et al., 1993; Farsang et al., 2018). For comparison, the ν_4 in-plane bending mode of dolomite (space group: $R\bar{3}$), which is structurally similar to bütschliite, exhibits a frequency shift of $-0.0021 - 1.7\ (10^{-5}\ T)$ (Gillet et al., 1993). The stationary behavior of the in-plane bending mode of bütschliite likely results from a combination of anisotropic expansion of the unit cell along the *c*-axis, seen in both aragonite and dolomite (Reeder and Markgraf, 1986; Ye et al., 2012), and the orientation of the trigonal planar [CO_3] units

in the unit cell. The [CO_3] units in aragonite are perfectly aligned, the [CO_3] units in bütschliite are slightly offset, and the [CO_3] units in dolomite are substantially offset (Figure 4.3). The alignment of sheets of [CO_3] units in the aragonite and bütschliite unit cells results in a coupling of the [CO_3] units between layers. This coupling is weaker for the dolomite structure, where the [CO_3] units are misaligned. The thermal expansion within the plane of the [CO_3] is small, while the distance to neighboring metal cations increases and the associated in-plane bending vibration is correspondingly temperature-insensitive as the coupled [CO_3] units move away from each other during heating in the bütschliite unit cell. Although no thermal expansion measurements have been conducted on bütschliite, under pressure the *c*-axis is by far the most compressible (e.g., Zeff et al., 2024), and the thermal expansion of the material can be anticipated to be highest in the between-layer, *c*-axis direction. Based on the negligible frequency shift and moderate broadening of the peak (Figure 4.4), we infer that the in-plane bending mode of bütschliite represents very nearly ideal harmonic behavior during heating.

The location of the lowest frequency lattice mode is the least well-resolved of any mode during heating, but the overarching data are consistent with a shift between +0.005 and -0.001 cm^{-1}/°C. Here, this small shift is compatible with the behavior of this band under pressure (Zeff et al., 2024; Likhacheva et al., 2024): while not soft, its pressure shift is anomalously small for a low frequency lattice mode. The asymmetric stretching υ_3 mode is the only vibration that exhibits any curvature in its frequency-temperature trajectory over the stability range of bütschliite during heating; this peak

also broadens substantially more during heating than any of the other internal carbonate vibrations (Figure 4.4). Why this mode, out of the four carbonate internal modes, appears to be the most susceptible to anharmonic effects is not entirely clear. Nevertheless, we speculate that the broadening and non-linear shift of this band could be associated with its progressively closer proximity to the (unobserved) $2\upsilon_4$ overtone as higher temperatures are accessed. In this context, Raman linewidths at high temperatures have been shown to vary depending on multi-phonon interactions (e.g., Balkanski et al., 1983).

While the initiation of the transition from bütschliite to fairchildite is tightly constrained in our measurements to between 568 and 571°C (roughly 20°C hotter than the temperature reported by Cooper et al. (1975) at 1 kbar), the transition is characterized by a mixed phase regime that persists until 595°C. Indeed, the transition proceeds inhomogeneously across the sample, with different regions showing fairchildite-like and bütschliite spectra across this ~25°C interval. This observation strongly suggests that the transition may be kinetically impeded, with nucleation and growth processes controlling the conversion to the high-temperature phase. The first appearance of the new phase can be seen in the spectrum at 571°C (Figure 4.5). The low frequency region of this spectrum appears to be a mixture of the two most intense lattice modes of bütschliite and the broad feature associated with the intrinsically disordered structure of fairchildite. The υ_4 in-plane bending vibration of bütschliite is still present in spectra at this temperature, but there is also a high frequency component of lower intensity; the υ_2 out-of-plane bending vibration is absent. The υ_1 symmetric

stretching vibration is dominated by fairchildite, however a small component of the bütschliite symmetric stretching vibration persists on the high frequency side of the peak. The asymmetric stretching vibration is absent from this spectrum, in accord with the spectrum of fairchildite. Figure 4.6 shows deconvolution of a representative fairchildite spectrum measured at 637°C. The low frequency feature in Figure 4.6a is fit with seven peaks. The ν_4 in-plane bending mode is fit with two peaks: the low and high frequency peaks have widths 33 and 22 cm^{-1}, respectively. The ν_1 symmetric stretching vibration is also fit with two peaks: the low and high frequency peaks have widths 19 and 22 cm^{-1}. The broad peaks of the internal carbonate vibrations suggest that both carbon sites are disordered.

Notably, our measurements indicate that the high-temperature/ambient-pressure stability field of fairchildite is limited, as a second phase transition initiates around 663°C. Based on the previous thermoanalytical work of Winbo et al. (1998), we infer that this transition represents the decomposition of fairchildite into K_2CO_3 and CaO. CaO does not have a first order Raman spectrum and we do not resolve any second order features in the spectrum of the quenched sample. Hence, based on our high-temperature measurements conducted in vacuum, we bracket the stability field of fairchildite at ambient pressure to the temperature range 570-665°C.

4.5 High-temperature Raman spectra of shortite

With the exception of a single in-plane bending vibration, all of the vibrational modes of shortite shift to lower frequencies during heating and shift linearly within the resolution of the data (Figure 4.7 and Table 4.2). In contrast to the high-temperature

behavior of some other carbonates (e.g., Gillet et al., 1993; Farsang et al., 2018; Wang et al. 2019), the lattice modes of bütschliite and shortite do not systematically shift faster than the internal CO_3 vibrations. The two highest frequency lattice modes of shortite are closely spaced, with initial ambient temperature frequencies of 260 and 266 cm^{-1}, and by 200°C they coalesce to the degree that they can be fit well with a single peak. Unlike bütschliite, the υ_4 in-plane bending modes of shortite (labelled υ_{4a-d} from low to high frequency) all shift measurably during heating. Three of the in-plane bending modes, υ_{4a}, υ_{4b}, and υ_{4d}, shift to lower frequencies, while υ_{4c} shifts to higher frequency; because of both the comparative complexity of the shortite structure and of this spectral region, correlating these shifts with possible anisotropy in compression or expansion is challenging. The two ν_1 symmetric stretching vibrations, both with A_1 symmetry, shift at modestly different rates. The lower frequency ν_{1a} peak shifts about 27% faster than the higher frequency ν_{1b} peak: this lower frequency peak is associated with the C(2) carbon environments, which lie within the *b*-*c* plane in this structure (Vennari et al., 2018), while the more distorted C(1) environment (the highest frequency band) is sensitive to expansion along each crystallographic direction. Within shortite, the *c*-axis is also the most compressible (Vennari et al., 2018), and hence is likely to undergo the largest thermal expansion among the axes. In contrast, the ν_3 asymmetric stretching vibrations, which do not share the same symmetry, exhibit considerably more variation in their thermal shifts. The four lowest frequency asymmetric stretching vibrations (i.e., ν_{3a-d}), with respective symmetries of A_1, A_2, B_1, and A_1, shift with rates between -0.0179 and -0.0275 cm^{-1}/°C. The higher frequency ν_{3e}

and ν_{3f} vibrations, with B_2 symmetry, shift at a rate of -0.049 cm^{-1}/°C. The five overtones we observe in the shortite spectrum fall into two clusters (Figure 4.7f). The first cluster contains the overtones with initial frequencies of 1699 and 1706 cm^{-1}. These vibrations exhibit a very weak and nearly parallel frequency shift during heating. The second cluster of overtones contains the modes initially at frequencies of 1727, 1732, and 1742 cm^{-1}. The frequency shifts of these three overtones are also nearly parallel, but exhibit a much stronger temperature dependence than the modes in the lower frequency cluster. A possible explanation for these two clusters lies in the possible nature of the combination bands: the higher frequency cluster's shifts lie close to twice that of the single υ_2 Raman band for which we document the temperature dependence (Figure 4.7c). Within the infrared spectrum of shortite, the lowest lying υ_2 vibration is at 851 cm^{-1} (White, 1974), or close to half the frequency associated with the lower overtone cluster. Therefore, the lower frequency cluster may involve combinations with infrared-active vibrations, and the differing temperature shifts may indicate that these lower-lying infrared υ_2 vibrations may have markedly smaller thermal shifts.

We observe the onset of the shortite-nyerereite transition at 535°C (Figure 4.8), a substantially higher temperature than the values of 335°C and 400°C reported by Cooper et al. (1975) at 1 kbar and 470°C reported by Johnson et al. (1974) at near ambient pressure. These results suggest that either very modest increases in pressure substantially reduce the stability field of shortite at high temperatures, and/or kinetics play a major role in this transition. The decomposition of shortite forms calcite and

nyerereite at low pressures (Cooper et al., 1975), and at higher pressures the decomposition reaction yields aragonite and $Na_2Ca_3(CO_3)_4$ (Podborodnikov et al., 2018) or aragonite and $Na_2Ca_4(CO_3)_5$ (Shatskiy et al., 2013).

The Raman spectrum of shortite does not uniformly convert to nyerereite at 535°C. The baseline underlying the low frequency region and the lattice modes of shortite smoothly and continuously increases and broadens up to the onset of the nyerereite transition at 535°C. A further temperature increase of 5°C results in a dramatically different spectrum at 540°C, with a low frequency region that is in accord with a strongly disordered nyerereite phase. Similarly, the amplitude of the υ_{1a} symmetric stretching mode gradually decreases up to 535°C and the space between the two symmetric stretching vibrations is uplifted. At 540°C the υ_1 symmetric stretching vibration is in a new regime in which it requires three components to fit. Unlike the υ_1 symmetric stretching and lattice modes, the υ_4 in-plane bending vibrations and υ_3 asymmetric stretches do not smoothly transition into the new phase at 540°C. The ν_4 in-plane bending vibrations broaden and merge up until 535°C, at which point they do not show any indications of a new phase. Then, at 540°C, an asymmetric υ_4 in-plane bending peak that can be fit with two components becomes the dominant feature. At higher frequencies, we track six asymmetric stretching ν_3 modes and five combination/overtone bands up to 530°C. At 535°C these eleven peaks are abruptly replaced by two peaks that roughly correspond to the asymmetric stretching and overtone/combination regions.

A second phase transition initiates at 700°C. This transition is marked by broadening of the υ_1 symmetric stretching and ν_4 in-plane bending vibrations, and the appearance of two new peaks around 630 cm^{-1} and 990 cm^{-1}. The latter peak location is at an anomalously low frequency for a typical resonance-stabilized carbonate group and, if associated with C-O bonding, appears likely to be associated with destabilization of the carbonate group. By 715°C, no spectral features associated with nyerereite remain. This transition likely represents the decomposition of nyerereite into α-Na_2CO_3 (a high-temperature polymorph of natrite) or possibly to an adsorbed transient species such as $NaCO_3^-$ (Ballirano, 2011; Carper et al., 2012) that is a close precursor of decarbonation. In computational studies, Zhao et al. (2013) and Zhao et al. (2015) modeled decarbonation pathways of $CaCO_3$ and $MgCO_3$ and identified a suite of possible transient species that could form just prior to decarbonation. While these species have been challenging to observe experimentally, highly localized bonding effects associated with heterogeneous decarbonation and the metastable retention of carbonate could be conducive to preserving transient species that are in accord with our measured spectra.

4.6 Anharmonic properties of bütschliite and shortite

The isothermal and isobaric mode Grüneisen parameters, γ_{iT} and γ_{iP}, are commonly used to quantify the frequency dependent contributions to anharmonicity of a crystalline solid during compression and heating. In the idealized case of a crystal with a fully harmonic bonding environment, peaks would remain stationary during heating and compression and both quantities would be equal to zero. For the special

case in which frequency shifts depend only on changes in volume, the isothermal and isobaric Grüneisen parameters are equivalent and the bonding environment is said to be *quasiharmonic*. In the absence of experimental thermal expansion data for bütschliite and shortite, we use the quantity $-\alpha\gamma_{iP}$ as a proxy for the isobaric mode Grüneisen parameter. Figure 4.9 shows that the major contributions to anharmonicity for bütschliite and shortite come from the lattice modes. This is in accord with high-pressure experiments, in which the largest values of γ_{iT} correspond to the lattice modes (Vennari et al., 2018; Zeff et al., 2024).

The shift of the ν_4 in-plane bending mode of bütschliite under isothermal compression is small but nonzero: $(\partial\upsilon/\partial P)_T = 2.48$ cm^{-1}/GPa (Zeff et al., 2024). In contrast, this mode neither shifts nor broadens significantly during heating, indicating near-harmonic behavior at high temperatures. The ν_3 asymmetric stretching mode of bütschliite shifts the fastest of the internal carbonate modes during both heating and compression, and broadens dramatically during heating, but has a relatively small value of γ_{iT} due to its high frequency. The ν_1 and ν_2 modes are anharmonic but, as shown in Figure 4.9, only account for small contributions.

The ν_4 in-plane bending mode and ν_2 out-of-plane bending mode of shortite also exhibit anomalous behavior. Vennari et al. (2018) reported that all four of the ν_4 in-plane bending modes shifted to higher frequency and identified the ν_2 out-of-plane bending mode as a soft mode during compression. The behavior of the ν_4 vibration is consistent with increasing force constants and shortening bond lengths in the carbonate unit, while the anomalous behavior of the ν_2 vibration was explained as a result of the

simultaneous strengthening of Ca/Na-O bonds and weakening of C-O bonds. Figure 4.7 shows that ν_{4a}, ν_{4b}, ν_{4d}, and ν_2 shift to lower frequencies during heating, consistent with weakening force constants and lengthening of bonds in the carbonate unit. The ν_{4c} vibration, however, shifts to higher frequency during heating. The shift of the ν_2 vibration to lower frequency and ν_{4c} vibration to higher frequency during heating and compression is indicative of a substantial isochoric or explicit contribution to anharmonicity. This contribution, $(\partial \nu_i(P,T)/\partial T)_V$, is equivalent to

$$\left(\frac{\partial ln v_i(P,T)}{\partial T}\right)_V = -\alpha(\gamma_{iP} - \gamma_{iT}), \tag{4.4}$$

where $\alpha = (1/V)(dV/dT)$, and is governed by the thermal population of vibrational levels (Lucazeau, 2003).

4.7 Conclusions

The identification of alkali-alkaline earth carbonate minerals and quenched melts in a compositionally and geographically diverse suite of mantle-derived rocks have fueled interest in the stability and thermodynamic properties of many of the "double carbonate" minerals. Particular interest has been paid to the Na-, Mg-, K-, and Ca-bearing phases. In this study, the Raman spectra of bütschliite and shortite were characterized under vacuum to 725°C and 715°C, respectively. Bütschliite begins to convert to the isochemical disordered phase fairchildite at 570°C. We document a mixed phase regime consisting of bütschliite and fairchildite to 595°C. Upon further heating, fairchildite decomposes to an assemblage of K_2CO_3 and CaO at 663°C. Shortite also converts to a largely disordered assemblage, composed of nyerereite and

disordered $CaCO_3$ at 535°C, followed by a subsequent decomposition reaction that initiates at 700°C: this latter reaction involves a phase with particularly weak C-O bonding, and may represent a transitional phase at the onset of decarbonation.

The limited stability of fairchildite at high-temperatures and ambient pressure is particularly notable: our results suggest that fairchildite is stable between 570°C and 660°C under vacuum. The high-pressure phase boundary of fairchildite has been suggested to lie between 0.1 and 3 GPa, with pressure slightly expanding the high-temperature stability (Arefiev et al., 2019). When fairchildite is preserved as an inclusion, the mineral could serve as a useful geothermometer for shallow silicic and carbonatitic melting and crystallization processes.

Figures

Figure 1.1 Mineralogy of the Martian mantle. Modified after Khan & Connolly (2008). Sp = spinel; opx = orthopyroxene; cpx = clinopyroxene; ol = olivine; gt = garnet; wds = wadsleyite; rwd = ringwoodite; TCBL = thermochemical boundary layer. The primary discontinuity associated with the Martian transition zone is at around ~14 GPa.

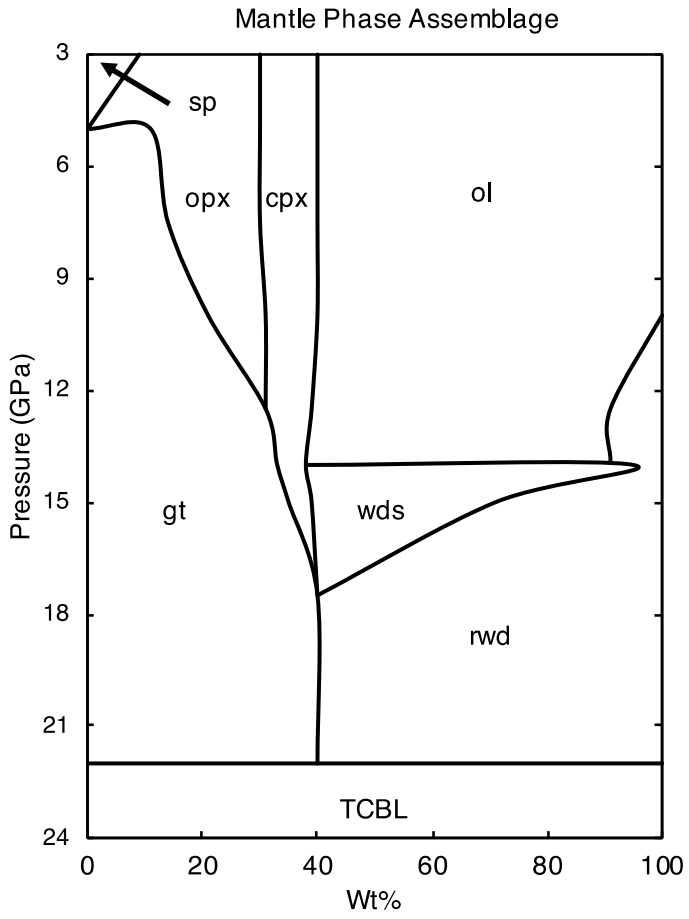
Mantle Phase Assemblage
Pressure (GPa)
3
6
9
12
15
18
21
24
sp
opx
cpx
ol
gt
wds
rwd
TCBL
0
20
40
60
80
100
Wt%

Figure 1.2 Density differences between residual liquid and coexisting solids ($\rho_{\text{liquid}} - \rho_{\text{solid}}$) at 3 GPa **(a)**. Shaded region represents conditions at which magma is dense enough to descend. Density differences between liquid and coexisting solids as a function of pressure for a range of melt compositions **(b)**. First appearance of solid phases for a fractionally crystallizing magma ocean, as derived from the pMelts simulations **(c)**. Opx = orthopyroxene; ol = olivine; gt = garnet; sp = spinel; cpx = clinopyroxene. Fractional crystallization proceeds to the right.

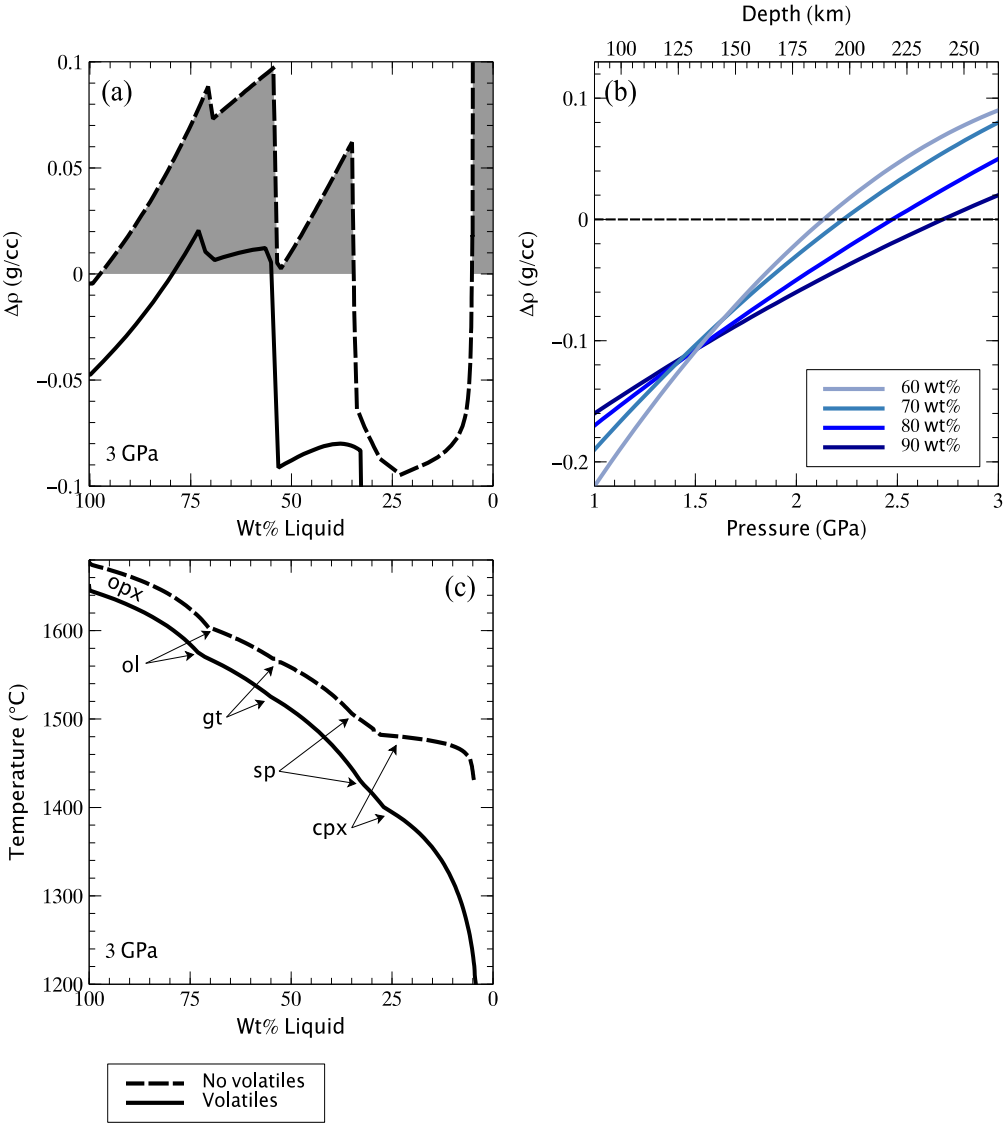
(a)
3 GPa
Δρ (g/cc)
Wt% Liquid
(b)
Depth (km)
Pressure (GPa)
60 wt%
70 wt%
80 wt%
90 wt%
(c)
opx
ol
gt
sp
cpx
Temperature (°C)
3 GPa
Wt% Liquid
No volatiles
Volatiles

Figure 1.3 Density profiles of Mars' mantle and fractionally crystallized magma ocean liquids **(a)**. Both of the mantle density profiles were calculated in BurnMan assuming an adiabatic temperature, starting at different initial temperatures. In **(b**-**f)** solid lines represent Assemblage 1 (a ringwoodite-dominated assemblage) and broken lines represent Assemblage 2 (garnet-dominated: see table 1.2); gray lines between 21 and 21.5 GPa represent the bulk lower mantle assemblage (gt + rwd). P-wave velocity of lower mantle and possible TCBL assemblages **(b)**. S-wave velocity of lower mantle and TCBL assemblages **(c)**. Density profile of lower mantle and TCBL assemblages **(d)**. P-wave impedance of the lower mantle and TCBL assemblages **(e)**. S-wave impedance of the lower mantle and TCBL assemblages **(f)**.

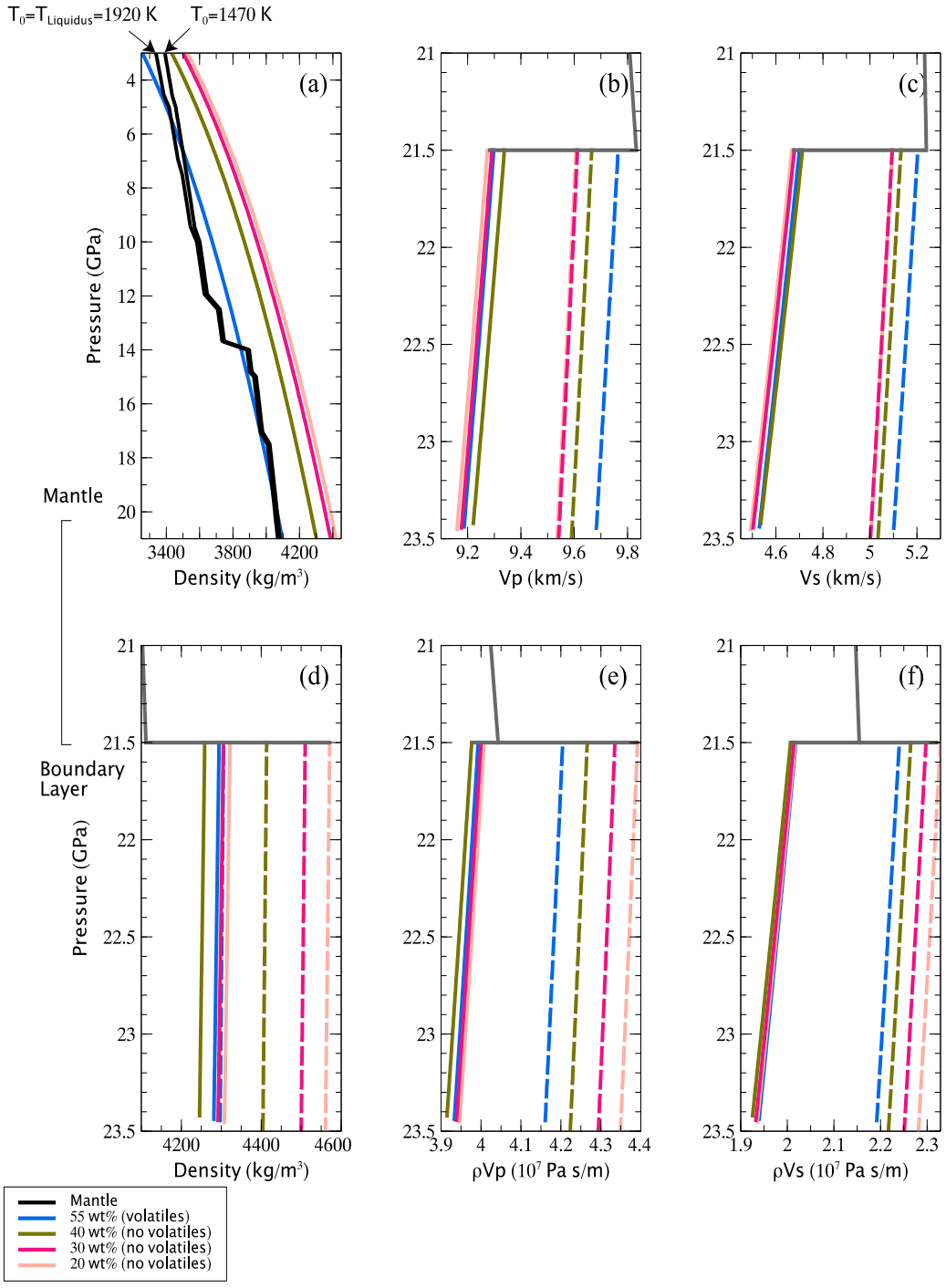
T0=TLiquidus=1920 K
T0=1470 K
(a)
(b)
(c)
(d)
(e)
(f)
Pressure (GPa)
Density (kg/m3)
Vp (km/s)
Vs (km/s)
ρVp (10^7 Pa s/m)
ρVs (10^7 Pa s/m)
Mantle
Boundary Layer
Mantle
55 wt% (volatiles)
40 wt% (no volatiles)
30 wt% (no volatiles)
20 wt% (no volatiles)

Figure 2.1 The $\bar{v}_{H_2O}$ dataset considered in this study over three different pressure ranges **(a-c)**. The 1223 K isotherm is from B&D71 and the 457 K isotherm is from Tkachev et al., (2005). References for each technique are listed in Table 2.1. Calculated fluid water isotherms, from Belonoshko and Saxena (1991), are shown for comparison. The fluid water isotherms are plotted from 1000 K to 6000 K at intervals of 1000 K. The cyan curves show the Hugoniots of fluid water from (high pressure) Mitchell and Nellis (1979) and (low pressure) Rice and Walsh (1957).

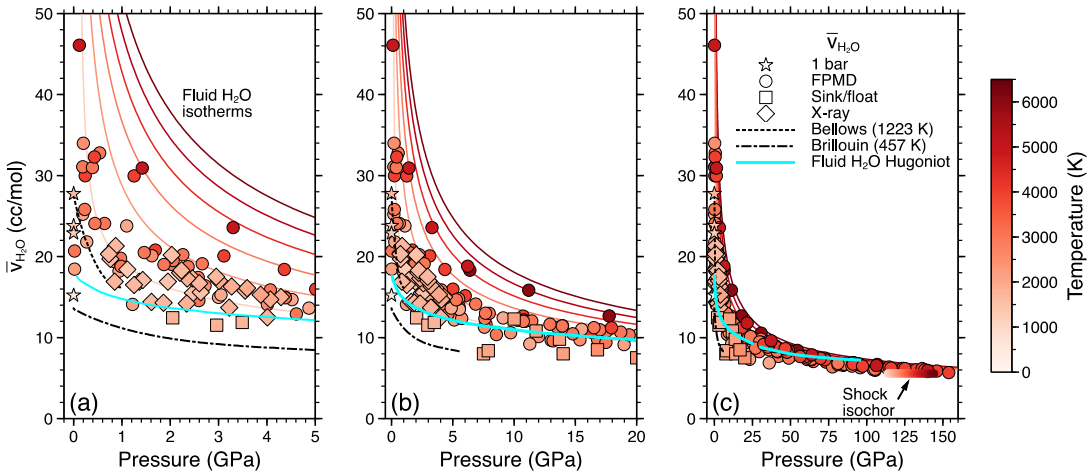
Fluid H2O isotherms
(a)
(b)
(c)
Pressure (GPa)
V̄H2O (cc/mol)
V̄H2O
1 bar
FPMD
Sink/float
X-ray
Bellows (1223 K)
Brillouin (457 K)
Fluid H2O Hugoniot
Shock isochor
Temperature (K)

Figure 2.2 The $\bar{v}_{H_2O}$ dataset binned according to temperature. Bins **(a-c)** contain the experimental data and bins **(d-h)** contain the FPMD data with a calculated shock-derived point at each temperature for comparison. Mean temperatures are reported in the upper right corner of each bin. References to individual studies are given in Table 2.1, and EOS fit parameters are given in Table 2.2.

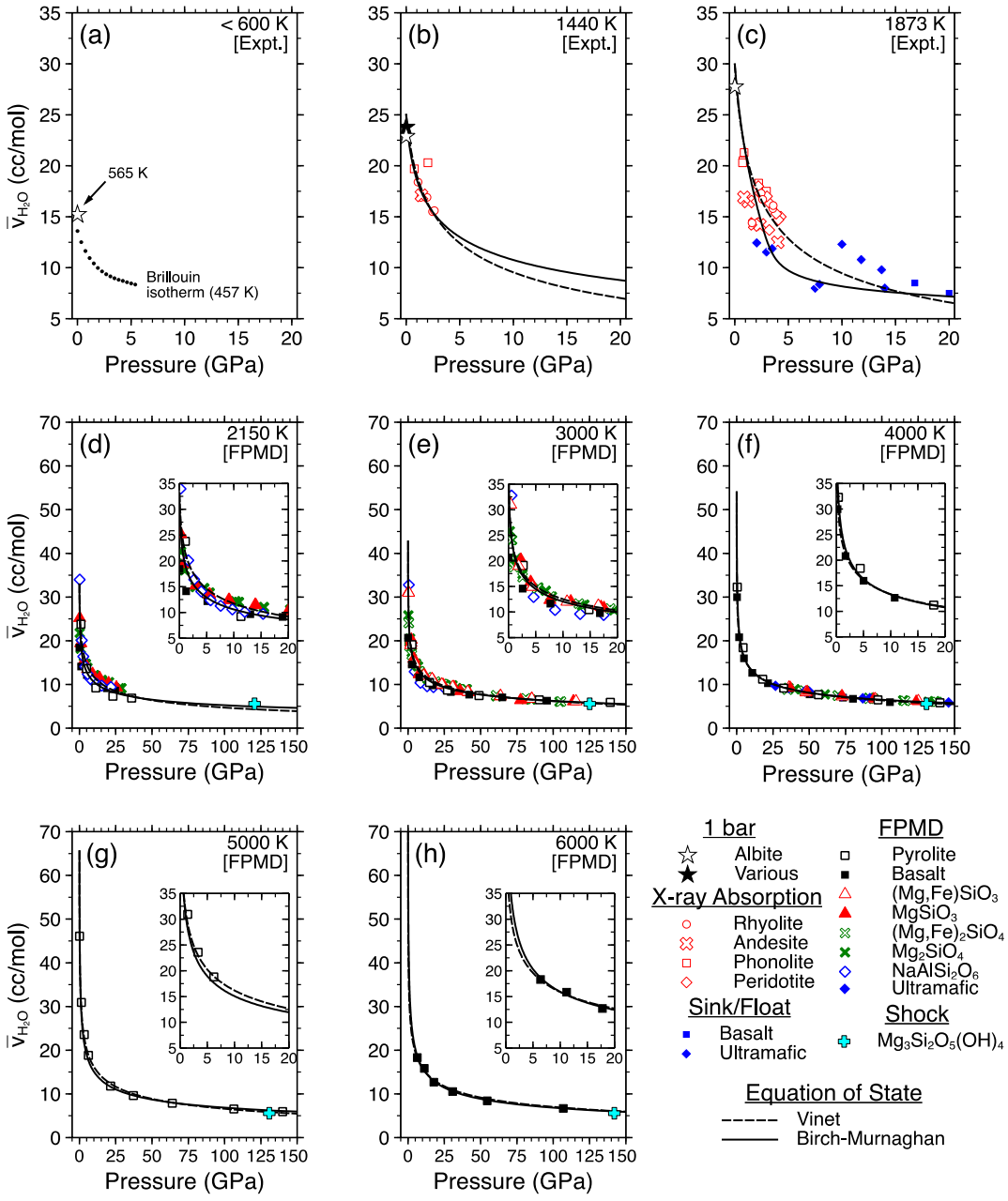
(a)
< 600 K
[Expt.]
565 K
Brillouin
isotherm (457 K)
(b)
1440 K
[Expt.]
(c)
1873 K
[Expt.]
(d)
2150 K
[FPMD]
(e)
3000 K
[FPMD]
(f)
4000 K
[FPMD]
(g)
5000 K
[FPMD]
(h)
6000 K
[FPMD]
$\bar{V}_{H_2O}$ (cc/mol)
Pressure (GPa)
1 bar
Albite
Various
X-ray Absorption
Rhyolite
Andesite
Phonolite
Peridotite
Sink/Float
Basalt
Ultramafic
FPMD
Pyrolite
Basalt
$(Mg,Fe)SiO_3$
$MgSiO_3$
$(Mg,Fe)_2SiO_4$
Mg_2SiO_4
$NaAlSi_2O_6$
Ultramafic
Shock
$Mg_3Si_2O_5(OH)_4$
Equation of State
Vinet
Birch-Murnaghan

Figure 2.3 Isotherms and thermal expansivity of the dissolved H_2O component in silicate melt. **(a)** Ambient pressure thermal expansion. FPMD curves (in color) at 0.5 GPa are from Dufils et al. (2020). Our 1 bar fit includes data from O&L97,99 and Bouhifd et al. (2015). **(b-c)** From bottom to top: 1273 K, 1473 K, and 1673 K Vinet and 3rd order Birch-Murnaghan isotherms calibrated relative to the 1440 K bin 2 data (Figure 2.2b). **(d)** Pressure dependence of the thermal expansion coefficient, parameterized with respect to pressure using Equation 9, with q = -0.5. The blue and red curves are calibrated to the 1440 K and 1873 K data (bins 2 and 3). The curve from Agee (2008b) extends the model of B&D71 to high pressure. The curve for fluid water is from Rice and Walsh (1957). **(e-f)** From bottom to top: 1873 K, 2073 K, and 2273 K Vinet and 4th order Birch-Murnaghan isotherms calibrated to the 1873 K data from bin 3 (Figure 2.2c). The FPMD data shown in the inset range from 2000-5000 K. The fluid H_2O isotherm was calculated with the EOS of Pitzer and Sterner (1994) at 1873 K.

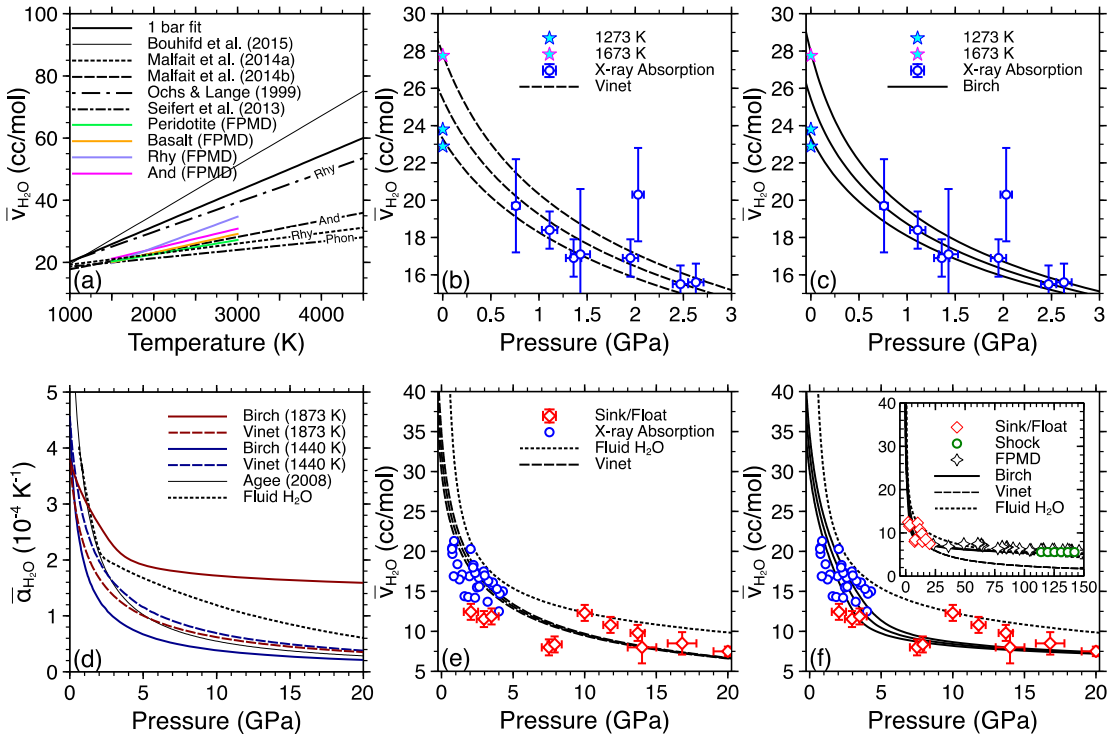
1 bar fit
Bouhifd et al. (2015)
Malfait et al. (2014a)
Malfait et al. (2014b)
Ochs & Lange (1999)
Seifert et al. (2013)
Peridotite (FPMD)
Basalt (FPMD)
Rhy (FPMD)
And (FPMD)
Rhy
And
Rhy
Phon
(a)
Temperature (K)
1273 K
1673 K
X-ray Absorption
Vinet
(b)
Pressure (GPa)
1273 K
1673 K
X-ray Absorption
Birch
(c)
Pressure (GPa)
Birch (1873 K)
Vinet (1873 K)
Birch (1440 K)
Vinet (1440 K)
Agee (2008)
Fluid H2O
(d)
Pressure (GPa)
Sink/Float
X-ray Absorption
Fluid H2O
Vinet
(e)
Pressure (GPa)
Sink/Float
Shock
FPMD
Birch
Vinet
Fluid H2O
(f)
Pressure (GPa)

Figure 2.2 Hydrous melt isotherms, pressure-density, and pressure-temperature relations in the Earth's mantle. **(a-d)** Hydrous melt compression curves calculated with the elastic- and volumetric-based mixing models for MORB (mid ocean ridge basalt) and IT8720 (high pressure partial melt of peridotite) compositions with up to 10 mol% H_2O. PREM is shown in green. **(e)** Hydrous melt compression curves plotted against PREM and solid mantle phases. Broken lines correspond to the volumetric mixing model; solid lines correspond to the elastic modulus mixing model. Numbers in parentheses show wt% H_2O. The slab density (Wang et al., 2020) is evaluated along the geotherm of Brown and Shankland (1981). The black curves show the densities of solid $Mg_{0.9}Fe_{0.1}$-silicates calculated in BurnMan (Cottaar et al., 2014) with mineral properties from Stixrude and Lithgow-Bertelloni (2011). The density of ol is evaluated along the geotherm of Anderson (1982) and the densities of wd, rw, and pv are evaluated along the geotherm of Brown and Shankland (1981). EOS parameters for the melt isotherms can be found in Table 2.4. **(f)** The main panel shows geotherms from Brown and Shankland (1981) and Anderson (1982), along with the solidi of dry peridotite (Zhang and Herzberg, 1994); dry pyrolite (Nomura et al., 2014); dry MORB (Andrault et al., 2014); alkali-rich peridotite + 5wt% CO_2 [ACP] (Ghosh et al., 2014); and eclogite + 2.5wt% CO_2 [CE] (Litasov and Ohtani, 2010). The inset zooms in on the interval 0-25 GPa and shows the hydrous solidi of peridotite (Kawamoto and Holloway, 1997); basalt (Lambert and Wyllie, 1972); and granite (Huang and Wyllie, 1981). Stars show second critical endpoints (SCEP) of albite [Ab] (Paillat et al., 1992); potassium feldspar [Kfs] (Mibe et al., 2008); SiO_2 (Kennedy et al., 1962); basalt (Mibe et al., 2011); and peridotite (Wang et al., 2020). The solidi of anhydrous and hydrous (1.1wt% H_2O) carbonated pelite [CPEL] are from Grassi and Schmidt (2011). Pressure-temperature curves of stagnant slabs are from Litasov and Ohtani (2010).

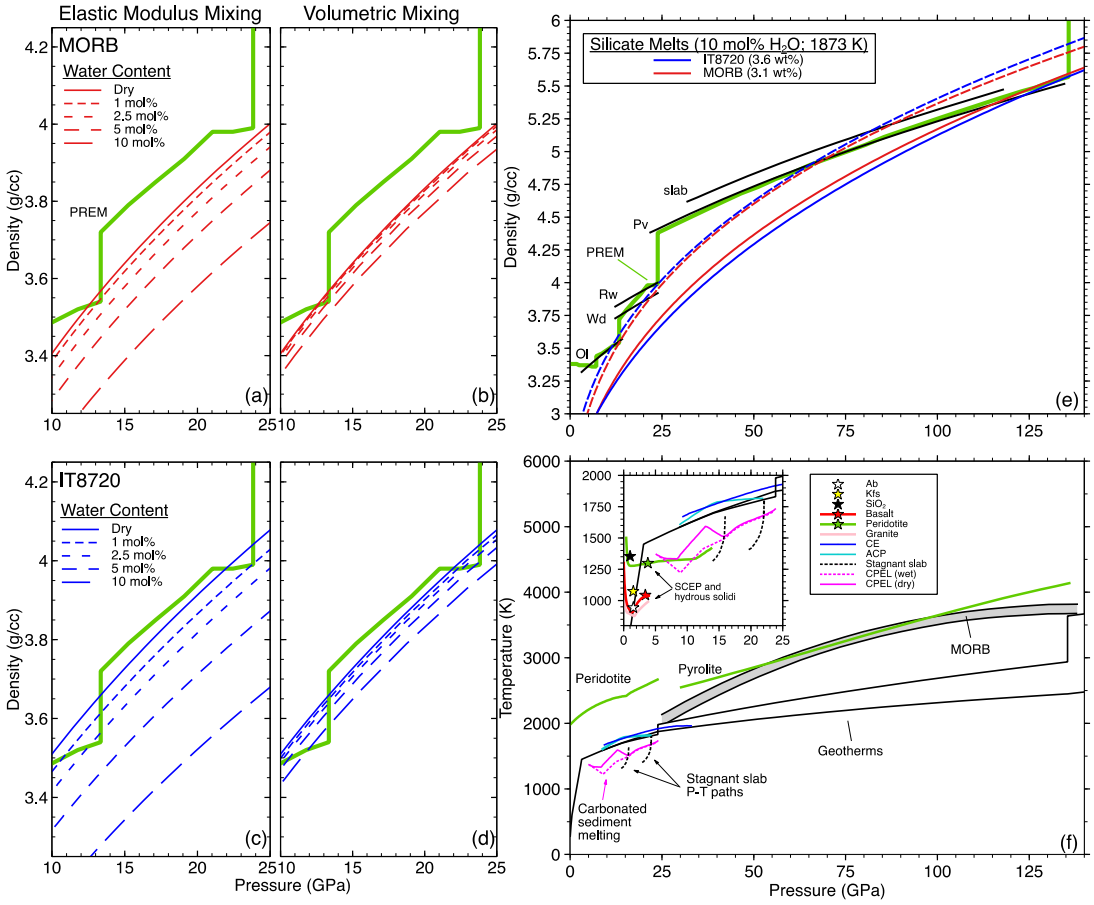
Elastic Modulus Mixing
Volumetric Mixing
MORB
Water Content
Dry
1 mol%
2.5 mol%
5 mol%
10 mol%
PREM
Density (g/cc)
(a)
(b)
IT8720
Water Content
Dry
1 mol%
2.5 mol%
5 mol%
10 mol%
Density (g/cc)
(c)
(d)
Pressure (GPa)
Silicate Melts (10 mol% H2O; 1873 K)
IT8720 (3.6 wt%)
MORB (3.1 wt%)
slab
Pv
PREM
Rw
Wd
Ol
Density (g/cc)
(e)
Ab
Kfs
SiO2
Basalt
Peridotite
Granite
CE
ACP
Stagnant slab
CPEL (wet)
CPEL (dry)
SCEP and
hydrous solidi
Peridotite
Pyrolite
MORB
Geotherms
Stagnant slab
P-T paths
Carbonated
sediment
melting
Temperature (K)
(f)
Pressure (GPa)

Figure 2.3 The effects of partial melt on seismic wave velocities. **(a-b)** P- and S-wave velocity reductions as functions of melt fraction for different partial melt geometries. Velocity reductions for partial melt films with three different aspect ratios are plotted as broken lines. Note that the vertical axes have different scales. The elastic moduli of a melt film-rock aggregate were calculated with the method of Walsh (1969). The spheres and tubes were calculated with the method of Watt et al. (1976). **(c)** Seismic velocity profiles of the mantle near the top of the MTZ from two different reference models shown in red and blue: PREM and IASP91 (Dziewonski and Anderson, 1981; Kennett and Engdahl, 1991). Velocity profiles for mantle rock with 2% partial melt distributed in films with different aspect ratios are shown as broken black lines. **(d)** V_P:V_S ratios shown for the two seismic reference models and mantle rock with melt films.

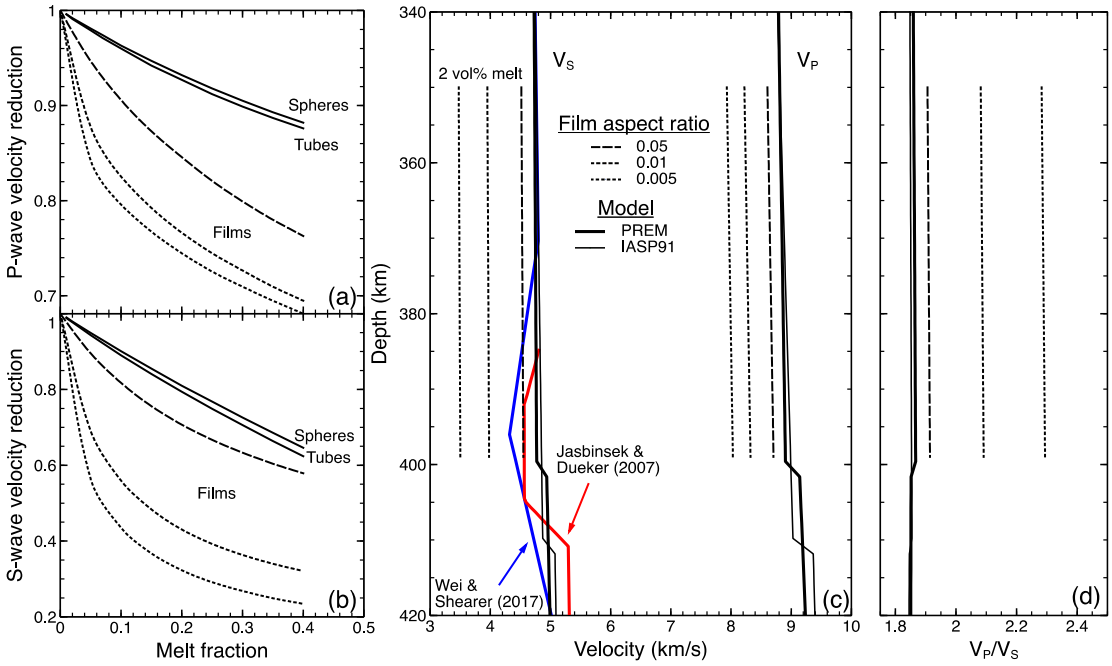
P-wave velocity reduction
S-wave velocity reduction
Melt fraction
Spheres
Tubes
Films
(a)
(b)
Depth (km)
2 vol% melt
V_S
V_P
Film aspect ratio
0.05
0.01
0.005
Model
PREM
IASP91
Jasbinsek & Dueker (2007)
Wei & Shearer (2017)
Velocity (km/s)
(c)
V_P/V_S
(d)

Figure 3.1 Structural refinements of bütschliite and bütschliite-II at 0 and 7.6 GPa, respectively, from different perspectives **(a-e)**. Atomic spacings of bütschliite and bütschliite-II derived from single-crystal measurements **(f-k)**. Note that the structures in **(c-e)** are drawn with the K^+ ions in 12-fold coordination. The unfilled square symbols in **(h)** show distances between unbonded potassium and oxygen atoms that become bonded after the phase transition.

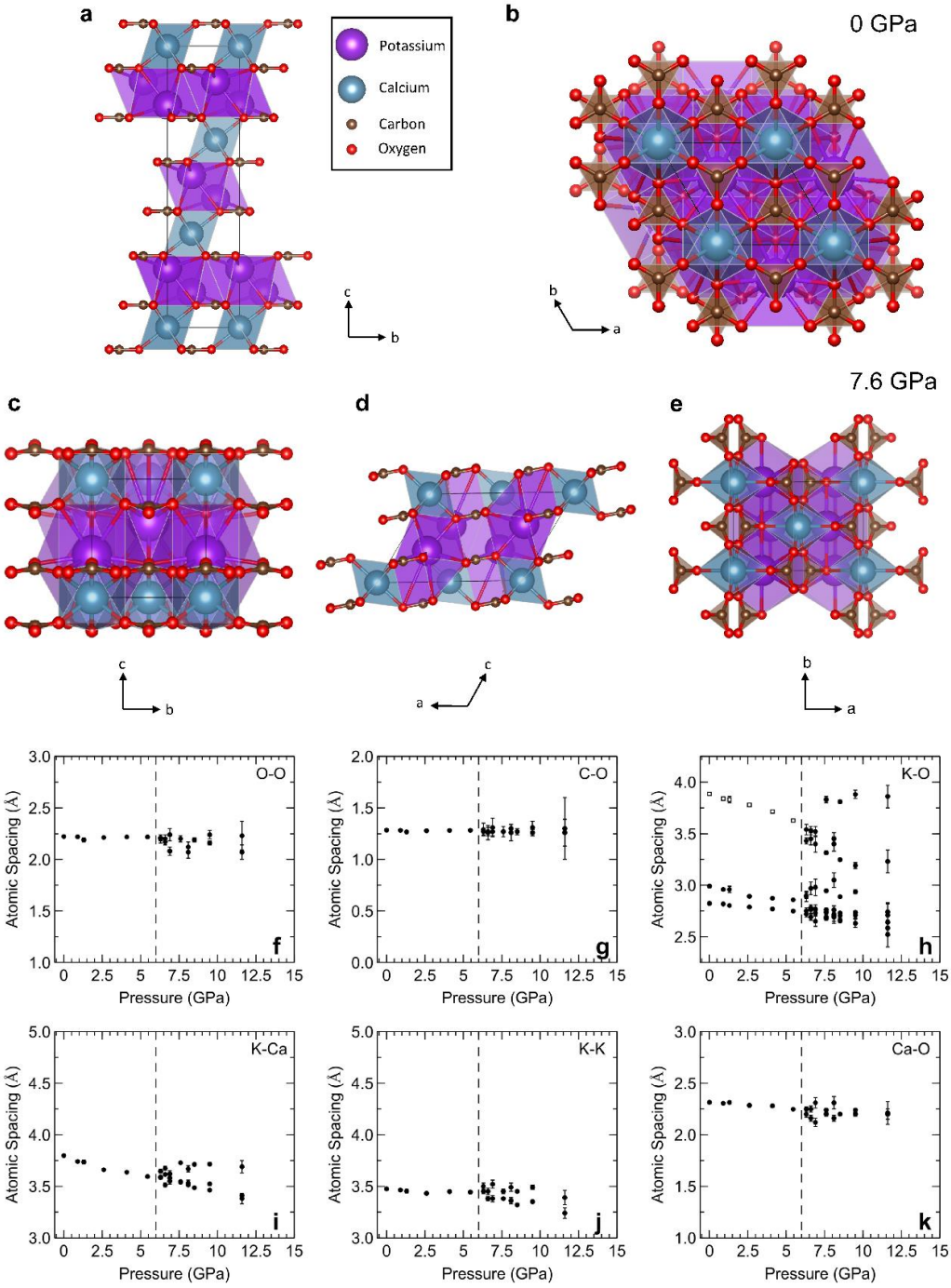
a
Potassium
Calcium
Carbon
Oxygen
c
b
b
0 GPa
b
a
7.6 GPa
c
d
e
c
b
c
a
b
a
O-O
f
C-O
g
K-O
h
K-Ca
i
K-K
j
Ca-O
k
Atomic Spacing (Å)
Pressure (GPa)

Figure 3.2 Lattice parameters **(a-c)**, β-angles **(d)**, formula unit normalized volumes **(e)**, and unit cell volumes of bütschliite and bütschliite-II during compression **(f)**. The green markers in **(c)** show the $3csin(\beta)$ trend, which is directly comparable to the c-axis in the low-pressure phase. The black star in **(f)** is the calculated zero-pressure volume of bütschliite-II from the method of Jeanloz (1981). Equation of state parameters for **(f)** are reported in the text. Fits only include the experimental x-ray data. The data point of Hou et al. (2022) at 10 GPa is in a metastable regime of the *C*2/*m* phase: they calculate that the $P\bar{1}$ structure is stable from 3.3 to 10.3 GPa. Tian et al. (2023) do not report lattice parameters or β-angles; the *C*2/*m* phase is stable in their calculations from either 3.3 or 3.5 GPa to 10.3 or 10.5 GPa (their paper is inconsistent in its reporting of the pressure of transitions). Error bars fall within the symbols.

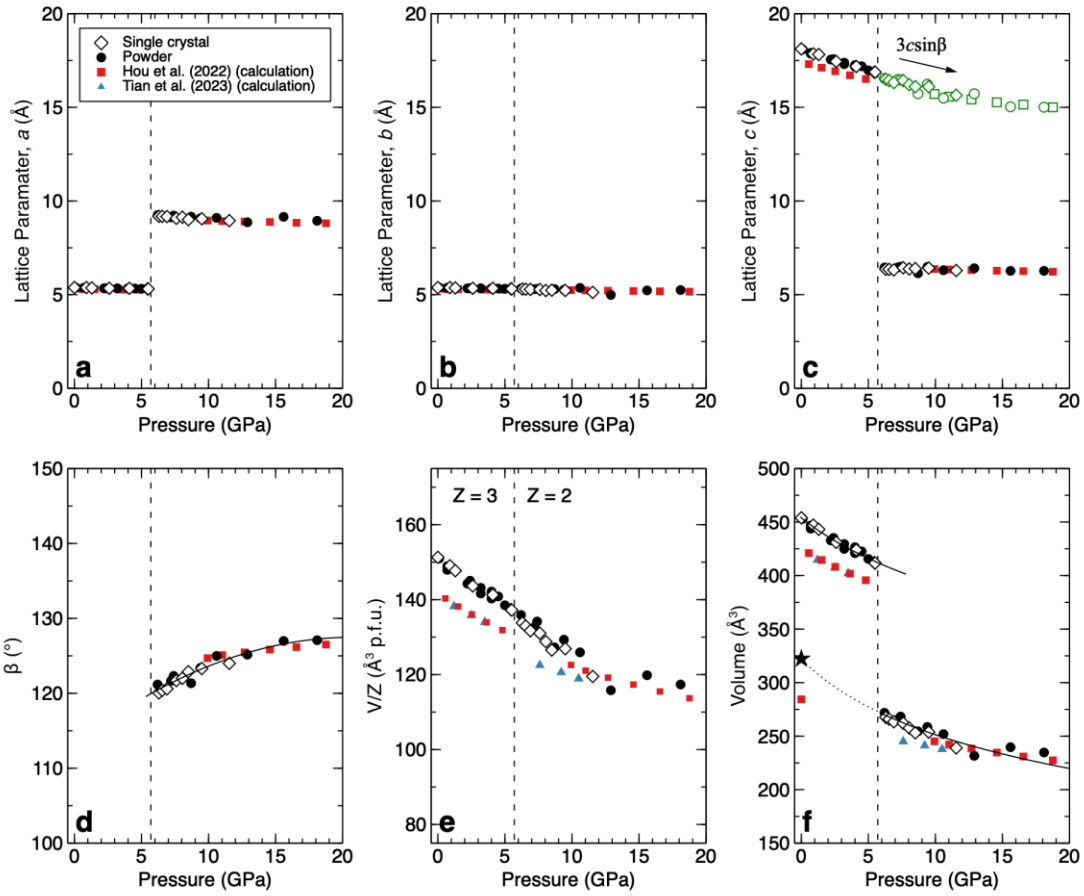
Single crystal
Powder
Hou et al. (2022) (calculation)
Tian et al. (2023) (calculation)
Lattice Paramater, a (Å)
Lattice Parameter, b (Å)
Lattice Parameter, c (Å)
3csinβ
Pressure (GPa)
a
b
c
β (°)
V/Z (Å³ p.f.u.)
Z = 3
Z = 2
Volume (Å³)
d
e
f

Figure 3.3 K-O coordination environments of the $R\bar{3}m$ **(a)** and *C*2/*m* **(b,c)** phases of bütschliite. Coordination progresses from 9-fold in **(a)**, to 12-fold (9+3) in **(b)**, to 11-fold (9+2) in **(c)**. The dotted line in **(c)** shows the oxygen atom leaving the potassium coordination sphere.

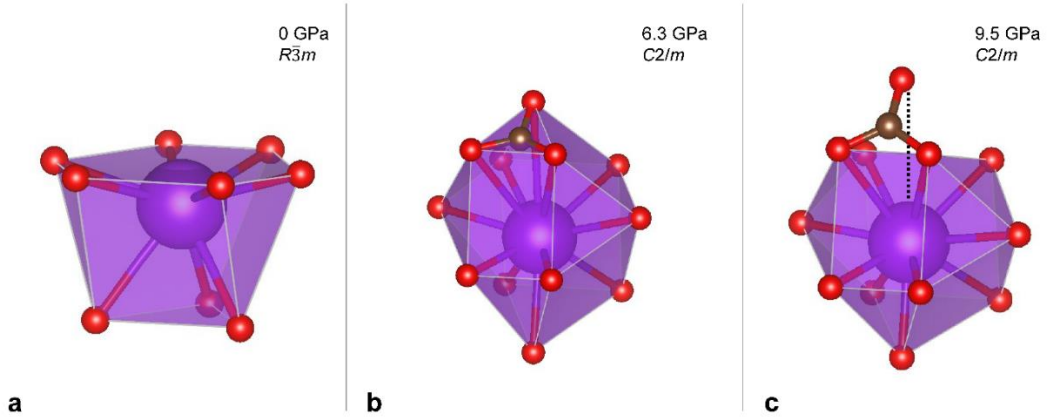
0 GPa
$R\bar{3}m$
a
6.3 GPa
C2/m
b
9.5 GPa
C2/m
c

Figure 3.4 Tilt of [CO_3] units in the bütschliite-II phase as a function of pressure, derived from single-crystal XRD refinements. The angle θ is formed by the intersection of the (001) plane with a plane passing through the three oxygen atoms in a [CO_3] unit. The fit is a quadratic fit intended to guide the eye.

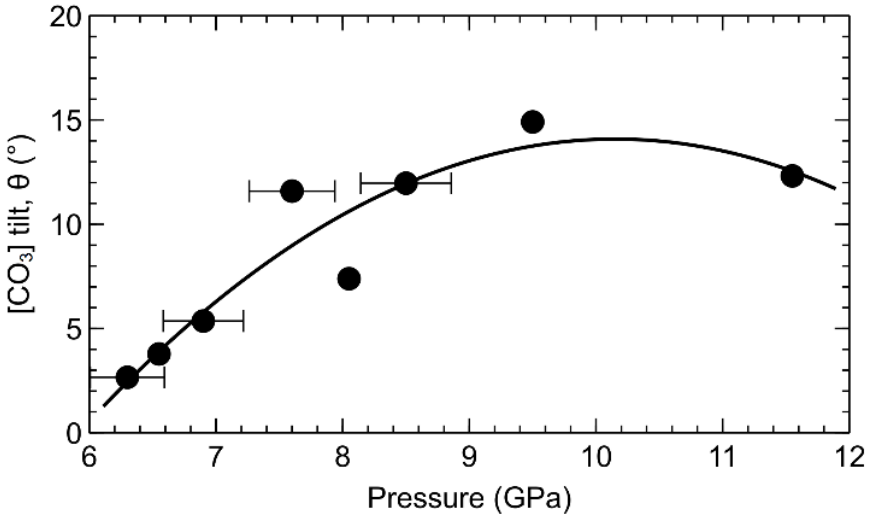
20
15
10
5
0
6
7
8
9
10
11
12
[CO3] tilt, θ (°)
Pressure (GPa)

Figure 3.5 Raman spectrum of synthetic bütschliite-I taken under ambient conditions.

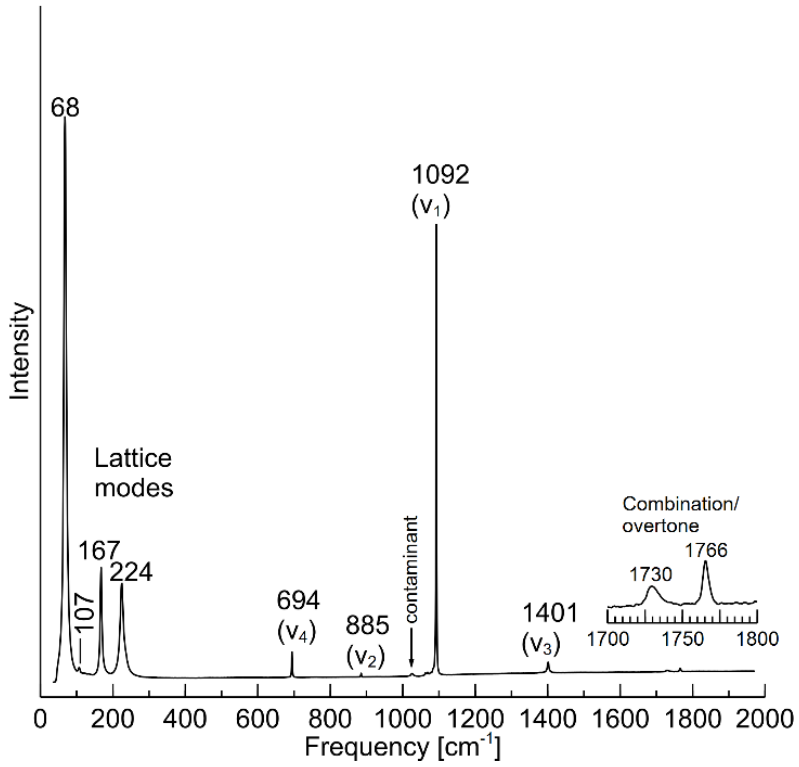
68
1092
(v1)
Intensity
Lattice
modes
167
224
107
694
(v4)
885
(v2)
contaminant
1401
(v3)
Combination/
overtone
1766
1730
1700
1750
1800
0
200
400
600
800
1000
1200
1400
1600
1800
2000
Frequency [cm-1]

Figure 3.6 Mode shifts **(a-b)** and representative spectra **(c-f)** of bütschliite on compression to 94 GPa. The first appearances of new phases are marked by lines at 6.0, 27.8, 33.5, and 37.4 GPa and the colors correspond to different phase regimes: bütschliite-I is black, bütschliite-II is green, bütschliite-III is orange, bütschliite-IV is magenta, and bütschliite-V is blue. For clarity, the largest peak intensities have been normalized to the same amplitude across panels **(c-f)**.

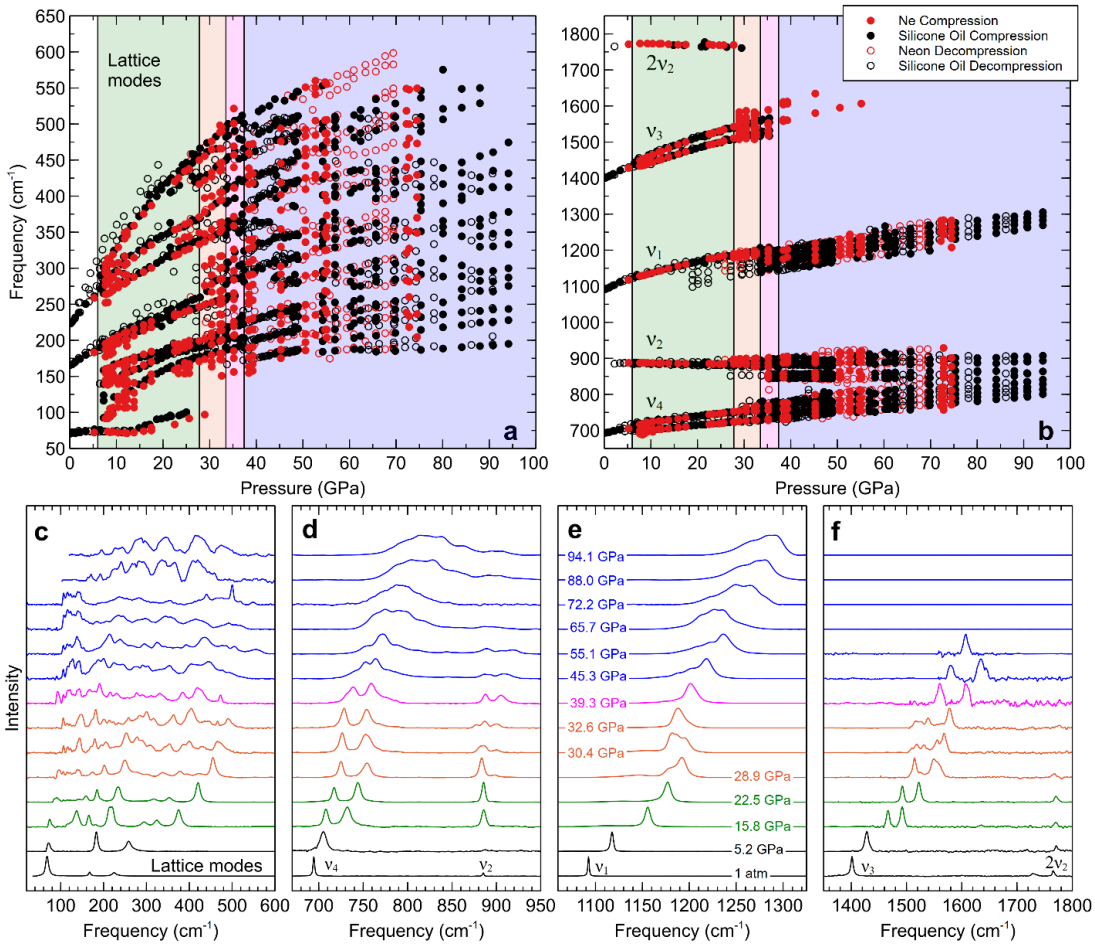
Lattice modes
Frequency (cm-1)
Pressure (GPa)
a
b
Ne Compression
Silicone Oil Compression
Neon Decompression
Silicone Oil Decompression
2ν2
ν3
ν1
ν2
ν4
c
d
e
f
Intensity
94.1 GPa
88.0 GPa
72.2 GPa
65.7 GPa
55.1 GPa
45.3 GPa
39.3 GPa
32.6 GPa
30.4 GPa
28.9 GPa
22.5 GPa
15.8 GPa
5.2 GPa
1 atm
Lattice modes
ν4
ν2
ν1
ν3
2ν2
Frequency (cm-1)

Figure 3.7 Mode shifts of bütschliite-I under compression up to the transition to the *C*2/*m* phase.

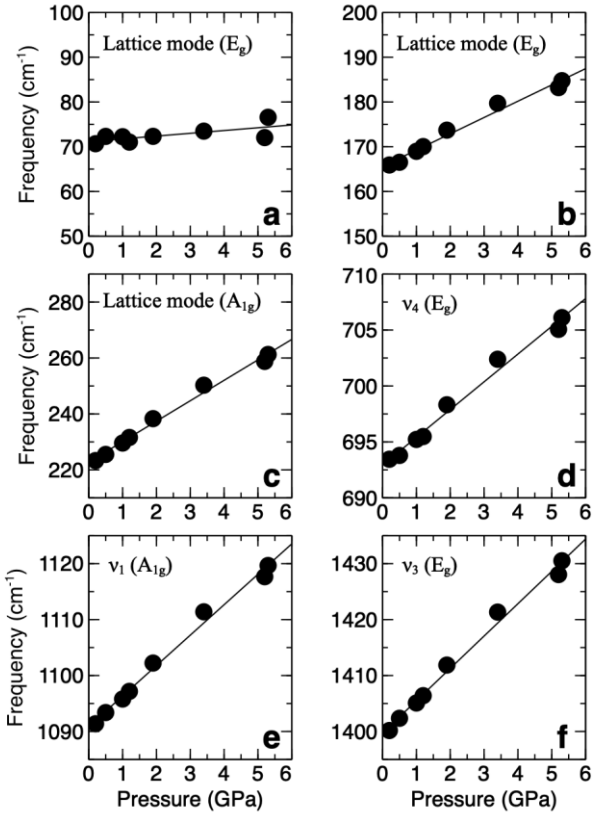
Lattice mode (E_g)
Lattice mode (E_g)
Lattice mode (A_{1g})
ν_4 (E_g)
ν_1 (A_{1g})
ν_3 (E_g)
Frequency (cm^{-1})
Pressure (GPa)
a
b
c
d
e
f

Figure 3.8 Raman spectra showing the transition from bütschliite-I (black) to bütschliite-II (green). For clarity, the largest peak intensities have been normalized to the same amplitude across the panels.

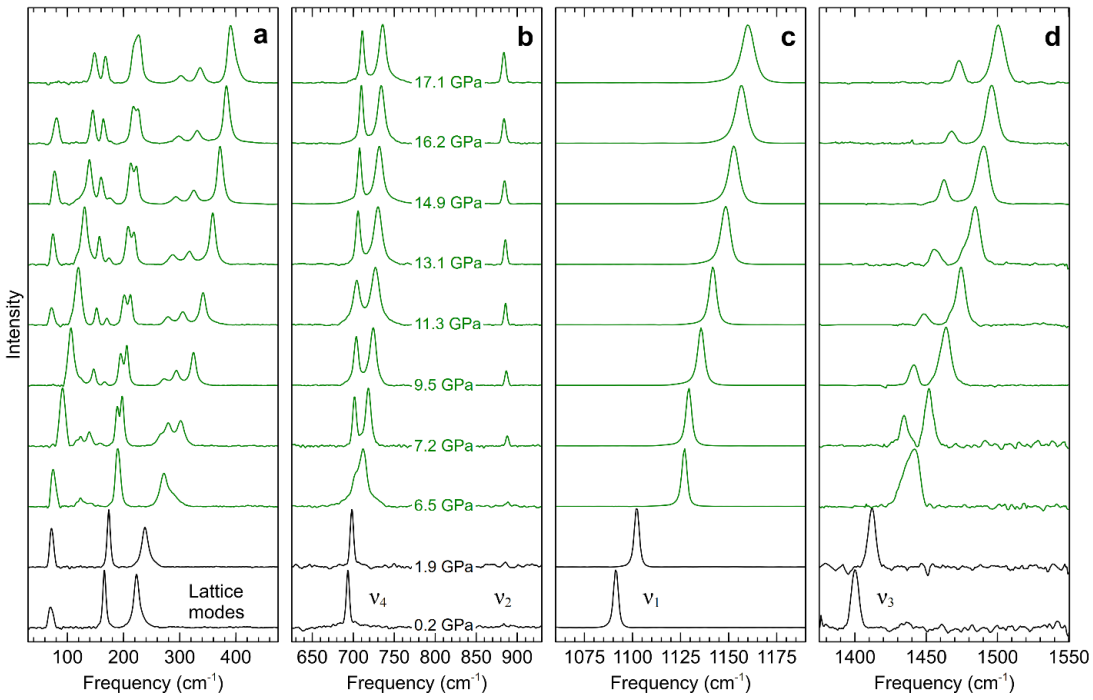
a
b
c
d
Intensity
17.1 GPa
16.2 GPa
14.9 GPa
13.1 GPa
11.3 GPa
9.5 GPa
7.2 GPa
6.5 GPa
1.9 GPa
0.2 GPa
Lattice modes
ν4
ν2
ν1
ν3
100 200 300 400
650 700 750 800 850 900
1075 1100 1125 1150 1175
1400 1450 1500 1550
Frequency (cm-1)
Frequency (cm-1)
Frequency (cm-1)
Frequency (cm-1)

Figure 3.9 Fermi Resonance in bütschliite-II. Raman spectra of the lattice modes during compression **(a)**. Resonating peaks are marked with asterisks. Measured frequencies of resonating peaks and calculated unperturbed frequencies **(b)**. Normalized intensities of the resonating peaks **(c)**.

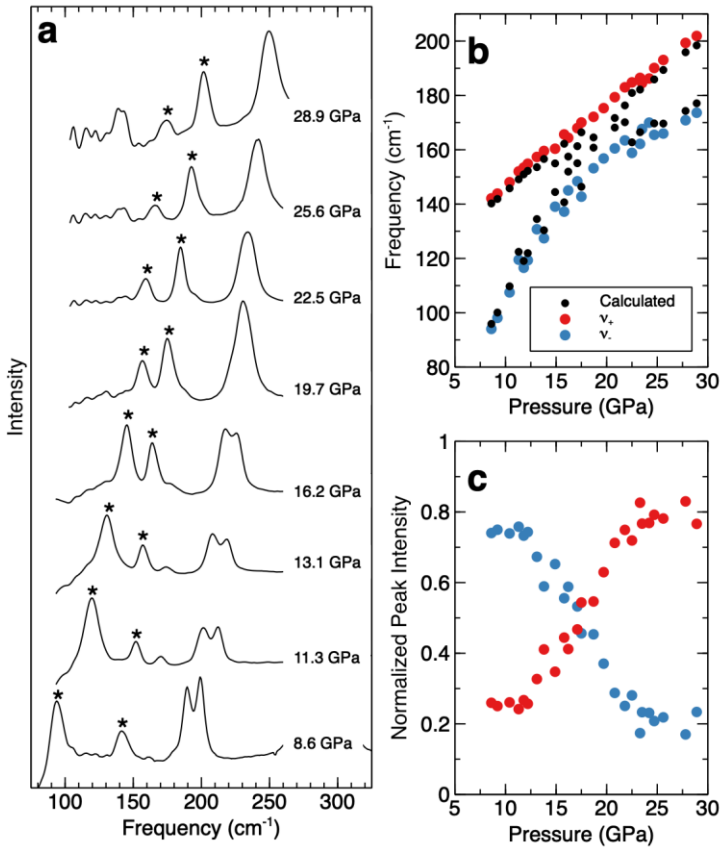
a
28.9 GPa
25.6 GPa
22.5 GPa
19.7 GPa
16.2 GPa
13.1 GPa
11.3 GPa
8.6 GPa
Intensity
100
150
200
250
300
Frequency (cm-1)
b
Frequency (cm-1)
Calculated
ν+
ν-
Pressure (GPa)
c
Normalized Peak Intensity
Pressure (GPa)

Figure 3.4 Carbonate mode shifts of bütschliite-II. Blue and red diamonds show extrapolations to zero pressure.

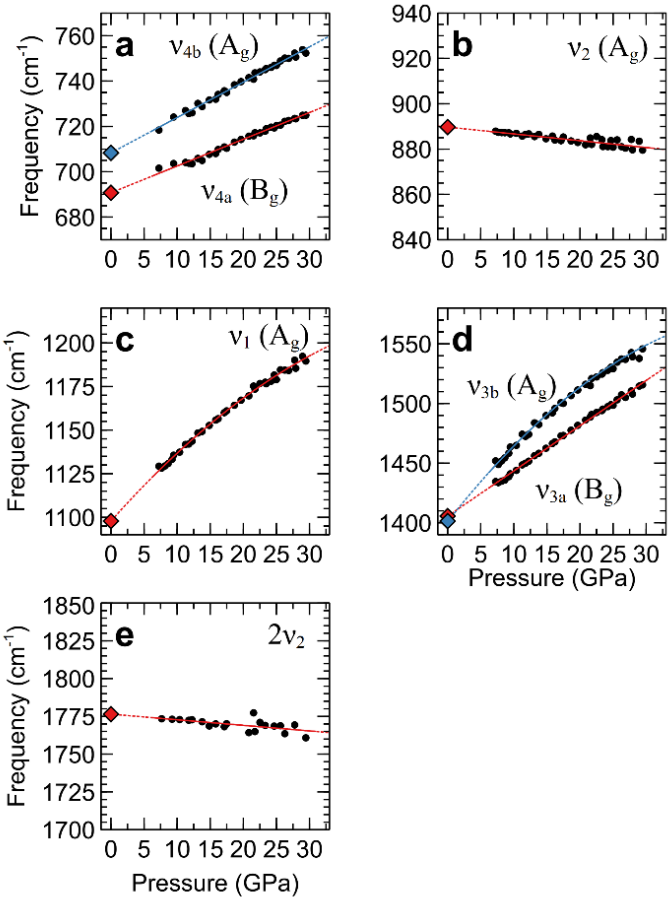
a
ν_{4b} (A_g)
ν_{4a} (B_g)
b
ν_2 (A_g)
c
ν_1 (A_g)
d
ν_{3b} (A_g)
ν_{3a} (B_g)
e
$2\nu_2$
Frequency (cm^{-1})
Pressure (GPa)

Figure 3.5 Raman spectra showing phase transitions from bütschliite-II through bütschliite-V. For clarity, the largest peak intensities have been normalized to the same amplitude across the panels. Unlabeled spectra were measured with the sample in a Ne PTM. Bütschliite-II is shown in green, bütschliite-III in orange, bütschliite-IV in magenta, and bütschliite-V in blue.

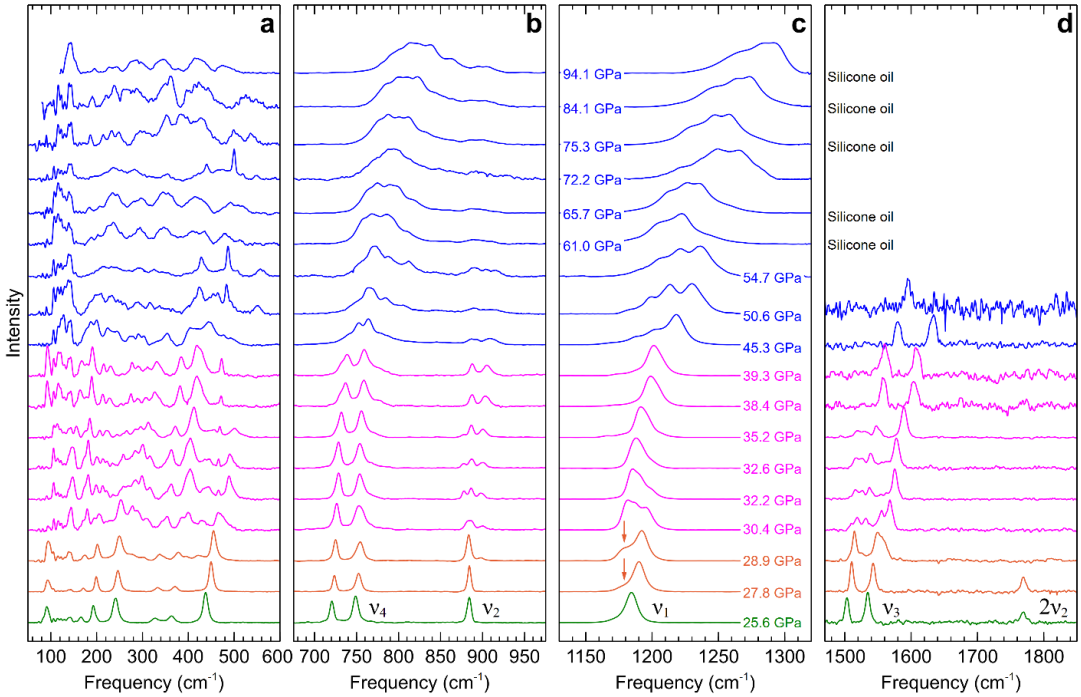
a
b
c
d
Intensity
94.1 GPa
84.1 GPa
75.3 GPa
72.2 GPa
65.7 GPa
61.0 GPa
54.7 GPa
50.6 GPa
45.3 GPa
39.3 GPa
38.4 GPa
35.2 GPa
32.6 GPa
32.2 GPa
30.4 GPa
28.9 GPa
27.8 GPa
25.6 GPa
Silicone oil
Silicone oil
Silicone oil
Silicone oil
Silicone oil
ν4
ν2
ν1
ν3
2ν2
100 200 300 400 500 600
700 750 800 850 900 950
1150 1200 1250 1300
1500 1600 1700 1800
Frequency (cm-1)
Frequency (cm-1)
Frequency (cm-1)
Frequency (cm-1)

Figure 3.6 Isothermal bulk moduli as a function of cation radius for a suite of structurally and compositionally diverse carbonate minerals. The solid black line is a fit to the double carbonates only and the dotted gray line is a fit to all data. Cation radii are taken from Shannon (1976). Bulk moduli data are from: bütschliite and bütschliite-II ($K_2Ca(CO_3)_2$, this study); spherocobaltite ($CoCO_3$, Chariton et al., 2017); eitelite ($Na_2Mg(CO_3)_2$) and $K_2Mg(CO_3)_2$ (Golubkova et al., 2015); siderite ($FeCO_3$, Lavina et al., 2010); rhodochrosite ($MnCO_3$, Merlini et al., 2015); aragonite ($CaCO_3$, Palaich et al., 2016); calcite ($CaCO_3$, Redfern and Angel, 1999); dolomite and ankerite ($CaMg(CO_3)_2$ and $Ca(Fe,Mg,Mn)(CO_3)_2$, Ross and Reeder, 1992); gaspéite ($(Ni,Mg)CO_3$, Sawchuk et al., 2021); shortite ($Na_2Ca_2(CO_3)_3$, Vennari et al., 2018); strontianite and witherite ($SrCO_3$ and $BaCO_3$, Wang et al., 2015); cerussite ($PbCO_3$, Yu-Feng et al., 2013); and magnesite ($MgCO_3$, Zhang et al., 1997).

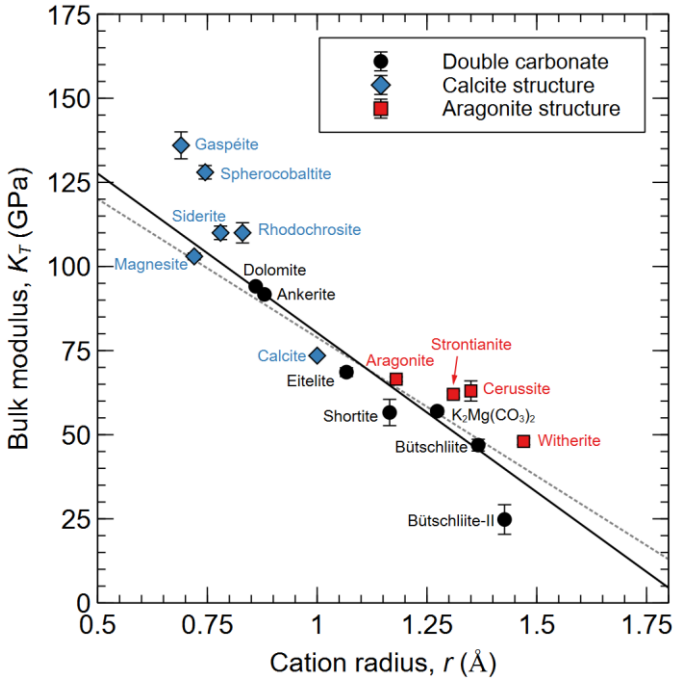
Double carbonate
Calcite structure
Aragonite structure
Gaspéite
Spherocobaltite
Siderite
Rhodochrosite
Magnesite
Dolomite
Ankerite
Calcite
Aragonite
Strontianite
Eitelite
Cerussite
Shortite
$K_2Mg(CO_3)_2$
Witherite
Bütschliite
Bütschliite-II
Bulk modulus, K_T (GPa)
Cation radius, r (Å)
175
150
125
100
75
50
25
0
0.5
0.75
1
1.25
1.5
1.75

Figure 4.7 Ambient Raman spectra of natural shortite **(a)** and synthetic bütschliite **(b)**. Peak locations and assignments are reported in Table 4.1 and Table 4.2.

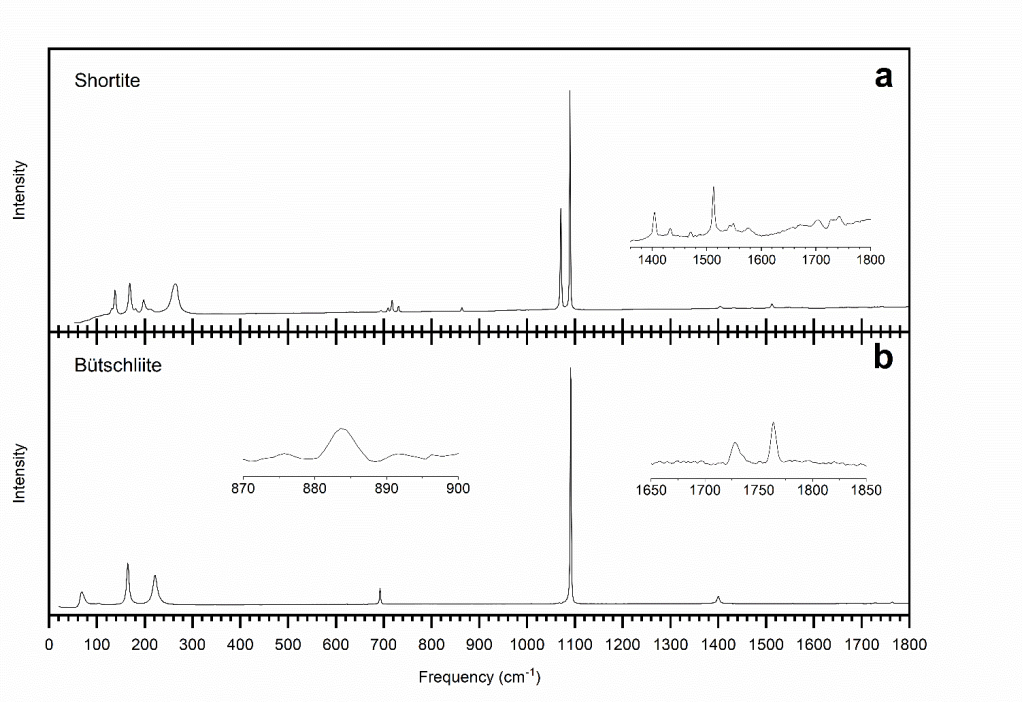
Shortite
a
Intensity
1400
1500
1600
1700
1800
Bütschliite
b
Intensity
870
880
890
900
1650
1700
1750
1800
1850
0
100
200
300
400
500
600
700
800
900
1000
1100
1200
1300
1400
1500
1600
1700
1800
Frequency (cm-1)

Figure 4.2 High-temperature Raman mode shifts of bütschliite. High-temperature phases are plotted as triangles.

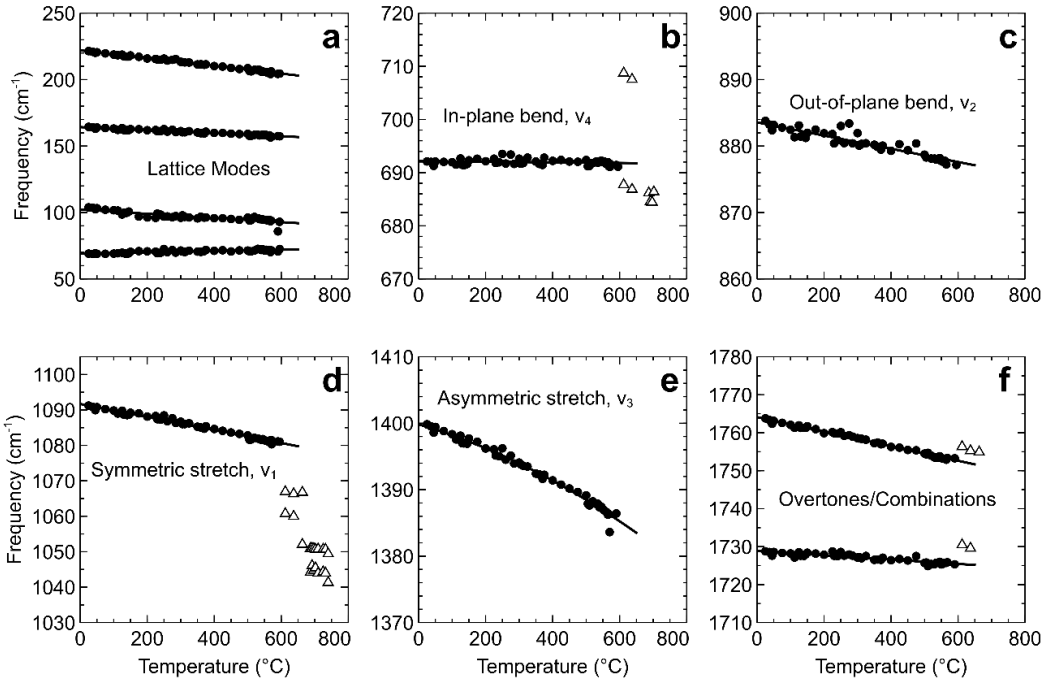
a
Lattice Modes
b
In-plane bend, v_4
c
Out-of-plane bend, v_2
d
Symmetric stretch, v_1
e
Asymmetric stretch, v_3
f
Overtones/Combinations
Frequency (cm^{-1})
Temperature (°C)

Figure 4.3 Arrangements of the trigonal planar [CO_3] units in aragonite, bütschliite, and dolomite. Each unit cell is viewed down the *b*-axis. Metal cations are hidden for clarity. Dotted lines emphasize the alignments of nearest neighbor carbon atoms.

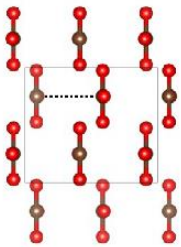

Aragonite

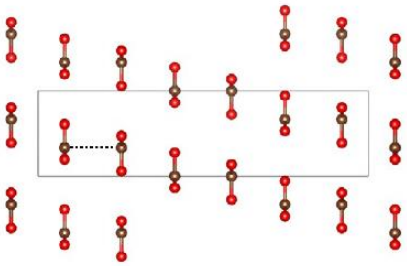

Bütschliite

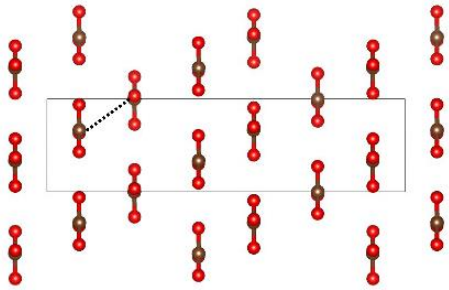

Dolomite

Figure 4.4 Linewidths of the internal carbonate modes of bütschliite.

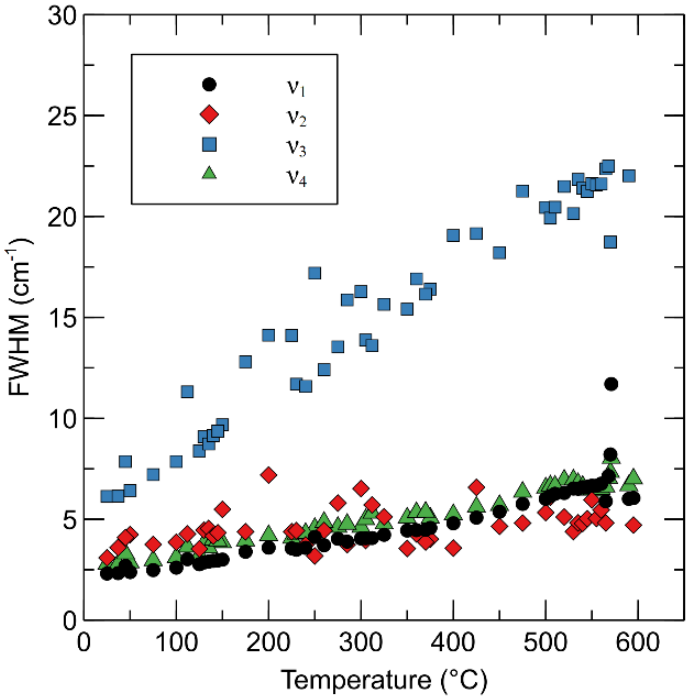
30
25
20
15
10
5
0
0
100
200
300
400
500
600
FWHM (cm-1)
Temperature (°C)
ν1
ν2
ν3
ν4

Figure 4.5 High-temperature Raman spectra of bütschliite. The spectra between 571 and 595°C are representative spectra taken in different locations within the sample, and show the spatially heterogeneous nature of the transition.

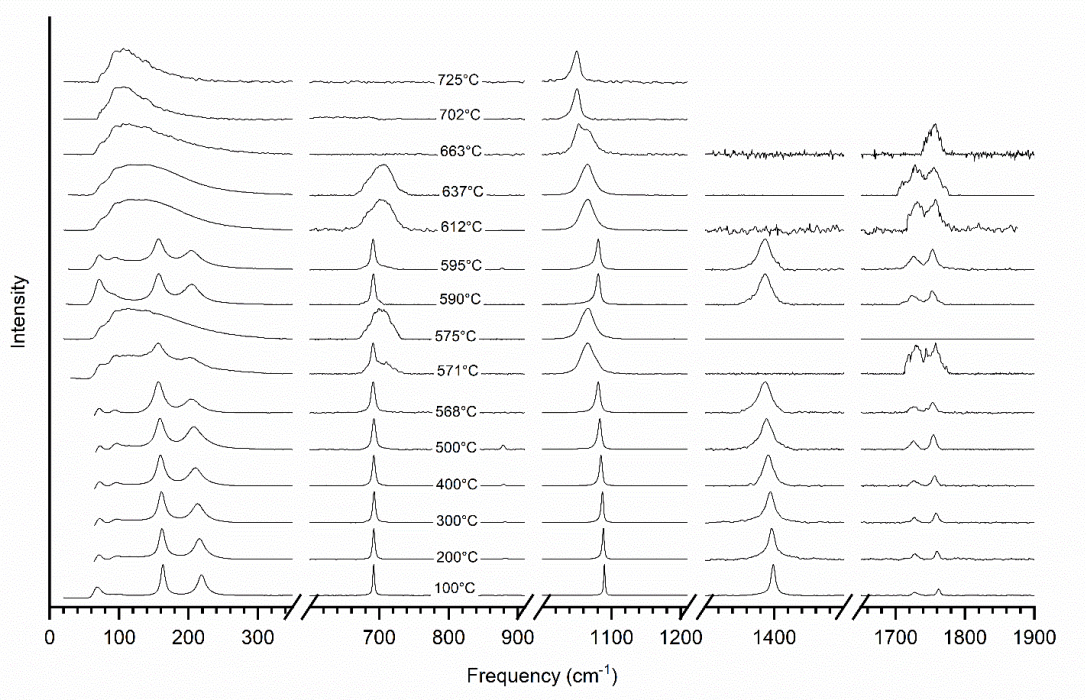
Intensity
725°C
702°C
663°C
637°C
612°C
595°C
590°C
575°C
571°C
568°C
500°C
400°C
300°C
200°C
100°C
0
100
200
300
700
800
900
1100
1200
1400
1700
1800
1900
Frequency (cm-1)

Figure 4.6 Spectrum of fairchildite at 637°C **(a)**. Deconvolution of the fairchildite spectrum **(b-e)**. The raw spectrum is shown as a black dotted line, the deconvolved peaks are shown in green, and the fit spectrum is shown in blue.

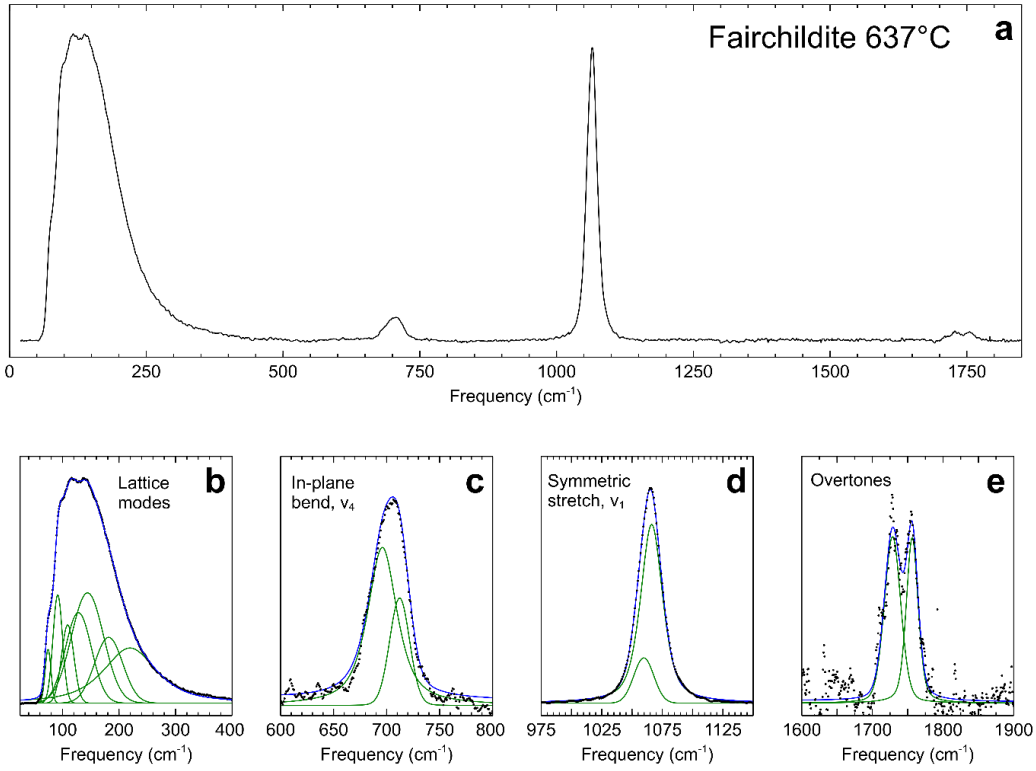
Fairchildite 637°C
a
0
250
500
750
1000
1250
1500
1750
Frequency (cm-1)
Lattice modes
b
100
200
300
400
Frequency (cm-1)
In-plane bend, v4
c
600
650
700
750
800
Frequency (cm-1)
Symmetric stretch, v1
d
975
1025
1075
1125
Frequency (cm-1)
Overtones
e
1600
1700
1800
1900
Frequency (cm-1)

Figure 4.7 Raman mode shifts of shortite. The modes of the high-temperature phase are shown with triangles.

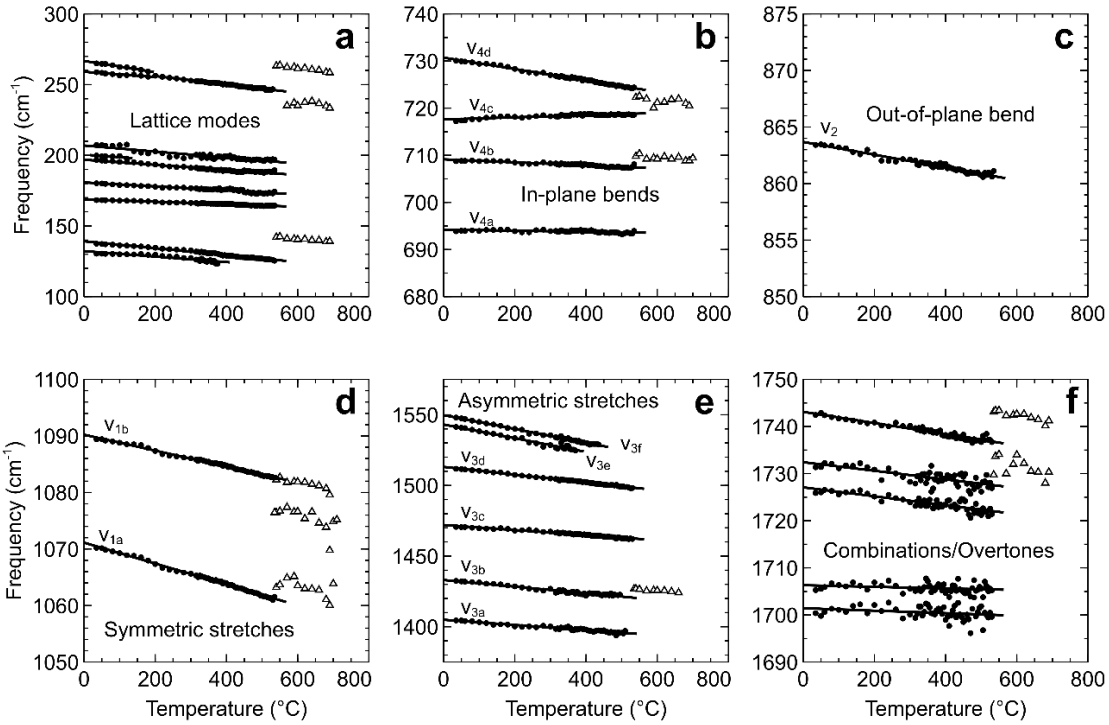
a
Lattice modes
b
ν_{4d}
ν_{4c}
ν_{4b}
In-plane bends
ν_{4a}
c
Out-of-plane bend
ν_2
d
ν_{1b}
ν_{1a}
Symmetric stretches
e
Asymmetric stretches
ν_{3f}
ν_{3e}
ν_{3d}
ν_{3c}
ν_{3b}
ν_{3a}
f
Combinations/Overtones
Frequency (cm^{-1})
Temperature (°C)

Figure 4.8 High-temperature Raman spectra of shortite. The 715°C spectrum was collected with a 633 nm excitation laser.

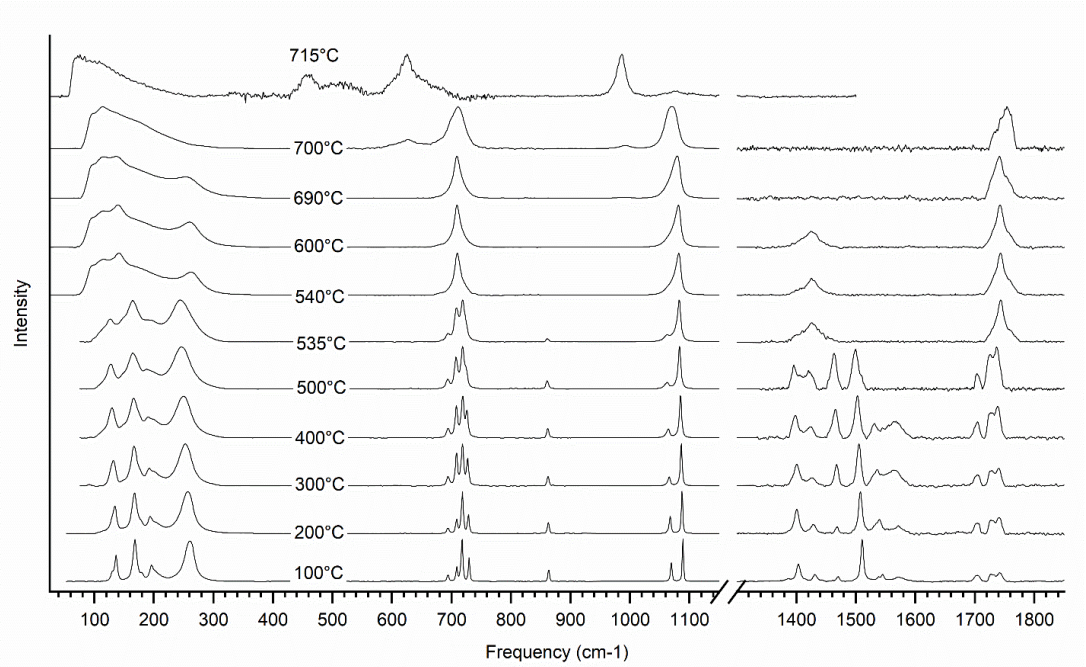
715°C
700°C
690°C
600°C
540°C
535°C
500°C
400°C
300°C
200°C
100°C
Intensity
100
200
300
400
500
600
700
800
900
1000
1100
1400
1500
1600
1700
1800
Frequency (cm-1)

Figure 4.9 Scaled mode Gruneisen parameters of bütschliite and shortite. The error bars on the lowest frequency lattice mode of bütschliite correspond to the range reported in Table 4.1. The dotted line corresponds to ideal harmonic behavior.

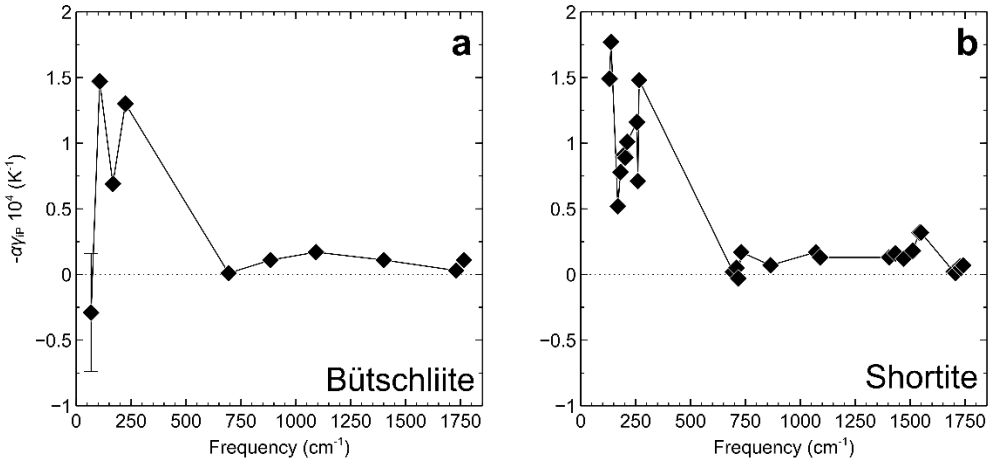
a
b
Bütschliite
Shortite
$-\alpha\gamma_{HF}\ 10^4\ (K^{-1})$
Frequency (cm^{-1})
2
1.5
1
0.5
0
−0.5
−1
0
250
500
750
1000
1250
1500
1750

Tables

Table 1.1 Bulk mantle and liquid compositions (generated in pMELTS). The bulk mantle composition is taken from Elkins-Tanton et al. (2003), modified after Bertka & Fei (1997), with total iron reported as FeO. The first two letters in each composition name represent an initially anhydrous (AM) or hydrous mantle (HM), and the numbers correspond to wt% melt.

	Bulk Mantle	HM55	AM40	AM30	AM20
Wt % liquid	--	55.05	40.08	30.10	19.18
Density (g/cc)	--	3.26	3.43	3.50	3.53
SiO_2	43.90	36.89	35.67	35.20	35.43
Al_2O_3	3.15	5.03	4.57	3.76	2.50
Fe_2O_3	--	2.33	2.65	2.93	3.07
FeO	18.80	25.06	30.26	33.87	35.56
MgO	31.66	25.76	22.14	18.52	17.42
CaO	2.50	3.84	4.71	5.71	6.01
H_2O	--	0.90	0.00	0.00	0.00
CO_2	--	0.18	0.00	0.00	0.00

Table 1.2 Normative mineralogy calculations: two different TCBL assemblages for each liquid composition.

			Mole Fraction Solid Phases			
	Solid Phase	Composition	HM55	AM40	AM30	AM20
Assemblage 1	Ca-perovskite	$CaSiO_3$	0.08	0.09	0.10	0.10
	Garnet	$(Mg_{0.8}Fe_{0.2})_3Al_2Si_3O_{12}$	0.06	0.05	0.04	0.02
	Ringwoodite	$(Mg_{0.75}Fe_{0.25})_2SiO_4$	0.60	0.47	0.37	0.35
	Ferropericlase	FeO	0.20	0.30	0.36	0.37
	Stishovite	SiO_2	0.06	0.09	0.13	0.15
Assemblage 2	Ca-perovskite	$CaSiO_3$	0.07	0.09	0.10	0.10
	Garnet	$(Mg_{0.8}Fe_{0.2})_3Al_2Si_3O_{12}$	0.05	0.05	0.03	0.02
		$(Mg_{0.6}Fe_{0.4})SiO_3$	0.42	0.54	0.49	0.47
	Ferropericlase	$(Mg_{0.85}Fe_{0.15})O$	0.20	0.13	0.08	0.10
		FeO	0.26	0.20	0.29	0.31

Table 2.1 Summary of experiments and simulations considered in this study. Water concentrations, pressures, and temperatures represent maximum values from each study.

Technique	Reference	Composition	H_2O (wt%)	P (GPa)	T (K)
Bellows compression	Burnham & Davis (1971)	$NaAlSi_3O_8$	11	1	1220
Brillouin	Tkachev et al. (2005)	Na_2O-$2SiO_2$	46	8	850
FPMD	Bajgain et al. (2015)	Basalt	8	100	4000
	Bajgain et al. (2019)	$NaAlSi_2O_6$	4	30	4000
	Du et al. (2019)	Fe-rich ultramafic	12	150	4000
	Karki et al. (2021)	$(Mg,Fe)SiO_3$/$(Mg,Fe)_2SiO_4$	11	140	4000
	Mookherjee et al. (2008)	$MgSiO_3$	10	110	6000
	Solomotova & Caracas (2021)	Pyrolite	5	140	5000
	Yuan et al. (2020)	Mg_2SiO_4	27	16	2200
Low pressure (1 bar)	Bouhifd et al. (2015)	Various (alkali rich)	Various	0	1270
	Ochs & Lange (1997)	$NaAlSi_3O_8$	6	0	1670
	Ochs & Lange (1999)	Rhyolite	6	0	1270
Shock compression	Tyburczy et al. (1991)	$Mg_3Si_2O_5(OH)_4$	13	175	6000
Sink/float	Agee (2008)	Fe-rich ultramafic	5	8	2070
	Jing & Karato (2012)	Fe-rich ultramafic	7	14	2170
	Matsukage et al. (2005)	Fe-rich ultramafic	5	14	2170
	Sakamaki et al. (2006)	Basalt	8	20	2470
X-ray absorption	Malfait et al. (2014a)	Rhyolite	8	4	1950
	Malfait et al. (2014b)	Andesite	9	4	1800
	Sakamaki et al. (2009)	Peridotite	5	4	2070
	Seifert et al. (2013)	Phonolite	4	3	1850

Table 2.2 Equation of state fits for each bin in Figure 2.2. †Estimated from Figure 16 of Tkachev et al. (2005). *Our preferred fit parameters (principally derived from the 1873 K fits). V_0 was calculated assuming V_{1673K} = 27.75 cm^3/mol (O&L97) and dV/dT = 11.4 × 10^{-3} cm^3/K (see Table 2.3); one standard deviation uncertainties for the fit parameters are given in parentheses.

T (K)	457	1440	1873	2150	3000	4000	5000	6000
V_0 (cm^3/mol)	13.60	25.06	30.03	33.16	42.85	54.25	65.65	77.05
				Vinet				
$K_{0,T}$ (GPa)	4.03[†]	2.32(1.21)	1.79(0.22)	0.85(0.08)	0.12(0.01)	0.06(0.01)	0.16(0.02)	0.04(0.01)
$K'_{0,T}$	--	3.45(2.67)	3.07(0.32)	5.33(0.20)	8.12(0.09)	8.26(0.12)	6.52(0.14)	7.94(0.31)
				Birch-Murnaghan				
$K_{0,T}$ (GPa)	--	1.74(1.31)	2.15(0.40)*	0.51(0.08)	0.16(0.03)	0.20(0.04)	0.26(0.03)	0.23(0.05)
$K'_{0,T}$	--	4.42(3.48)	2.11(0.23)*	4.83(0.31)	6.78(0.71)	4.91(0.26)	4.26(0.10)	4.09(0.11)
$K''_{0,T}$ (GPa^{-1})	--	--	-1.80(0.47)*	--	--	--	--	--
α_0 (10^{-4} K^{-1})	3.80							
q	-0.5							

Table 2.3 Ambient pressure thermal expansivity of the dissolved H_2O component in silicate melt.

T (K)	dV/dT (10^{-3} cm^3/K)	Composition	Reference
1273	3.4	Rhyolite	Malfait et al. (2014a)
	9.5	Rhyolite	Ochs and Lange (1999)
	5.2	Andesite	Malfait et al. (2014b)
	15.9	Various	Bouhifd et al. (2015)
1673	2.8	Phonolite	Seifert et al. (2013)
--	11.4	--	Fit to ambient pressure data

Table 2.4 Birch-Murnaghan equation of state fit parameters for the hydrous melt isotherms in Figure 2.4. Melts contain 10 mol% H_2O, indicated in wt% in parentheses.

T = 1873 K	IT8720 (3.6 wt%)	MORB (3.1 wt%)
ρ_0 (g/cc)	2.53	2.37
	Mixed parameters: Volume	
$K_{0,T}$ (GPa)	10.3	9.5
$K'_{0,T}$	8.3	6.2
$K''_{0,T}$ (GPa^{-1})	-2.80	-1.00
	Mixed parameters: $K_{0,T}$ and $K'_{0,T}$	
$K_{0,T}$ (GPa)	29.0	16.5
$K'_{0,T}$	4.4	5.2

Table 3.3 Symmetry assignments, measured initial frequencies, frequency-pressure derivatives, and mode-Grüneisen parameters of bütschliite-I.

Assignment	**Symmetry**	**Measured initial frequency, ν_0 (cm^{-1})**	**$d\nu_i/dP$ (cm^{-1}/GPa)**	γ_i
Lattice mode	E_g	68	0.62(26)	0.43
Lattice mode	E_g	107	--	--
Lattice mode	E_g	167	3.64(19)	1.03
Lattice mode	A_{1g}	224	7.31(28)	1.54
In-plane bend, ν_4	E_g	694	2.48(11)	0.17
Out-of-plane bend, ν_2	A_{1g}	885	--	--
Symmetric stretch, ν_1	A_{1g}	1092	5.44(20)	0.24
Asymmetric stretch, ν_3	E_g	1401	5.78(23)	0.19
Overtone, $2\nu_2$ (IR)	--	1730	--	--
Overtone, $2\nu_2$ (Raman)	--	1766	--	--

Table 3.4 Symmetry assignments, fit zero pressure frequencies, measured initial high-pressure frequencies, frequency-pressure derivatives, and mode-Grüneisen parameters (γ_i) of bütschliite-II evaluated at 7.3 GPa. †Evaluated at 7.6 GPa (no peak observed at 7.3 GPa).

Assignment	**Symmetry**	**Fit initial frequency, ν_0 (cm^{-1})**	**High pressure frequency, ν_P (cm^{-1})**	**$d\nu_i/dP$ (cm^{-1}/GPa)**	γ_i
In-plane bend, ν_{4a}	B_g	690.7(5)	702	1.18(3)	0.11
In-plane bend, ν_{4b}	A_g	708.3(6)	718	1.56(3)	0.14
Out-of-plane bend, ν_2	A_g	889.7(6)	888	-0.30(3)	-0.02
Symmetric stretch, ν_1	A_g	1097.8(18)	1129	4.26 – 0.07P	0.22
Asymmetric stretch, ν_{3a}	B_g	1405.6(7)	1435	3.79(4)	0.17
Asymmetric stretch, ν_{3b}	A_g	1401.0(27)	1452	7.03 – 0.14P	0.27
Overtone, $2\nu_2$[†]	--	1776.5(22)	1773	-0.37(11)	-0.01

Table 4.1 Peak assignments and temperature dependence of Raman modes of bütschliite.

Initial frequency, ν_0 [cm^{-1}]	Vibration	Symmetry	$(\partial\nu/\partial T)_P$ [cm^{-1}/K]	$-\alpha\gamma_{iP}$ [10^4 K^{-1}]
68	Lattice mode	E_g	-0.001 - 0.005	-0.29
107	Lattice mode	E_g	-0.0157(0)	1.47
167	Lattice mode	E_g	-0.0115(0)	0.69
224	Lattice mode	A_{1g}	-0.0291(0)	1.30
694	In-plane bend, ν_4	E_g	-0.0005(0)	0.01
885	Out-of-plane bend, ν_2	A_{1g}	-0.0099(0)	0.11
1092	Symmetric stretch, ν_1	A_{1g}	-0.0184(0)	0.17
1401	Asymmetric stretch, ν_3	E_g	-0.0148(2) - 3.18(0) 10^{-5} T	0.11
1730	Overtone, $2\nu_2$ (IR)	--	-0.0057(0)	0.03
1766	Overtone, $2\nu_2$ (Raman)	--	-0.0192(0)	0.11

Table 4.2 Peak assignments, fit range, and temperature dependence of the Raman modes of shortite.

Initial frequency, ν_0 [cm^{-1}]	Vibration	Symmetry	Fit range [°C]	$(\partial\nu/\partial T)_P$ [cm^{-1}/K]	$-\alpha\gamma_{iP}$ [10^4 K^{-1}]
131	Lattice mode	B_2	$T \leq 375$	-0.0195(1)	1.49
138	Lattice mode	A_1	$T \leq 530$	-0.0244(0)	1.77
169	Lattice mode	A_2	$T \leq 530$	-0.0088(0)	0.52
181	Lattice mode	A_1	$T \leq 530$	-0.0141(0)	0.78
198	Lattice mode	--	$T \leq 530$	-0.0181(0)	0.91
203	Lattice mode	--	$T \leq 120$	-0.0180(7)	0.89
211	Lattice mode	--	$T \leq 530$	-0.0213(0)	1.01
256	Lattice mode	--	$200 \leq T \leq 530$	-0.0297(1)	1.16
260	Lattice mode	B_1	$T \leq 180$	-0.0185(3)	0.71
266	Lattice mode	A_1	$T \leq 180$	-0.0394(3)	1.48
694	In-plane bend, ν_{4a}	A_1	$T \leq 530$	-0.0012(0)	0.02
709	In-plane bend, ν_{4b}	A_1	$T \leq 530$	-0.0032(0)	0.05
717	In-plane bend, ν_{4c}	A_2	$T \leq 530$	0.0023(0)	-0.03
731	In-plane bend, ν_{4d}	B_2	$T \leq 530$	-0.0121(0)	0.17
864	Out-of-plane bend, ν_2	A_1	$T \leq 530$	-0.0056(0)	0.07
1071	Symmetric stretch, ν_{1a}	A_1	$T \leq 530$	-0.0185(0)	0.17
1090	Symmetric stretch, ν_{1b}	A_1	$T \leq 530$	-0.0141(0)	0.13
1404	Asymmetric stretch, ν_{3a}	A_1	$T \leq 510$	-0.0183(1)	0.13
1433	Asymmetric stretch, ν_{3b}	A_2	$T \leq 495$	-0.0235(1)	0.16
1470	Asymmetric stretch, ν_{3c}	B_1	$T \leq 530$	-0.0179(0)	0.12
1512	Asymmetric stretch, ν_{3d}	A_1	$T \leq 530$	-0.0275(0)	0.18
1542	Asymmetric stretch, ν_{3e}	B_2	$T \leq 370$	-0.0485(1)	0.32
1549	Asymmetric stretch, ν_{3f}	B_2	$T \leq 435$	-0.0488(1)	0.32
1699	Overtone/combination	--	$T \leq 530$	-0.0026(0)	0.02
1706	Overtone/combination	--	$T \leq 530$	-0.0017(0)	0.01
1727	Overtone/combination	--	$T \leq 530$	-0.0095(0)	0.06
1732	Overtone/combination	--	$T \leq 530$	-0.0091(0)	0.05
1742	Overtone/combination	--	$T \leq 530$	-0.0119(0)	0.07

Supplemental Information

Chapter 2 supplemental information 1

Introduction

This document includes extra information relevant to the calculation of $\bar{v}_{H_2O}$ from the available shock compression data on enstatite, forsterite, and serpentine. Text sections S1-S4 describe our selection criteria for the experimental data and briefly characterize the Hugoniot of each mineral. Figures S1-S3 reproduce the experimental data along with our shockwave equation of state fits and temperature calculations. Figure S4 shows a series of calculated $\bar{v}_{H_2O}$ isotherms between 1000-9000 K (the shock isochor presented in Figure 2.1 of the main text was constructed from these isotherms). Table S1 shows shockwave equation of state fit parameters with associated uncertainties for each Hugoniot. Citations for the references in this document can be found in the bibliography of the main text.

Text S1. Experimental data selection criteria

In our analysis we only consider shock compression experiments on single crystal samples or polycrystalline samples whose bulk densities are within a few percent of crystal densities. Many shock compression experiments have been carried out on compositionally relevant porous and glass samples. However, due to their lower initial densities, glass and porous samples reach higher temperatures during shock compression and their Hugoniots deviate significantly from those of single crystal and polycrystalline samples. Additionally, datasets have been filtered to only include experimental (and not calculated) data. This is most significant with respect to the work

of Sekine et al. (2012), where the inclusion of calculated data points leads to physically implausible results for the very-high-pressure phase (>125 GPa) of serpentine (e.g., negative sound speed velocities and substantial density reductions with increasing pressure). Discarded shots are listed below.

- Sekine et al. (2012): #2, #3, #7
- Tyburczy et al. (1991) (discarded in original study as well as our calculations): 40-544-W, LGG-177-Al, LGG-179-Al, LGG-187-Al.
- Zhang et al. (2014): #14

Text S2. The forsterite Hugoniot

Mosenfelder et al. (2007) identified a transition to bridgmanite plus periclase that is complete by 100 GPa. They inferred a melt phase occurring between 130 – 150 GPa and note that forsterite and enstatite experience similar density increases upon melting at high pressures. Bolis et al. (2016) carried out decaying laser shock experiments on forsterite over the range 120 – 500 GPa and found no signatures of phase transitions in velocity or emission profiles. They offer two possible explanations: Mg_2SiO_4 persists as an undissociated phase on the Hugoniot due to slow reaction kinetics, or the existence of a eutectic point in the MgO-SiO_2/MgO-$MgSiO_3$ systems that results in MgO concentrations that are not high enough to generate a detectable signature with decaying shocks. Sekine et al. (2016) identified a number of phase transitions in their laser shock compression experiments on forsterite. They propose melting and subsequent incongruent crystallization of MgO over the interval 271 – 285

GPa; a transition of MgO from the B1 to B2 phase over the interval 285 – 344 GPa; melting of the B2 phase over the interval 470 – 500 GPa.

Text S3. The enstatite Hugoniot

Ahrens & Gaffney (1971) identified three distinct phase regimes along the enstatite Hugoniot: a low pressure phase between 0-16 GPa, a mixed phase regime between 16-32 GPa, and a high pressure phase at ≥32 GPa. Akins et al. (2004) identified a mixed phase regime persisting to 70 GPa, a transition to pv complete by 110-120 GPa, and melting at 170 GPa. Fratanduono et al. (2018) conducted laser-driven shock experiments on enstatite and suggested that melting along the Hugoniot is complete by 227 ± 10 GPa and 5745 ± 530 K. Hernandez et al. (2020) conducted laser-driven shock compression experiments on single crystal enstatite and determined the Hugoniot up to 337 GPa with in-situ x-ray diffraction. They identified a disordered, glasslike state that persists from 80 GPa up to the equilibrium melting pressure near 170 GPa.

Text S4. The serpentine Hugoniot

There have been fewer shock experiments conducted on serpentine than either enstatite or forsterite. Tyburczy et al. (1991) carried out shock compression experiments on polycrystalline samples of lizardite, antigorite, and chrysotile up to pressures of ~150 GPa. They propose a possibly amorphous low-pressure phase that persists up to about 40 GPa, a mixed phase regime between 40 – 55 GPa, a high-pressure phase between 55 – 125 GPa, and a very high-pressure phase beyond 125 GPa. Tyburczy et al. (1991) note that the high-pressure phase can be modeled as either mixed

oxides + H_2O or a brucite containing assemblage. The very high-pressure phase could represent incongruent melting – the density is approximately equal to 2Pv + Pc. Sekine et al. (2012) conducted shock compression experiments on antigorite and suggest a decomposition to a brc + st + pe or brc + pv assemblage at pressures greater than 60 GPa. Zhang et al. (2014) determined the Hugoniot of antigorite up to 130 GPa. They inferred three distinct regions of a lower pressure phase up to 43 GPa, a metastable extension appearing between 43-130 GPa for short compressions, and a high pressure phase at 43-80 GPa.

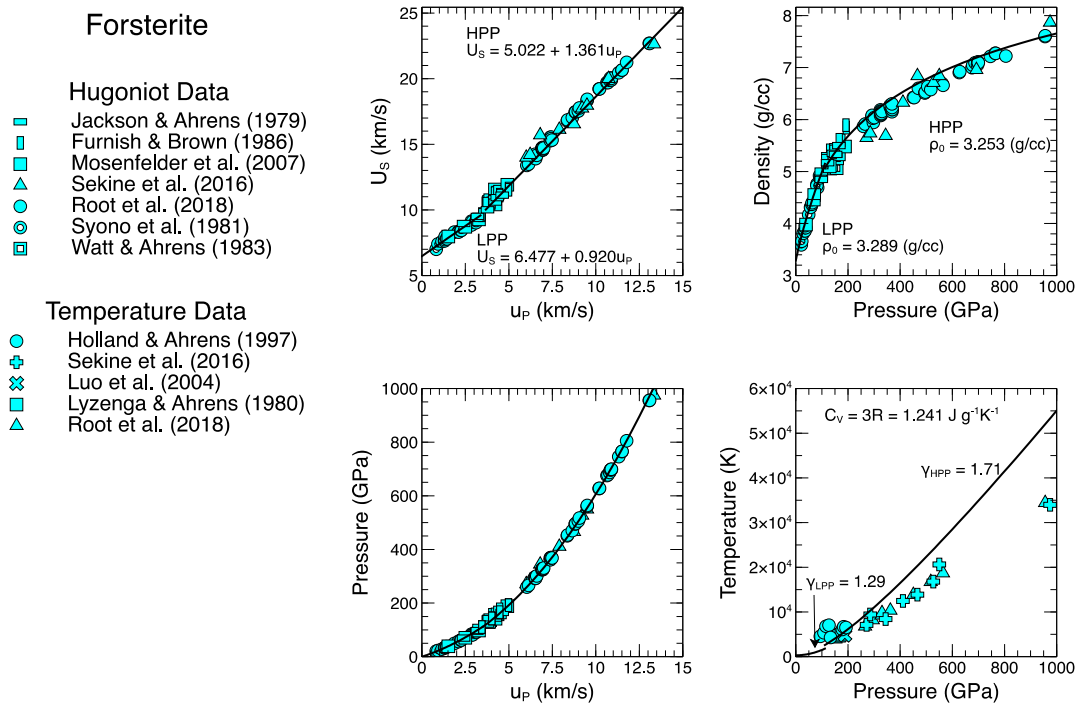

Figure S1 The forsterite Hugoniot. Experimental data are shown as cyan markers; fits and calculations are shown as solid black lines. Temperature along the Hugoniot was calculated with the method of Walsh & Christian (1955).

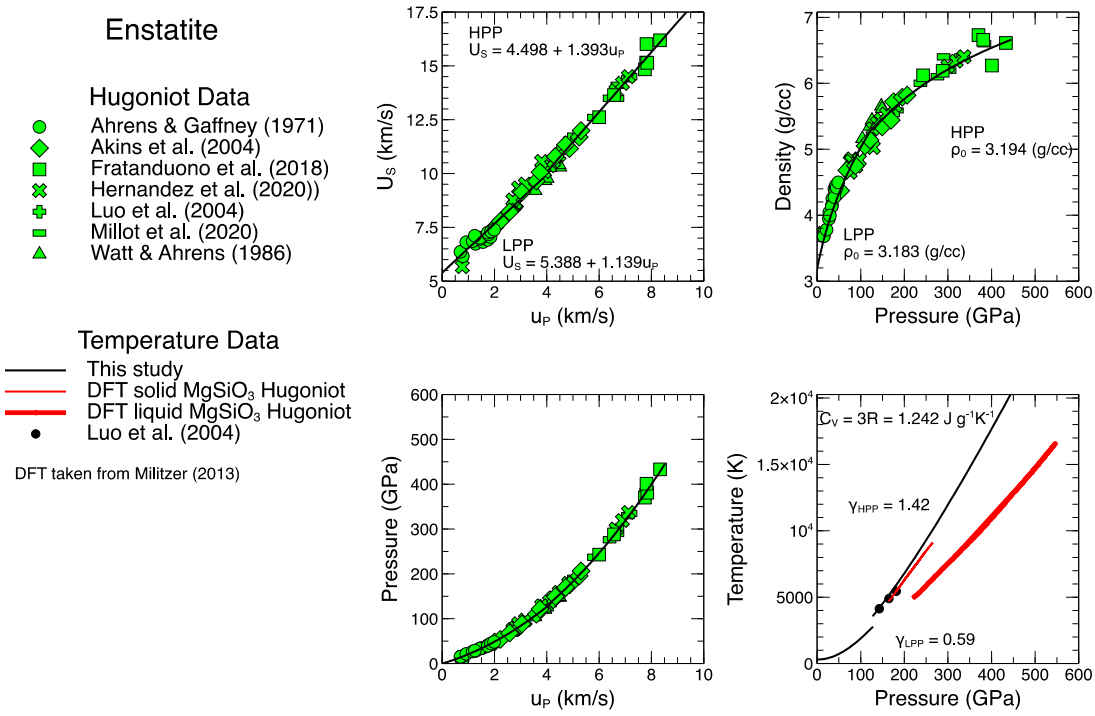

Figure S2 The enstatite Hugoniot. Experimental data are shown as green markers; fits and calculations are shown as solid black lines. Temperature along the Hugoniot was calculated with the method of Walsh & Christian (1955). We also include experimental temperature measurements (filled black circles) and the results of DFT calculations (red lines) for both liquid and solid $MgSiO_3$.

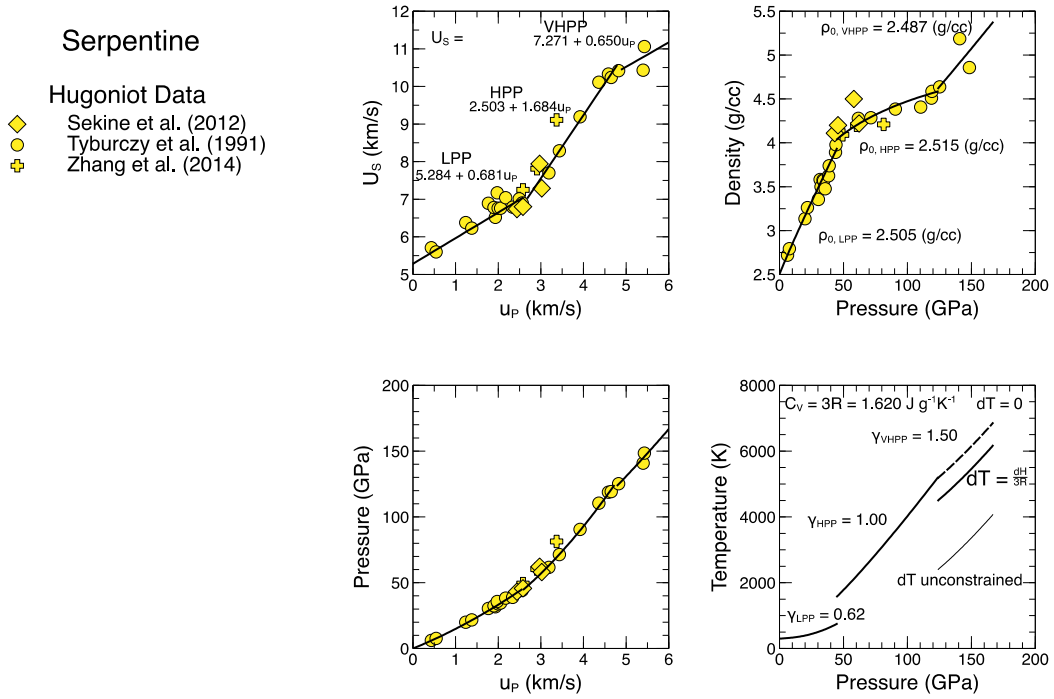

Figure S3 The serpentine Hugoniot. Experimental data are shown as yellow markers; fits and calculations are shown as solid black lines. Note that unlike the Hugoniot curves of forsterite and enstatite which are split into two branches, the serpentine Hugoniot is defined along three branches. In the last subplot we show three different assumptions for the transition from the high pressure phase to the very high pressure inferred melt phase: no temperature change; a temperature decrease constrained by dT=dH/3R, where H is the enthalpy and R is the gas constant; temperature change is unconstrained.

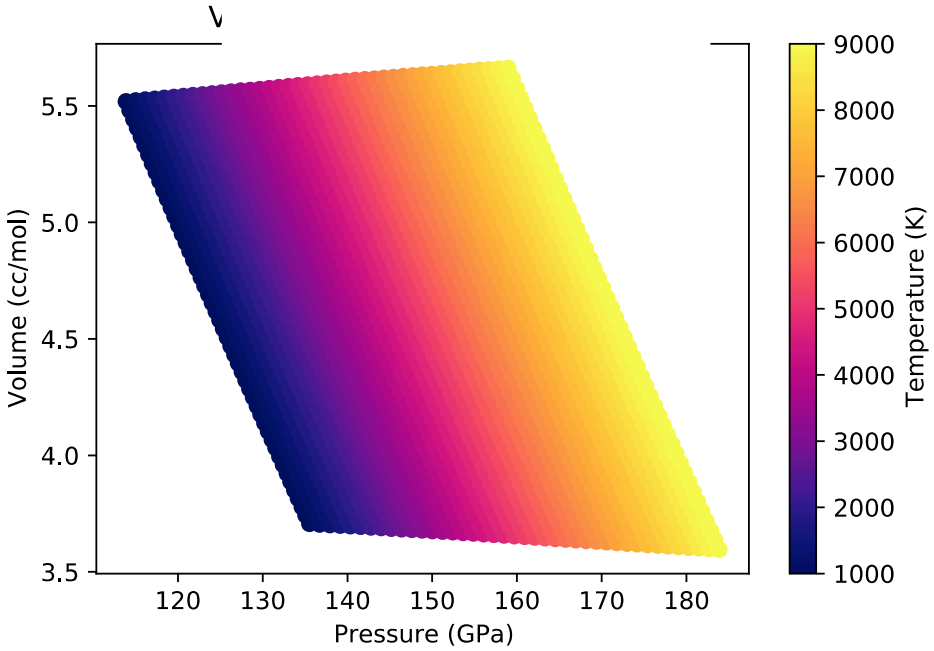

Figure S4. $\bar{v}_{H_2O}$ isotherms calculated from the forsterite, enstatite, and serpentine Hugoniots.

phase	**fit interval**	**S**	**±**	**C_0**	**±**	**ρ_0**	**±**
	(km/s)			**(km/s)**		**(g/cc)**	
Fo LPP	$u_P \leq 3.5$	0.920	(0.012)	6.477	(0.037)	3.289	(0.006)
Fo HPP	$u_P \geq 3.5$	1.361	(0.003)	5.022	(0.019)	3.253	(0.003)
Srp LPP	$u_P \leq 2.6$	0.681	(0.017)	5.284	(0.024)	2.505	(0.008)
Srp HPP	$2.6 \leq u_P \leq 4.8$	1.684	(0.043)	2.503	(0.171)	2.515	(0.006)
Srp VHPP	$u_P \geq 4.8$	0.650	(0.317)	7.271	(1.652)	2.487	(0.018)
En LPP	$u_P \leq 4.0$	1.139	(0.009)	5.388	(0.019)	3.183	(0.008)
En HPP	$u_P \geq 4.0$	1.393	(0.021)	4.498	(0.101)	3.194	(0.006)

Table S1. Shockwave equation of state parameters $\pm 1\sigma$ uncertainties for crystalline forsterite, enstatite, and serpentine. LPP = low pressure phase; HPP = high pressure phase; VHPP = very high pressure phase. Serpentine is the only mineral for a which a distinction is made between high pressure and very high pressure phases.

Chapter 2 Supplemental information 2

Introduction

The equation of state fits presented in Figure 2 of the main text were obtained by first transforming the pressure-volume measurements into stress-strain coordinates and then using nonlinear least squares (NLS) and orthogonal distance regression (ODR) routines to fit for the equation of state parameters. The transformation for the fourth order Birch-Murnaghan equation of state is

$$F(f) = P\left[3f(1+2f)^{5/2}\right]^{-1} = K_0(1 + af + bf^2) \qquad 1$$

Where $f = \frac{1}{2}[(V_0/V)^{2/3} - 1]$, $a = (3/2)(K' - 4)$, and $b = \frac{1}{6}\left(9K_T K_T'' + 9K_T'^2 - 63K_T' + 143\right)$. The third order form is obtained by setting $b = 0$. The transformation for the Vinet equation of state is

$$ln(H) = ln\left[\frac{P(1+z)^2}{3z}\right] = ln(K_T) + \frac{3z}{2}(K_T' - 1) \qquad 2$$

where $z = 1 - (V/V_0)^{1/3}$.

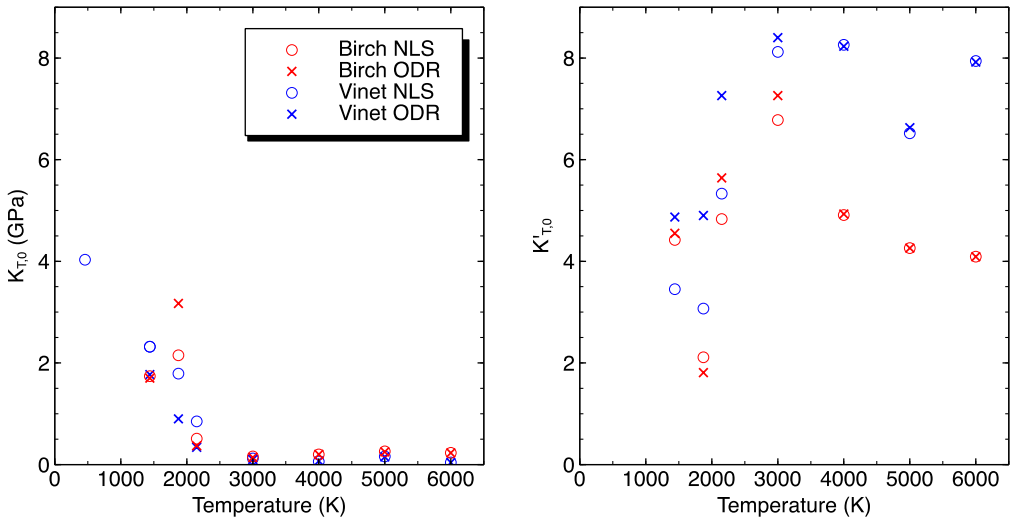

Figure S1. Isothermal bulk modulus and its pressure derivative plotted against mean bin temperature for each equation of state fit.

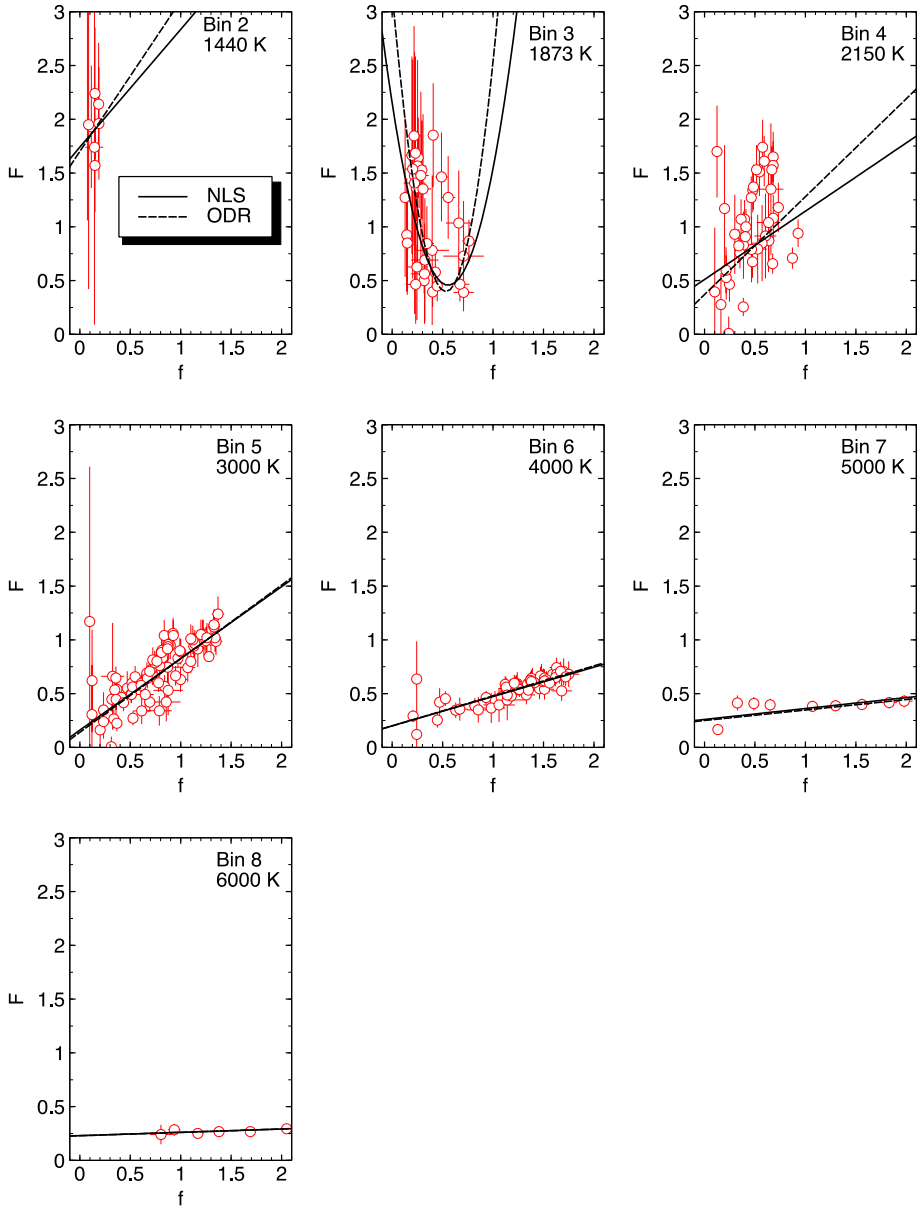

Figure S2. Birch-Murnaghan equation of state fits.

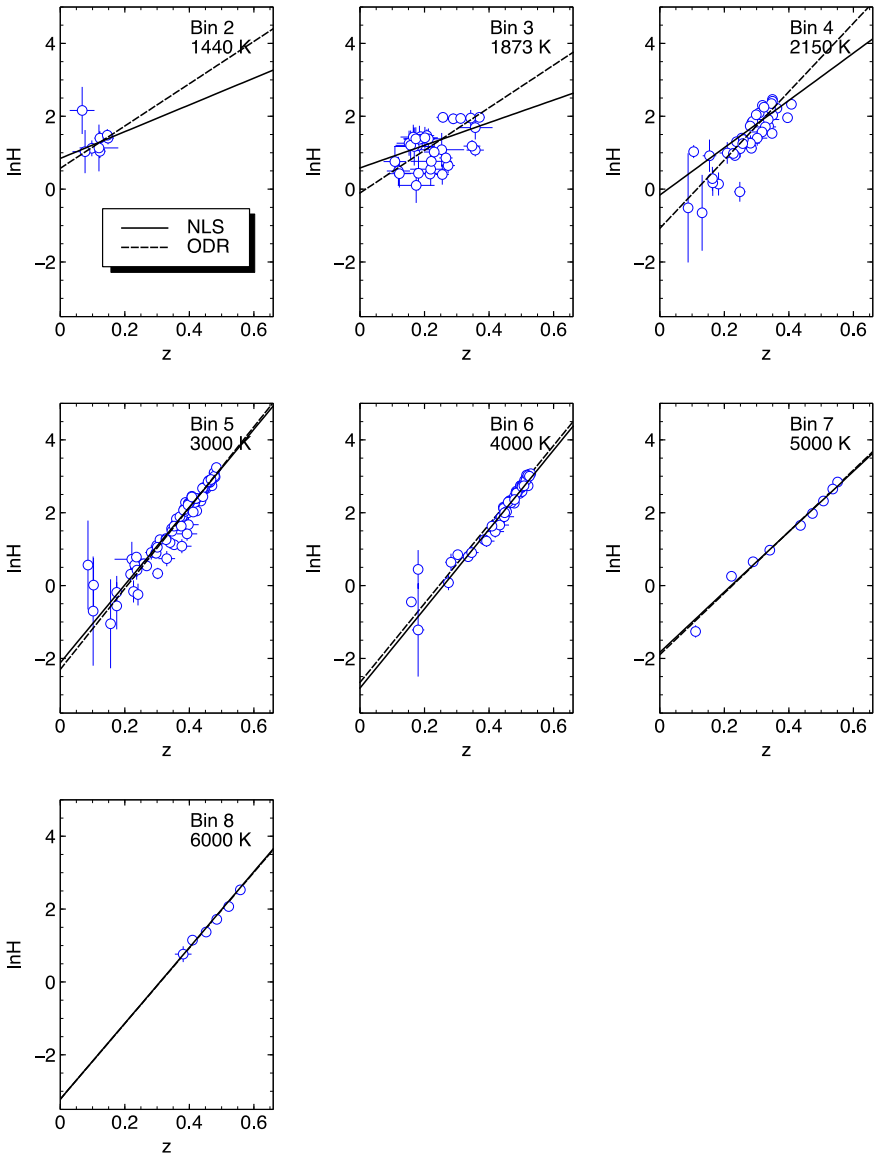

Figure S3. Vinet equation of state fits.

T [K]	*V_0 [cc/mol]*	*K [GPa]*	+-	*K′*	+-
1440	25.06	2.32	1.21	3.45	2.67
1873	30.03	1.79	0.22	3.07	0.32
2150	33.16	0.85	0.08	5.33	0.20
3000	42.85	0.12	0.01	8.12	0.09
4000	54.25	0.06	0.01	8.26	0.12
5000	65.65	0.16	0.02	6.52	0.14
6000	77.05	0.04	0.01	7.94	0.31

Table S1. Vinet nonlinear least squares fits.

T [K]	*V_0 [cc/mol]*	*K [GPa]*	+-	*K′*	+-
1440	25.06	1.77	2.57	4.87	7.53
1873	30.03	0.90	1.77	4.90	5.18
2150	33.16	0.34	0.74	7.26	4.69
3000	42.85	0.10	0.11	8.40	1.75
4000	54.25	0.07	0.07	8.23	1.47
5000	65.65	0.15	0.08	6.63	0.78
6000	77.05	0.04	0.03	7.92	1.00

Table S2. Vinet orthogonal distance regression fits.

T [K]	*V_0 [cc/mol]*	*K [GPa]*	+-	*K′*	+-	*K″ [GPa^{-1}]*	+-
1440	25.06	1.74	1.31	4.42	3.48	--	--
1873	30.03	2.15	0.40	2.11	0.23	-1.80	0.47
2150	33.16	0.51	0.08	4.83	0.31	--	--
3000	42.85	0.16	0.03	6.78	0.71	--	--
4000	54.25	0.20	0.04	4.91	0.26	--	--
5000	65.65	0.26	0.03	4.26	0.10	--	--
6000	77.05	0.23	0.05	4.09	0.11	--	--

Table S3. Birch-Murnaghan nonlinear least squares fits.

T [K]	V_0 [cc/mol]	K [GPa]	+-	K'	+-	K'' [GPa^{-1}]	+-
1440	25.06	1.70	1.30	4.55	3.65	--	--
1873	30.03	3.17	0.53	1.81	0.17	-1.40	0.31
2150	33.16	0.37	0.08	5.64	0.62	--	--
3000	42.85	0.14	0.03	7.26	0.94	--	--
4000	54.25	0.20	0.04	4.93	0.27	--	--
5000	65.65	0.25	0.03	4.26	0.10	--	--
6000	77.05	0.23	0.05	4.09	0.11	--	--

Table S4. Birch-Murnaghan orthogonal distance regression fits.

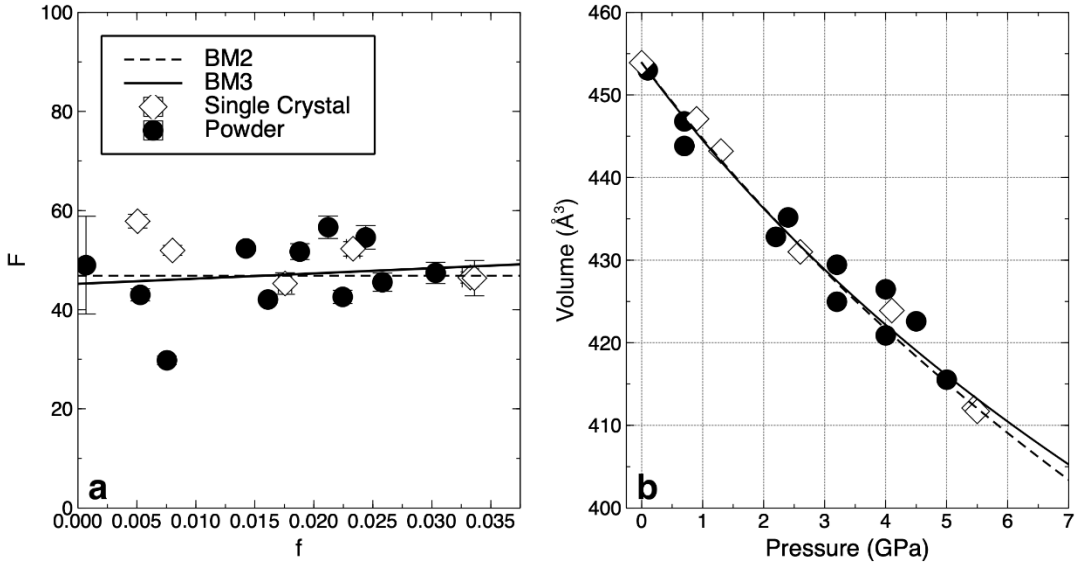

Figure SI 1 Eulerian stress-strain fit to the bütschliite ($R\bar{3}m$) x-ray diffraction data (a). Compression curves plotted with pressure-volume data from the x-ray diffraction measurements (b). BM2 and BM3 refer to the 2nd- and 3rd-order Birch-Murnaghan equations of state. The Eulerian stress-strain data were fit with an orthogonal distance regression to account for uncertainties in both pressure and volume. BM2 fit parameters: V_0 = 453.9(5) Å^3, K_0 = 46.9(17) GPa, K' = 4. BM3 fit parameters: V_0 = 453.9(5) Å^3, K_0 = 45.2(45) GPa, K' = 5.5(41).

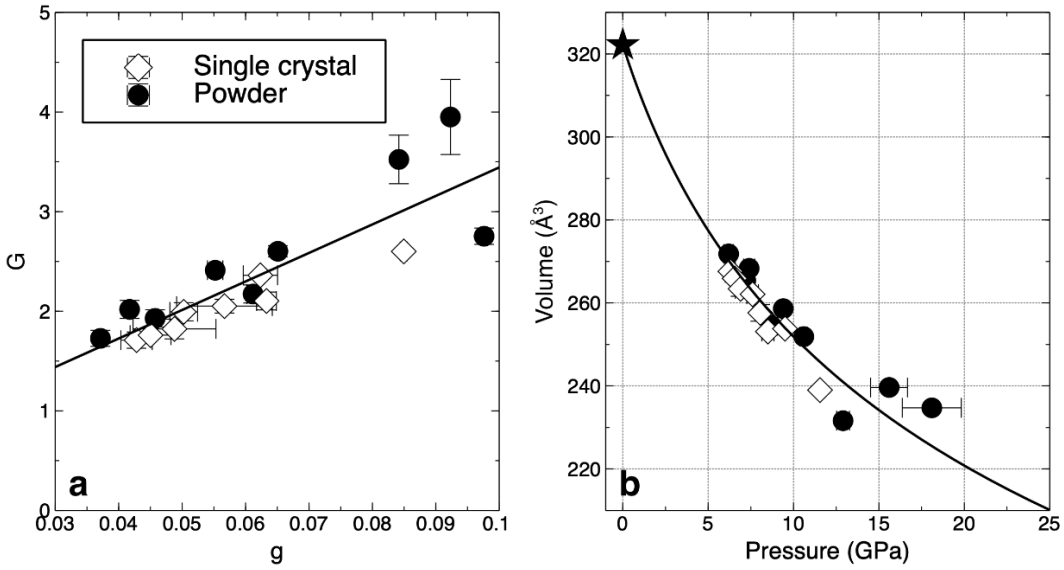

Figure SI 2 Equation of state fit to the bütschliite-II (C2/m) diffraction data following the method of Jeanloz (1981). V_0 = 322.2 Å^3, K_0 = 24.8(44) GPa, K' = 4.0(11).

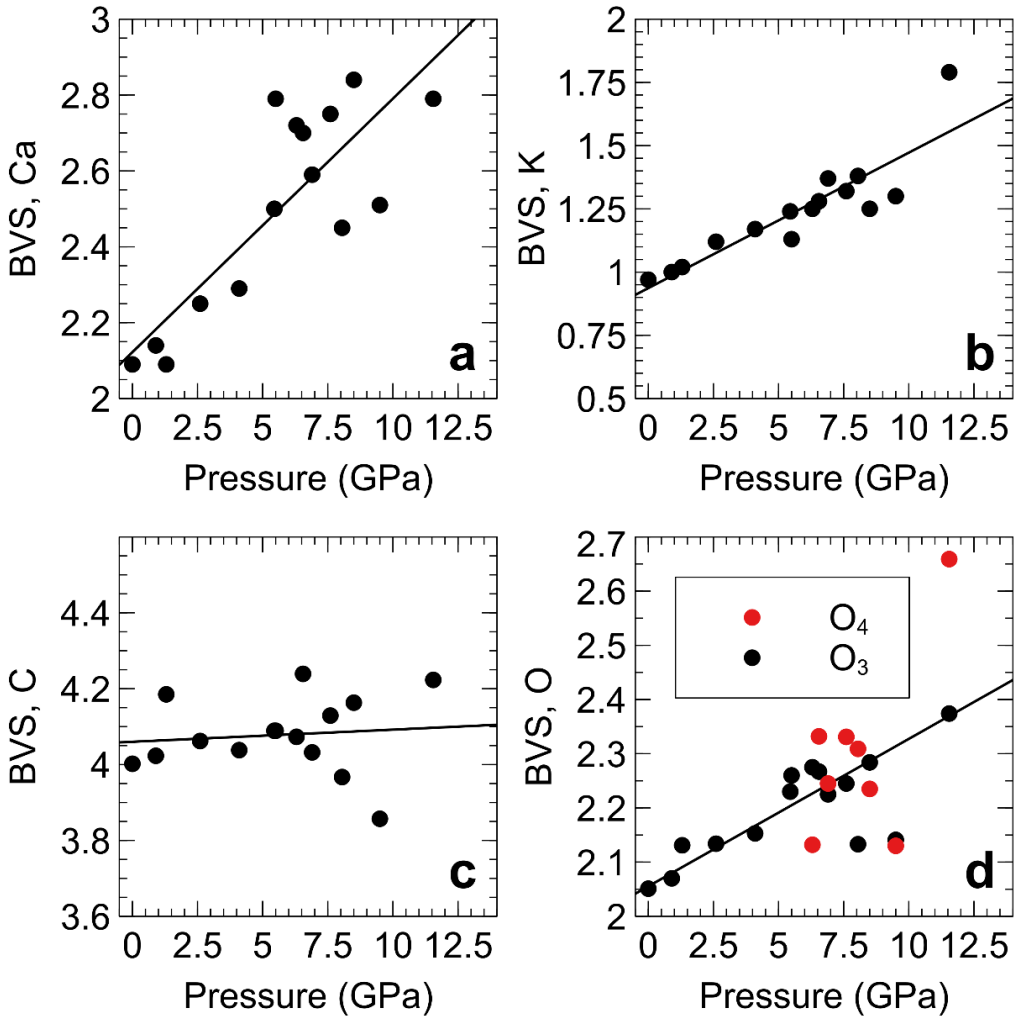

Figure SI 3 Bond valence sums calculated for bütschliite-I and bütschliite-II: calcium (a), potassium (b), carbon (c), and oxygen (d).

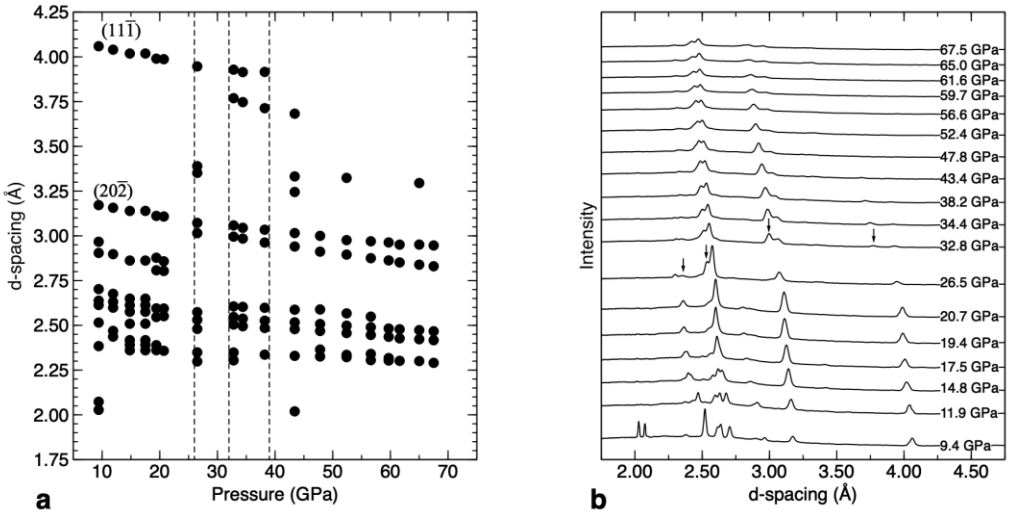

Figure SI 3 d-spacings (a) and powder patterns (b) of $K_2Ca(CO_3)_2$ taken on compression. Measurements were collected with the sample in a Ne PTM.

Pressure (GPa)	a (Å)	+-	b (Å)	+-	c (Å)	+-	V (Å^3)	+-	Z	V/Z	beta	+-	Phase	Method
0.0	5.379	0.002	5.379	0.002	18.115	0.010	453.9	0.5	3	151.3	–	–	bütschliite-I	Single xtal
0.1	5.377	0.000	5.377	0.000	18.089	0.001	453.0	0.0	3	151.0	–	–	bütschliite-I	Powder
0.7	5.356	0.001	5.356	0.001	17.864	0.002	443.8	0.1	3	147.9	–	–	bütschliite-I	Powder
0.7	5.368	0.000	5.368	0.000	17.907	0.000	446.8	0.0	3	148.9	–	–	bütschliite-I	Powder
0.9	5.378	0.005	5.378	0.005	17.850	0.030	447.1	0.1	3	149.0	–	–	bütschliite-I	Single xtal
1.3	5.359	0.006	5.359	0.006	17.820	0.030	443.2	0.1	3	147.7	–	–	bütschliite-I	Single xtal
2.2	5.337	0.002	5.337	0.002	17.549	0.004	432.8	0.1	3	144.3	–	–	bütschliite-I	Powder
2.4	5.348	0.000	5.348	0.000	17.568	0.001	435.2	0.0	3	145.1	–	–	bütschliite-I	Powder
2.6	5.341	0.004	5.341	0.004	17.448	0.017	431.0	0.7	3	143.7	–	–	bütschliite-I	Single xtal
3.2	5.325	0.000	5.325	0.000	17.304	0.001	425.0	0.0	3	141.7	–	–	bütschliite-I	Powder
3.2	5.341	0.001	5.341	0.001	17.384	0.001	429.4	0.0	3	143.1	–	–	bütschliite-I	Powder
4.0	5.32	0.001	5.32	0.001	17.175	0.001	420.9	0.0	3	140.3	–	–	bütschliite-I	Powder
4.0	5.343	0.000	5.343	0.000	17.253	0.001	426.5	0.0	3	142.2	–	–	bütschliite-I	Powder
4.1	5.338	0.004	5.338	0.004	17.179	0.017	423.9	0.7	3	141.3	–	–	bütschliite-I	Single xtal
4.5	5.328	0.001	5.328	0.001	17.193	0.003	422.6	0.1	3	140.9	–	–	bütschliite-I	Powder
5.0	5.316	0.002	5.316	0.002	16.976	0.004	415.5	0.2	3	138.5	–	–	bütschliite-I	Powder
5.5	5.311	0.004	5.311	0.004	16.872	0.020	412.1	0.8	3	137.4	–	–	bütschliite-I	Single xtal
5.5	5.307	0.005	5.307	0.005	16.880	0.020	411.7	0.1	3	137.2	–	–	bütschliite-I	Single xtal
6.2	9.247	0.019	5.33	0.001	6.446	0.009	271.8	0.1	2	135.9	121.17	0.02	bütschliite-II	Powder
6.3	9.182	0.007	5.299	0.006	6.354	0.011	267.6	0.7	2	133.8	120.06	0.03	bütschliite-II	Single xtal
6.6	9.179	0.017	5.29	0.009	6.349	0.014	265.9	0.9	2	133.0	120.40	0.05	bütschliite-II	Single xtal
6.9	9.17	0.030	5.28	0.020	6.320	0.030	263.4	1.8	2	131.7	120.60	0.10	bütschliite-II	Single xtal
7.2	9.125	0.027	5.293	0.001	6.455	0.013	265.4	0.1	2	132.7	121.66	0.03	bütschliite-II	Powder
7.4	9.222	0.026	5.305	0.001	6.491	0.013	268.3	0.1	2	134.2	122.33	0.03	bütschliite-II	Powder
7.6	9.076	0.007	5.273	0.005	6.437	0.007	262.1	0.6	2	131.0	121.70	0.03	bütschliite-II	Single xtal
8.1	9.134	0.014	5.221	0.007	6.370	0.040	257.6	2.0	2	128.8	122.00	0.15	bütschliite-II	Single xtal
8.5	9.004	0.007	5.238	0.005	6.391	0.007	253.1	0.4	2	126.6	122.88	0.02	bütschliite-II	Single xtal
8.7	9.165	0.149	5.297	0.002	6.139	0.069	254.5	0.3	2	127.3	121.35	0.18	bütschliite-II	Powder
9.4	9.081	0.051	5.265	0.004	6.480	0.029	258.6	0.3	2	129.3	123.41	0.07	bütschliite-II	Powder
9.5	9.051	0.009	5.225	0.007	6.421	0.013	253.8	0.7	2	126.9	123.30	0.03	bütschliite-II	Single xtal
10.6	9.099	0.049	5.361	0.001	6.303	0.024	251.9	0.1	2	125.9	124.99	0.06	bütschliite-II	Powder
11.6	8.95	0.020	5.12	0.012	6.290	0.020	239.0	0.1	2	119.5	124.00	0.09	bütschliite-II	Single xtal
12.9	8.864	0.078	4.986	0.002	6.410	0.040	231.6	0.1	2	115.8	125.16	0.09	bütschliite-II	Powder
15.6	9.154	0.064	5.226	0.003	6.271	0.030	239.6	0.1	2	119.8	126.99	0.07	bütschliite-II	Powder
18.1	8.943	0.029	5.247	0.001	6.270	0.014	234.7	0.0	2	117.4	127.09	0.03	bütschliite-II	Powder

Table SI 1 Lattice parameters from single crystal and powder x-ray diffraction measurements.

Bibliography

Abersteiner, A., Golovin, A., Chayka, I., Kamenetsky, V. S., Goemann, K., Rodemann, T., & Ehrig, K. (2022). Carbon compounds in the West Kimberley lamproites (Australia): Insights from melt and fluid inclusions. *Gondwana Research*, *109*, 536–557. https://doi.org/10.1016/j.gr.2022.06.005

Agee, C. B. (2008a). Compressibility of water in magma and the prediction of density crossovers in mantle differentiation. *Philosophical Transactions of the Royal Society A: Mathematical, Physical and Engineering Sciences*, *366*(1883), 4239–4252. https://doi.org/10.1098/rsta.2008.0071

Agee, C. B. (2008b). Static compression of hydrous silicate melt and the effect of water on planetary differentiation. *Earth and Planetary Science Letters*, *265*(3–4), 641–654. https://doi.org/10.1016/j.epsl.2007.11.010

Agnor, C., Canup, R. M., & Levison, H. F. (1999). On the character and consequences of large impacts in the late stage of terrestrial planet formation. *Icarus*, *142*(1), 219–237. https://doi.org/10.1006/icar.1999.6201

Ahrens, T. J. (1993). High-pressure shock compression of solids. In J. R. Asay & M. Shahinpoor (Eds.), *High Pressure Shock Compression of Solids* (pp. 75–114). Springer New York. https://doi.org/10.1007/978-1-4612-0911-9

Ahrens, T. J., & Gaffney, E. S. (1971). Dynamic compression of enstatite. *Journal of Geophysical Research*, *76*(23), 5504–5513. https://doi.org/10.1029/JB076i023p05504

Akahama, Y., & Kawamura, H. (2006). Pressure calibration of diamond anvil Raman gauge to 310GPa. *Journal of Applied Physics*, *100*(4), 043516. https://doi.org/10.1063/1.2335683

Akaogi, M., Tanaka, A., & Ito, E. (2002). Garnet–ilmenite–perovskite transitions in the system $Mg_4Si_4O_{12}$–$Mg_3Al_2Si_3O_{12}$ at high pressures and high temperatures: Phase equilibria, calorimetry and implications for mantle structure. *Physics of the Earth and Planetary Interiors*, *132*(4), 303–324. https://doi.org/10.1016/S0031-9201(02)00075-4

Akella, A., & Keszler, D. A. (1995a). Crystal structure of the borate $Ba_2Ca(BO_3)_2$. *Main Group Metal Chemistry*, *18*(1), 35–42. https://doi.org/10.1515/mgmc.1995.18.1.35

Akella, A., & Keszler, D. A. (1995b). Structure and Eu^{2+} luminescence of dibarium magnesium orthoborate. *Materials Research Bulletin*, *30*(1), 105–111. https://doi.org/10.1016/0025-5408(94)00113-8

Akins, J. A., Luo, S.-N., Asimow, P. D., & Ahrens, T. J. (2004). Shock-induced melting of $MgSiO_3$ perovskite and implications for melts in Earth's lowermost mantle. *Geophysical Research Letters*, *31*(14). https://doi.org/10.1029/2004GL020237

Anderson, O. L. (1967). Equation for thermal expansivity in planetary interiors. *Journal of Geophysical Research*, *72*(14), 3661–3668. https://doi.org/10.1029/JZ072i014p03661

Anderson, O. L. (1982). The Earth's core and the phase diagram of iron. *Philosophical Transactions of the Royal Society of London. Series A, Mathematical and Physical Sciences*. https://doi.org/10.1098/rsta.1982.0063

Anderson, O. L., & Isaak, D. G. (1993). The dependence of the Anderson-Grüneisen parameter δ_T upon compression at extreme conditions. *Journal of Physics and Chemistry of Solids*, *54*(2), 221–227. https://doi.org/10.1016/0022-3697(93)90313-G

Andrault, D., Pesce, G., Bouhifd, M. A., Bolfan-Casanova, N., Hénot, J.-M., & Mezouar, M. (2014). Melting of subducted basalt at the core-mantle boundary. *Science*, *344*(6186), 892–895. https://doi.org/10.1126/science.1250466

Arefiev, A. V., Shatskiy, A., Podborodnikov, I. V., & Litasov, K. D. (2018). Melting and subsolidus phase relations in the system K_2CO_3–$MgCO_3$ at 3 GPa. *High Pressure Research*, *38*(4), 422–439. https://doi.org/10/gncqwj

Arefiev, A. V., Shatskiy, A., Podborodnikov, I. V., Rashchenko, S. V., Chanyshev, A. D., & Litasov, K. D. (2019). The system K_2CO_3–$CaCO_3$ at 3 GPa: Link between phase relations and variety of K–Ca double carbonates at ≤ 0.1 and 6 GPa. *Physics and Chemistry of Minerals*, *46*(3), 229–244. https://doi.org/10/gncqwk

Arkani-Hamed, J., & Olson, P. (2010). Giant impact stratification of the Martian core. *Geophysical Research Letters*, *37*(2). https://doi.org/10.1029/2009GL041417

Bagley, B., Courtier, A. M., & Revenaugh, J. (2009). Melting in the deep upper mantle oceanward of the Honshu slab. *Physics of the Earth and Planetary Interiors*, *175*(3–4), 137–144. https://doi.org/10.1016/j.pepi.2009.03.007

Bagley, B., & Revenaugh, J. (2008). Upper mantle seismic shear discontinuities of the Pacific. *Journal of Geophysical Research: Solid Earth*, *113*(12), 1–9. https://doi.org/10.1029/2008JB005692

Bajgain, S., Ghosh, D. B., & Karki, B. B. (2015). Structure and density of basaltic melts at mantle conditions from first-principles simulations. *Nature Communications*, *6*(1), 8578. https://doi.org/10.1038/ncomms9578

Bajgain, S. K., Peng, Y., Mookherjee, M., Jing, Z., & Solomon, M. (2019). Properties of hydrous aluminosilicate melts at high pressures. *ACS Earth and Space Chemistry*, *3*(3), 390–402. https://doi.org/10.1021/acsearthspacechem.8b00157

Balkanski, M., Wallis, R. F., & Haro, E. (1983). Anharmonic effects in light scattering due to optical phonons in silicon. *Physical Review B*, *28*(4), 1928–1934. https://doi.org/10.1103/PhysRevB.28.1928

Ballirano, P. (2011). Thermal behaviour of natrite Na_2CO_3 in the 303–1013 K thermal range. *Phase Transitions*, *84*(4), 357–379. https://doi.org/10.1080/01411594.2010.541856

Balta, J. B., & McSween Jr., H. Y. (2013). Application of the MELTS algorithm to Martian compositions and implications for magma crystallization. *Journal of Geophysical Research: Planets*, *118*(12), 2502–2519. https://doi.org/10.1002/2013JE004461

Bayarjargal, L., Fruhner, C.-J., Schrodt, N., & Winkler, B. (2018). $CaCO_3$ phase diagram studied with Raman spectroscopy at pressures up to 50 GPa and high temperatures and DFT modeling. *Physics of the Earth and Planetary Interiors*, *281*, 31–45. https://doi.org/10.1016/j.pepi.2018.05.002

Belonoshko, A., & Saxena, S. K. (1991). A molecular dynamics study of the pressure-volume-temperature properties of super-critical fluids: I. H_2O. *Geochimica et Cosmochimica Acta*, *55*(1), 381–387. https://doi.org/10.1016/0016-7037(91)90425-5

Bertka, C. M., & Fei, Y. (1997). Mineralogy of the Martian interior up to core-mantle boundary pressures. *Journal of Geophysical Research: Solid Earth*, *102*(B3), 5251–5264. https://doi.org/10.1029/96JB03270

Birch, F. (1978). Finite strain isotherm and velocities for single-crystal and polycrystalline NaCl at high pressures and 300°K. *Journal of Geophysical Research*, *83*(B3), 1257. https://doi.org/10.1029/JB083iB03p01257

Boggs, P. T., Byrd, R. H., Rogers, J. E., & Schnabel, R. B. (1992). User's reference guide for ODRPACK version 2.01 software for weighted orthogonal distance regression. *U.S. Department of Commerce*, *June*, 99.

Bolis, R. M., Morard, G., Vinci, T., Ravasio, A., Bambrink, E., Guarguaglini, M., Koenig, M., Musella, R., Remus, F., Bouchet, J., Ozaki, N., Miyanishi, K., Sekine, T., Sakawa, Y., Sano, T., Kodama, R., Guyot, F., & Benuzzi-Mounaix, A. (2016). Decaying shock studies of phase transitions in MgO-SiO_2 systems: Implications for the super-Earths' interiors. *Geophysical Research Letters*, *43*(18), 9475–9483. https://doi.org/10.1002/2016GL070466

Bottinga, Y., Weill, D., & Richet, P. (1982). Density calculations for silicate liquids. I. Revised method for aluminosilicate compositions. *Geochimica et Cosmochimica Acta*, *46*(6), 909–919. https://doi.org/10.1016/0016-7037(82)90047-3

Bouhifd, M. A., Whittington, A. G., & Richet, P. (2015). Densities and volumes of hydrous silicate melts: New measurements and predictions. *Chemical Geology*, *418*, 40–50. https://doi.org/10.1016/j.chemgeo.2015.01.012

Bouvier, L. C., Costa, M. M., Connelly, J. N., Jensen, N. K., Wielandt, D., Storey, M., Nemchin, A. A., Whitehouse, M. J., Snape, J. F., Bellucci, J. J., Moynier, F., Agranier, A., Gueguen, B., Schönbächler, M., & Bizzarro, M. (2018). Evidence for extremely rapid magma ocean crystallization and crust formation on Mars. *Nature*, *558*(7711), 586–589. https://doi.org/10.1038/s41586-018-0222-z

Breuer, D., Labrosse, S., & Spohn, T. (2010). Thermal evolution and magnetic field generation in terrestrial planets and satellites. *Space Science Reviews*, *152*(1), 449–500. https://doi.org/10.1007/s11214-009-9587-5

Brey, G. P., Bulatov, V. K., & Girnis, A. V. (2011). Melting of K-rich carbonated peridotite at 6–10 GPa and the stability of K-phases in the upper mantle. *Chemical Geology*, *281*(3–4), 333–342. https://doi.org/10.1016/j.chemgeo.2010.12.019

Brown, J. M., & Shankland, T. J. (1981). Thermodynamic parameters in the Earth as determined from seismic profiles. *Geophysical Journal International*, *66*(3), 579–596. https://doi.org/10.1111/j.1365-246X.1981.tb04891.x

Bruker. (2016). *APEX3*. Bruker AXS Inc, Madison

Burnham, C. W., & Davis, N. F. (1971). The role of H_2O in silicate melts; I, P-V-T relations in the system $NaAlSi_3O_8$-H_2O to 10 kilobars and 1000°C. *American Journal of Science*, *270*(1), 54–79. https://doi.org/10.2475/ajs.270.1.54

Caracas, R., & Bobocioiu, E. (2011). The WURM project—A freely available web-based repository of computed physical data for minerals. *American Mineralogist*, *96*(2–3), 437–443. https://doi.org/10.2138/am.2011.3532

Carmichael, I. S. E., Nicholls, J., Spera, F. J., Wood, B. J., Nelson, S. A., Bailey, D. K., Smith, J. V., O'Hara, M. J., Horne, J. E. T., & Dunham, K. C. (1997). High-temperature properties of silicate liquids: Applications to the equilibration and ascent of basic magma. *Philosophical Transactions of the Royal Society of London. Series A, Mathematical and Physical Sciences*, *286*(1336), 373–431. https://doi.org/10.1098/rsta.1977.0124

Carper, W. R., Wahlbeck, P. G., & Griffiths, T. R. (2012). DFT models of molecular species in carbonate molten salts. *The Journal of Physical Chemistry B*, *116*(18), 5559–5567. https://doi.org/10.1021/jp3016694

Chayka, I. F., Kamenetsky, V. S., Vladykin, N. V., Kontonikas-Charos, A., Prokopyev, I. R., Stepanov, S. Y., & Krasheninnikov, S. P. (2021). Origin of alkali-rich volcanic and alkali-poor intrusive carbonatites from a common parental magma. *Scientific Reports*, 14. https://doi.org/10.1038/s41598-021-97014-y

Chizmeshya, A. V. G., Bauer, M. R., & Kouvetakis, J. (2003). Experimental and theoretical study of deviations from Vegard's Law in the Sn_xGe_{1-x} system. *Chemistry of Materials*, *15*(13). https://doi.org/10.1021/cm0300011

Closmann, C., & Williams, Q. (1995). In-situ spectroscopic investigation of high-pressure hydrated (Mg,Fe)SiO_3 glasses: OH vibrations as a probe of glass structure. *American Mineralogist*, *80*, 201–212. https://doi.org/10.2138/am-1995-3-401

Cohen, R. E., Gülseren, O., & Hemley, R. J. (2000). Accuracy of equation-of-state formulations. *American Mineralogist*, *85*(2), 338–344. https://doi.org/10.2138/am-2000-2-312

Cooper, A. F., Gittins, J., & Tuttle, O. F. (1975). The system Na_2CO_3-K_2CO_3-$CaCO_3$ at 1 kilobar and its significance in carbonatite petrogenesis. *American Journal of Science*, *275*(5), 534–560. https://doi.org/10.2475/ajs.275.5.534

Cottaar, S., Heister, T., Rose, I., & Unterborn, C. (2014). BurnMan: A lower mantle mineral physics toolkit. *Geochemistry, Geophysics, Geosystems*, *15*(4), 1164–1179. https://doi.org/10.1002/2013GC005122

Courtier, A. M., & Revenaugh, J. (2007). Deep upper-mantle melting beneath the Tasman and Coral Seas detected with multiple ScS reverberations. *Earth and Planetary Science Letters*, *259*(1–2), 66–76. https://doi.org/10/d8qcrn

Dahm, H. H., Gao, S. S., Kong, F., & Liu, K. H. (2017). Topography of the mantle transition zone discontinuities beneath Alaska and its geodynamic implications: Constraints from receiver function stacking. *Journal of Geophysical Research: Solid Earth*, *122*(12), 10,352-10,363. https://doi.org/10.1002/2017JB014604

Daines, M. J., & Kohlstedt, D. L. (1997). Influence of deformation on melt topology in peridotites. *Journal of Geophysical Research: Solid Earth*, *102*(B5), 10257–10271. https://doi.org/10.1029/97JB00393

Decius, J. C. (1955). Coupling of the out-of-plane bending mode in nitrates and carbonates of the aragonite structure. *The Journal of Chemical Physics*, *23*(7), 1290–1294. https://doi.org/10.1063/1.1742260

Dickens, B., Hyman, A., & Brown, W. E. (1971). Crystal structure of $Ca_2Na_2(CO_3)_3$ (shortite). *Journal of Research of the National Bureau of Standards. Section A, Physics and Chemistry*, *75A*(2), 129–135. https://doi.org/10.6028/jres.075A.013

Dreibus, G., & Wänke, H. (1984). Accretion of the Earth and inner planets. *Proc. 27th Intern. Geol. Con.*, *11*, 1–20.

Du, Z., Deng, J., Miyazaki, Y., Mao, H., Karki, B. B., & Lee, K. K. M. (2019). Fate of hydrous Fe-rich silicate melt in Earth's deep mantle. *Geophysical Research Letters*, *46*(16), 9466–9473. https://doi.org/10.1029/2019GL083633

Duffy, T. S., & Ahrens, T. J. (1993). Thermal expansion of mantle and core materials at very high pressures. *Geophysical Research Letters*, *20*(11), 1103–1106. https://doi.org/10/cb8j7s

Dufils, T., Sator, N., & Guillot, B. (2020). A comprehensive molecular dynamics simulation study of hydrous magmatic liquids. *Chemical Geology*, *533*(2019), 119300. https://doi.org/10.1016/j.chemgeo.2019.119300

Dziewonski, A. M., & Anderson, D. L. (1981). Preliminary reference Earth model. *Physics of the Earth and Planetary Interiors*, *25*(4), 297–356. https://doi.org/10.1016/0031-9201(81)90046-7

Efthimiopoulos, I., Müller, J., Winkler, B., Otzen, C., Harms, M., Schade, U., & Koch-Müller, M. (2019). Vibrational response of strontianite at high pressures and high temperatures and construction of P–T phase diagram. *Physics and Chemistry of Minerals*, *46*(1), 27–35. https://doi.org/10.1007/s00269-018-0984-8

Elkins-Tanton, L. T. (2008). Linked magma ocean solidification and atmospheric growth for Earth and Mars. *Earth and Planetary Science Letters*, *271*(1–4), 181–191. https://doi.org/10/fhzzb6

Elkins-Tanton, L. T. (2012). Magma oceans in the inner solar system. *Annual Review of Earth and Planetary Sciences*, *40*(1), 113–139. https://doi.org/10.1146/annurev-earth-042711-105503

Elkins-Tanton, L. T., Parmentier, E. M., & Hess, P. C. (2003). Magma ocean fractional crystallization and cumulate overturn in terrestrial planets: Implications for Mars. *Meteoritics & Planetary Science*, *38*(12), 1753–1771. https://doi.org/10.1111/j.1945-5100.2003.tb00013.x

Farsang, S., Facq, S., & Redfern, S. (2018). Raman modes of carbonate minerals as pressure and temperature gauges up to 6 GPa and 500°C. *American Mineralogist*. https://doi.org/10/gmrzph

Faul, U. H. (1997). Permeability of partially molten upper mantle rocks from experiments and percolation theory. *Journal of Geophysical Research: Solid Earth*, *102*(B5), 10299–10311. https://doi.org/10/dc6jk2

Fratanduono, D. E., Millot, M., Kraus, R. G., Spaulding, D. K., Collins, G. W., Celliers, P. M., & Eggert, J. H. (2018). Thermodynamic properties of $MgSiO_3$ at super-Earth mantle conditions. *Physical Review B*, *97*(21), 214105. https://doi.org/10.1103/PhysRevB.97.214105

Freitas, D., Manthilake, G., Schiavi, F., Chantel, J., Bolfan-Casanova, N., Bouhifd, M. A., & Andrault, D. (2017). Experimental evidence supporting a global melt layer at the base of the Earth's upper mantle. *Nature Communications*, *8*(1), 2186. https://doi.org/10.1038/s41467-017-02275-9

Furnish, M. D., & Brown, J. M. (1986). Shock loading of single-crystal olivine in the 100–200 GPa range. *Journal of Geophysical Research*, *91*(B5), 4723. https://doi.org/10.1029/jb091ib05p04723

Gao, W., Matzel, E., & Grand, S. P. (2006). Upper mantle seismic structure beneath eastern Mexico determined from P and S waveform inversion and its implications. *Journal of Geophysical Research: Solid Earth*, *111*(B8), 2006JB004304. https://doi.org/10.1029/2006JB004304

Ghiorso, M. S., Hirschmann, M. M., Reiners, P. W., & Kress III, V. C. (2002). The pMELTS: A revision of MELTS for improved calculation of phase relations and major element partitioning related to partial melting of the mantle to 3 GPa. *Geochemistry, Geophysics, Geosystems*, *3*(5), 1–35. https://doi.org/10.1029/2001GC000217

Ghosh, S., Litasov, K., & Ohtani, E. (2014). Phase relations and melting of carbonated peridotite between 10 and 20 GPa: A proxy for alkali- and CO_2-rich silicate melts in the deep mantle. *Contributions to Mineralogy and Petrology*, *167*(2), 964. https://doi.org/10/ghvmrc

Gillet, P., Biellmann, C., Reynard, B., & McMillan, P. (1993). Raman spectroscopic studies of carbonates part I: High-pressure and high-temperature behaviour of calcite, magnesite, dolomite and aragonite. *Physics and Chemistry of Minerals*, *20*(1). https://doi.org/10.1007/BF00202245

Golubkova, A., Merlini, M., & Schmidt, M. W. (2015). Crystal structure, high-pressure, and high-temperature behavior of carbonates in the $K_2Mg(CO_3)_2$–$Na_2Mg(CO_3)_2$ join. *American Mineralogist*, *100*(11–12), 2458–2467. https://doi.org/10/f72dmt

Grassi, D., & Schmidt, M. W. (2011). The melting of carbonated pelites from 70 to 700 km depth. *Journal of Petrology*, *52*(4), 765–789. https://doi.org/10/bf4k6d

Guo, X., Lange, R. A., & Ai, Y. (2013). The density and compressibility of CaO-FeO-SiO2 liquids at one bar: Evidence for four-coordinated Fe^{2+} in the $CaFeO_2$ component. *Geochimica et Cosmochimica Acta*, *120*, 206–219. https://doi.org/10.1016/j.gca.2013.06.007

Haar, L. (1984). *Nbs/Nrc Steam Tables*. CRC Press.

Hallstedt, B., Dupin, N., Hillert, M., Höglund, L., Lukas, H. L., Schuster, J. C., & Solak, N. (2007). Thermodynamic models for crystalline phases. Composition dependent models for volume, bulk modulus and thermal expansion. *Calphad*, *31*(1), 28–37. https://doi.org/10.1016/j.calphad.2006.02.008

Harder, H., & Christensen, U. R. (1996). A one-plume model of Martian mantle convection. *Nature*, *380*(6574), 507–509. https://doi.org/10.1038/380507a0

Harlow, G. E., & Davies, R. (2004). Status report on stability of K-rich phases at mantle conditions. *Lithos*, *77*(1–4), 647–653. https://doi.org/10.1016/j.lithos.2004.04.010

Herd, C. D. K., Borg, L. E., Jones, J. H., & Papike, J. J. (2002). Oxygen fugacity and geochemical variations in the Martian basalts: Implications for Martian basalt petrogenesis and the oxidation state of the upper mantle of Mars. *Geochimica et Cosmochimica Acta*, *66*(11), 2025–2036. https://doi.org/10/bnwbg5

Hernandez, J. -A., Morard, G., Guarguaglini, M., Alonso-Mori, R., Benuzzi-Mounaix, A., Bolis, R., Fiquet, G., Galtier, E., Gleason, A. E., Glenzer, S., Guyot, F., Ko, B., Lee, H. J., Mao, W. L., Nagler, B., Ozaki, N., Schuster, A. K., Shim, S. H., Vinci, T., & Ravasio, A. (2020). Direct observation of shock-induced disordering of enstatite below the melting temperature. *Geophysical Research Letters*, *47*(15), 1–9. https://doi.org/10.1029/2020GL088887

Hier-Majumder, S., & Courtier, A. (2011). Seismic signature of small melt fraction atop the transition zone. *Earth and Planetary Science Letters*, *308*(3–4), 334–342. https://doi.org/10.1016/j.epsl.2011.05.055

Hier-Majumder, S., Keel, E. B., & Courtier, A. M. (2014). The influence of temperature, bulk composition, and melting on the seismic signature of the low-velocity layer

above the transition zone. *Journal of Geophysical Research: Solid Earth*, *119*(2), 971–983. https://doi.org/10/gjvhv2

Hier-Majumder, S., & Tauzin, B. (2017). Pervasive upper mantle melting beneath the western US. *Earth and Planetary Science Letters*, *463*, 25–35. https://doi.org/10/f9t9p7

Hirschmann, M. M., Withers, A. C., & Aubaud, C. (2006). Petrologic structure of a hydrous 410 km discontinuity. *Earth's Deep Water Cycle*, *168*, 277–287.

Hirth, G., & Kohlstedt, D. L. (1996). Water in the oceanic upper mantle: Implications for rheology, melt extraction and the evolution of the lithosphere. *Earth and Planetary Science Letters*, *144*(1), 93–108. https://doi.org/10.1016/0012-821X(96)00154-9

Holland, K. G., & Ahrens, T. J. (1997). Melting of $(Mg,Fe)_2SiO_4$ at the core-mantle boundary of the earth. *Science*, *275*(5306), 1623–1625. https://doi.org/10.1126/science.275.5306.1623

Hou, B. (2022). Phase transitions and compressibility of alkali-bearing double carbonates at high pressures: A first-principles calculations study. *Physics and Chemistry of Minerals*, 12. https://doi.org/10.1007/s00269-022-01210-9

Houser, C. (2016). Global seismic data reveal little water in the mantle transition zone. *Earth and Planetary Science Letters*, *448*, 94–101.

Huang, W. L., & Wyllie, P. J. (1981). Phase relationships of S-type granite with H2O to 35 kbar: Muscovite granite from Harney Peak, South Dakota. *Journal of Geophysical Research: Solid Earth*, *86*(B11), 10515–10529. https://doi.org/10.1029/JB086iB11p10515

Jackson, I., & Ahrens, T. J. (1979). Shock wave compression of single-crystal forsterite. *Journal of Geophysical Research*, *84*(B6), 3039. https://doi.org/10.1029/JB084iB06p03039

Jakosky, B. M., & Phillips, R. J. (2001). Mars' volatile and climate history. *Nature*, *412*(6843), 237–244. https://doi.org/10.1038/35084184

Jasbinsek, J., & Dueker, K. (2007). Ubiquitous low-velocity layer atop the 410-km discontinuity in the northern Rocky Mountains. *Geochemistry, Geophysics, Geosystems*, *8*(10). https://doi.org/10.1029/2007GC001661

Jasbinsek, J. J., Dueker, K. G., & Hansen, S. M. (2010). Characterizing the 410 km discontinuity low-velocity layer beneath the LA RISTRA array in the North

American Southwest. *Geochemistry, Geophysics, Geosystems*, *11*(3). https://doi.org/10.1029/2009GC002836

Jeanloz, R. (1981). Finite-strain equation of state for high-pressure phases. *Geophysical Research Letters*, *8*(12), 1219–1222. https://doi.org/10.1029/GL008i012p01219

Jeanloz, R. (1989). Shock wave equation of state and finite strain theory. *Journal of Geophysical Research*, *94*(B5), 5873–5886. https://doi.org/10.1029/JB094iB05p05873

Jing, Z., & ichiro Karato, S. (2012). Effect of H_2O on the density of silicate melts at high pressures: Static experiments and the application of a modified hard-sphere model of equation of state. *Geochimica et Cosmochimica Acta*, *85*, 357–372. https://doi.org/10.1016/j.gca.2012.03.001

Jing, Z., & Karato, S. (2008). Compositional effect on the pressure derivatives of bulk modulus of silicate melts. *Earth and Planetary Science Letters*, *272*(1), 429–436. https://doi.org/10.1016/j.epsl.2008.05.013

Johnson, D., Smith, J. W., & Robb, W. A. (1974). Thermal characteristics of shortite. (Vol. 7862). US Department of the Interior, Bureau of Mines.

Karki, B. B., Ghosh, D. B., & Karato, S. (2021). Behavior and properties of water in silicate melts under deep mantle conditions. *Scientific Reports*, *11*(1), 10588. https://doi.org/10/gkzg5j

Katayama, I., Nakashima, S., & Yurimoto, H. (2006). Water content in natural eclogite and implication for water transport into the deep upper mantle. *Lithos*, *86*(3–4), 245–259. https://doi.org/10/frh7zw

Kawamoto, T., & Holloway, J. (1997). Melting temperature and partial melt chemistry of H_2O-saturated mantle peridotite to 11 gigapascals. *Science*, *276*(5310), 240–243. https://doi.org/10.1126/science.276.5310.240

Kennedy, G. C., Wasserburg, G. J., Heard, H. C., & Newton, R. C. (1962). The upper three-phase region in the system SiO_2-H_2O. *American Journal of Science*, *260*(7), 501–521. https://doi.org/10.2475/ajs.260.7.501

Kennett, B. L. N., & Engdahl, E. R. (1991). Traveltimes for global earthquake location and phase identification. *Geophysical Journal International*, *105*(2), 429–465. https://doi.org/10/b8jr4b

Khan, A., & Connolly, J. a. D. (2008). Constraining the composition and thermal state of Mars from inversion of geophysical data. *Journal of Geophysical Research: Planets*, *113*(E7). https://doi.org/10.1029/2007JE002996

Khan, A., Liebske, C., Rozel, A., Rivoldini, A., Nimmo, F., Connolly, J. a. D., Plesa, A.-C., & Giardini, D. (2018). A geophysical perspective on the bulk composition of Mars. *Journal of Geophysical Research: Planets*, *123*(2), 575–611. https://doi.org/10.1002/2017JE005371

Kiefer, W. S. (2003). Melting in the martian mantle: Shergottite formation and implications for present-day mantle convection on Mars. *Meteoritics & Planetary Science*, *38*(12), 1815–1832. https://doi.org/10.1111/j.1945-5100.2003.tb00017.x

Kraft, S., Knittle, E., & Williams, Q. (1991). Carbonate stability in the Earth's mantle: A vibrational spectroscopic study of aragonite and dolomite at high pressures and temperatures. *Journal of Geophysical Research*, *96*(B11), 17997. https://doi.org/10.1029/91JB01749

Kress, V. C., & Carmichael, I. S. E. (1991). The compressibility of silicate liquids containing Fe_2O_3 and the effect of composition, temperature, oxygen fugacity and pressure on their redox states. *Contributions to Mineralogy and Petrology*, *108*(1–2), 82–92. https://doi.org/10.1007/BF00307328

Kresse, G., & Furthmüller, J. (1996). Efficient iterative schemes for *ab initio* total-energy calculations using a plane-wave basis set. *Physical Review B*, *54*(16), 11169–11186. https://doi.org/10.1103/PhysRevB.54.11169

Kubo, A., & Akaogi, M. (2000). Post-garnet transitions in the system $Mg_4Si_4O_{12}$–$Mg_3Al_2Si_3O_{12}$ up to 28 GPa: Phase relations of garnet, ilmenite and perovskite. *Physics of the Earth and Planetary Interiors*, *121*(1), 85–102. https://doi.org/10.1016/S0031-9201(00)00162-X

Labrosse, S. (2002). Hotspots, mantle plumes and core heat loss. *Earth and Planetary Science Letters*, *199*(1–2), 147–156. https://doi.org/10.1016/S0012-821X(02)00537-X

Labrosse, S., Hernlund, J. W., & Coltice, N. (2007). A crystallizing dense magma ocean at the base of the Earth's mantle. *Nature*, *450*(7171), 866–869. https://doi.org/10.1038/nature06355

Lambert, I. B., & Wyllie, P. J. (1972). Melting of gabbro (quartz eclogite) with excess water to 35 kilobars, with geological applications. *The Journal of Geology*, *80*(6), 693–708. https://doi.org/10.1086/627795

Lange, R. A., & Carmichael, I. S. E. (1987). Densities of Na_2O-K_2O-CaO-MgO-FeO-Fe_2O_3-Al_2O_3-TiO_2-SiO_2 liquids: New measurements and derived partial molar properties. *Geochimica et Cosmochimica Acta*, *51*(11), 2931–2946. https://doi.org/10.1016/0016-7037(87)90368-1

Larsen, C. F., & Williams, Q. (1998). Overtone spectra and hydrogen potential of H_2O at high pressure. *Physical Review B*, *58*(13), 8306–8312. https://doi.org/10.1103/PhysRevB.58.8306

Lay, T., Garnero, E. J., & Williams, Q. (2004). Partial melting in a thermo-chemical boundary layer at the base of the mantle. *Physics of the Earth and Planetary Interiors*, *146*(3–4), 441–467. https://doi.org/10.1016/j.pepi.2004.04.004

Lay, T., Hernlund, J., & Buffett, B. A. (2008). Core-mantle boundary heat flow. *Nature Geoscience*, *1*(1), 25–32. https://doi.org/10.1038/ngeo.2007.44

Leahy, G. M., & Bercovici, D. (2007). On the dynamics of a hydrous melt layer above the transition zone. *Journal of Geophysical Research*, *112*(B7), B07401. https://doi.org/10.1029/2006JB004631

Li, G., Bai, L., Zhou, Y., Wang, X., & Cui, Q. (2017). Velocity structure of the mantle transition zone beneath the southeastern margin of the Tibetan Plateau. *Tectonophysics*, *721*, 349–360. https://doi.org/10.1016/j.tecto.2017.08.009

Li, G. H., Sui, Y., & Zhou, Y. Z. (2014). Low-velocity layer atop the mantle transition zone in the lower Yangtze Craton from P waveform triplication. *Acta Geophysica Sinica*, *57*(7), 2362–2371. https://doi.org/10.1002/cjg2.20122

Li, G., Li, Y. E., Zhang, H., Bai, L., Ding, L., Li, W., Cui, Q., & Zhou, Y. (2019). Detection of a thick and weak low-velocity layer atop the mantle transition zone beneath the northeastern South China sea from triplicated P-wave waveform modeling. *Bulletin of the Seismological Society of America*, *109*(4), 1181–1193. https://doi.org/10.1785/0120180318

Likhacheva, A. Y., Miloš, S., Romanenko, A. V., Goryainov, S. V., Semerikova, A. I., Rashchenko, S. V., Miletich, R., & Shatsky, A. (2024). High-pressure behavior and stability of synthetic buetschliite $K_2Ca(CO_3)_2$ up to 19 GPa and 300°C. *Journal of Raman Spectroscopy*, *55*(4), 517. https://doi.org/10.1002/jrs.6654

Lillis, R. J., Frey, H. V., & Manga, M. (2008). Rapid decrease in Martian crustal magnetization in the Noachian era: Implications for the dynamo and climate of early Mars. *Geophysical Research Letters*, *35*(14). https://doi.org/10.1029/2008GL034338

Litasov, K., & Ohtani, E. (2010). The solidus of carbonated eclogite in the system CaO–Al_2O_3–MgO–SiO_2–Na_2O–CO_2 to 32 GPa and carbonatite liquid in the deep mantle. *Earth and Planetary Science Letters*, *295*(1–2), 115–126. https://doi.org/10/ctmt42

Liu, X., Matsukage, K. N., Li, Y., Takahashi, E., Suzuki, T., & Xiong, X. (2018). Aqueous fluid connectivity in subducting oceanic crust at the mantle transition zone conditions. *Journal of Geophysical Research: Solid Earth*, *123*(8), 6562–6573. https://doi.org/10.1029/2018JB015973

Logvinova, A. M., Shatskiy, A., Wirth, R., Tomilenko, A. A., Ugap'eva, S. S., & Sobolev, N. V. (2019). Carbonatite melt in type Ia gem diamond. *Lithos*, *342–343*, 463–467. https://doi.org/10/gjxnx6

Lucazeau, G. (2003). Effect of pressure and temperature on Raman spectra of solids: Anharmonicity. *Journal of Raman Spectroscopy*, *34*(7–8), 478–496. https://doi.org/10.1002/jrs.1027

Luo, S. N., Akins, J. A., Ahrens, T. J., & Asimow, P. D. (2004). Shock-compressed $MgSiO_3$ glass, enstatite, olivine, and quartz: Optical emission, temperatures, and melting. *Journal of Geophysical Research: Solid Earth*, *109*(5), 1–14. https://doi.org/10.1029/2003JB002860

Lv, X., Wei, L., Wang, X., Xu, J., Yu, H., Hu, Y., Zhang, H., Zhang, C., Wang, J., & Li, Q. (2018). Crystal growth, electronic structure and optical properties of $Sr_2Mg(BO_3)_2$. *Journal of Solid State Chemistry*, *258*, 283–288. https://doi.org/10.1016/j.jssc.2017.10.032

Lyzenga, G. A., & Ahrens, T. J. (1980). Shock temperature measurements in Mg_2SiO_4 and SiO_2 at high pressures. *Geophysical Research Letters*, *7*(2), 141–144. https://doi.org/10.1029/GL007i002p00141

Malfait, W. J., Seifert, R., Petitgirard, S., Mezouar, M., & Sanchez-Valle, C. (2014). The density of andesitic melts and the compressibility of dissolved water in silicate melts at crustal and upper mantle conditions. *Earth and Planetary Science Letters*, *393*, 31–38. https://doi.org/10.1016/j.epsl.2014.02.042

Malfait, W. J., Seifert, R., Petitgirard, S., Perrillat, J.-P., Mezouar, M., Ota, T., Nakamura, E., Lerch, P., & Sanchez-Valle, C. (2014). Supervolcano eruptions driven by melt buoyancy in large silicic magma chambers. *Nature Geoscience*, *7*(2), 122–125. https://doi.org/10.1038/ngeo2042

Marinova, M. M., Aharonson, O., & Asphaug, E. (2008). Mega-impact formation of the Mars hemispheric dichotomy. *Nature*, *453*(7199), 1216–1219. https://doi.org/10.1038/nature07070

Matsukage, K. N., Hashimoto, M., & Nishihara, Y. (2017). Morphological stability of hydrous liquid droplets at grain boundaries of eclogite minerals in the deep upper mantle. *Journal of Mineralogical and Petrological Sciences*, *112*(6), 346–358. https://doi.org/10/gctjt8

Matsukage, K. N., Jing, Z., & Karato, S. (2005). Density of hydrous silicate melt at the conditions of Earth's deep upper mantle. *Nature*, *438*(7067), 488–491. https://doi.org/10.1038/nature04241

Mckenzie, D. P., Roberts, J. M., & Weiss, N. O. (1974). Convection in the earth's mantle: Towards a numerical simulation. *Journal of Fluid Mechanics*, *62*(3), 465–538. https://doi.org/10.1017/S0022112074000784

McKie, D. (1990). Subsolidus phase relations in the system $K_2Ca(CO_3)_2$-$Na_2Mg(CO_3)_2$ at 1 kbar; the fairchilditess-buetschliite-eitelite eutectoid. *American Mineralogist*, *75*, 1147–1150.

Mei, S., Bai, W., Hiraga, T., & Kohlstedt, D. L. (2002). Influence of melt on the creep behavior of olivine-basalt aggregates under hydrous conditions. *Earth and Planetary Science Letters*, *201*(3–4), 491–507.

Meltzer, A., & Kessel, R. (2023). The metasomatism of sub-cratonic peridotites by a slab-derived fluid – Implications for cratons' evolution. *Geochimica et Cosmochimica Acta*, *350*, 28–45. https://doi.org/10.1016/j.gca.2023.03.034

Mernagh, T. P., Kamenetsky, V. S., & Kamenetsky, M. B. (2011). A Raman microprobe study of melt inclusions in kimberlites from Siberia, Canada, SW Greenland and South Africa. *Spectrochimica Acta Part A: Molecular and Biomolecular Spectroscopy*, *80*(1), 82–87. https://doi.org/10.1016/j.saa.2011.01.034

Mibe, K., Chou, I. M., & Bassett, W. A. (2008). In situ Raman spectroscopic investigation of the structure of subduction-zone fluids. *Journal of Geophysical Research: Solid Earth*, *113*(4), 1–8. https://doi.org/10.1029/2007JB005179

Mibe, K., Kawamoto, T., Matsukage, K. N., Fei, Y., & Ono, S. (2011). Slab melting versus slab dehydration in subduction-zone magmatism. *Proceedings of the National Academy of Sciences*, *108*(20), 8177–8182. https://doi.org/10.1073/pnas.1010968108

Mibe, K., Yoshino, T., Ono, S., Yasuda, A., & Fujii, T. (2003). Connectivity of aqueous fluid in eclogite and its implications for fluid migration in the Earth's interior. *Journal of Geophysical Research: Solid Earth*, *108*(B6). https://doi.org/10/cdmvwd

Militzer, B. (2013). Ab initio investigation of a possible liquid-liquid phase transition in $MgSiO_3$ at megabar pressures. *High Energy Density Physics*, *9*(1), 152–157. https://doi.org/10.1016/j.hedp.2012.11.006

Millot, M., Zhang, S., Fratanduono, D. E., Coppari, F., Hamel, S., Militzer, B., Simonova, D., Shcheka, S., Dubrovinskaia, N., Dubrovinsky, L., & Eggert, J. H. (2020). Recreating giants impacts in the laboratory: Shock compression of bridgmanite to 14 Mbar. *Geophysical Research Letters*, *47*(4), 1–8. https://doi.org/10.1029/2019GL085476

Milton, C., & Axelrod, J. (1947). Fused wood-ash stones: Fairchildite (n. Sp.) $K_2CO_3 \cdot CaCO_3$, buetschliite (n. Sp.) $3K_2CO_3 \cdot 2CaCO_3 \cdot 6H_2O$ and calcite, $CaCO_3$, their essential components. *American Mineralogist: Journal of Earth and Planetary Materials*, *32*(11–12), 607–624.

Mitchell, A. C., & Nellis, W. J. (1979). Water Hugoniot measurements in the range 30 to 220 GPa. In *High-Pressure Science and Technology* (pp. 428–434). Springer US. https://doi.org/10.1007/978-1-4684-7470-1_53

Mookherjee, M., Stixrude, L., & Karki, B. (2008). Hydrous silicate melt at high pressure. *Nature*, *452*(7190), 983–986. https://doi.org/10.1038/nature06918

Mosenfelder, J. L., Asimow, P. D., & Ahrens, T. J. (2007). Thermodynamic properties of Mg_2SiO_4 liquid at ultra-high pressures from shock measurements to 200 GPa on forsterite and wadsleyite. *J. Geophys. Res*, *112*, 6208. https://doi.org/10.1029/2006JB004364

Mosenfelder, J. L., Asimow, P. D., Frost, D. J., Rubie, D. C., & Ahrens, T. J. (2009). The $MgSiO_3$ system at high pressure: Thermodynamic properties of perovskite, postperovskite, and melt from global inversion of shock and static compression data. *J. Geophys. Res*, *114*, 1203. https://doi.org/10.1029/2008JB005900

Mrose, M. E., Rose, H. J., & Marinenko, J. W. (1966). Synthesis and properties of fairchildite and buetschliite: Their relation to wood-ash stone formation. *Program of the Geol Soc. Am. Meeting, San Francisco*, *146*.

Navrotsky, A., Putnam, R. L., Winbo, C., & Rosen, E. (1997). Thermochemistry of double carbonates in the K_2CO_3-$CaCO_3$ system. *American Mineralogist*, *82*(5–6), 546–548. https://doi.org/10.2138/am-1997-5-614

Nimmo, F., & Stevenson, D. J. (2000). Influence of early plate tectonics on the thermal evolution and magnetic field of Mars. *Journal of Geophysical Research: Planets*, *105*(E5), 11969–11979. https://doi.org/10.1029/1999JE001216

Nolet, G., & Zielhuis, A. (1994). Low S velocities under the Tornquist-Teisseyre zone: Evidence for water injection into the transition zone by subduction. *Journal of Geophysical Research: Solid Earth*, *99*(B8), 15813–15820. https://doi.org/10.1029/94JB00083

Nomura, R., Hirose, K., Uesugi, K., Ohishi, Y., Tsuchiyama, A., Miyake, A., & Ueno, Y. (2014). Low core-mantle boundary temperature inferred from the solidus of pyrolite. *Science*, *343*(6170), 522–525. https://doi.org/10.1126/science.1248186

Ochs III., F. A., & Lange, R. A. (1997). The partial molar volume, thermal expansivity, and compressibility of H_2O in $NaAlSi_3O_8$ liquid: New measurements and an internally consistent model. *Contributions to Mineralogy and Petrology*, *129*(2–3), 155–165. https://doi.org/10.1007/s004100050329

Ochs III, F. A., & Lange, R. A. (1999). The density of hydrous magmatic liquids. *Science*, *283*(5406), 1314–1317. https://doi.org/10.1126/science.283.5406.1314

Ohtani, E., Kagawa, N., & Fujino, K. (1991). Stability of majorite $(Mg,Fe)SiO_3$ at high pressures and 1800°C. *Earth and Planetary Science Letters*, *102*(2), 158–166. https://doi.org/10.1016/0012-821X(91)90005-3

Ohtani, E., Suzuki, A., & Kato, T. (1993). Flotation of olivine in the peridotite melt at high pressure. *Proceedings of the Japan Academy. Ser. B: Physical and Biological Sciences*, *69*(2), 23–28. https://doi.org/10.2183/pjab.69.23

Ohuchi, T., Nishihara, Y., Kawazoe, T., Spengler, D., Shiraishi, R., Suzuki, A., Kikegawa, T., & Ohtani, E. (2012). Superplasticity in hydrous melt-bearing dunite: Implications for shear localization in Earth's upper mantle. *Earth and Planetary Science Letters*, *335–336*, 59–71. https://doi.org/10/gbbfwq

Ono, S. (1998). Stability limits of hydrous minerals in sediment and mid-ocean ridge basalt compositions: Implications for water transport in subduction zones. *Journal of Geophysical Research: Solid Earth*, *103*(B8), 18253–18267. https://doi.org/10/d6t644

Pabst, A. (1974). Synthesis, properties, and structure of $K_2Ca(CO_3)_2$, buetschliite. *American Mineralogist*, *59*(3–4), 6.

Paillat, O., Elphick, S. C., & Brown, W. L. (1992). The solubility of water in $NaAlSi_3O_8$ melts: A re-examination of Ab-H_2O phase relationships and critical behaviour at high pressures. *Contributions to Mineralogy and Petrology*, *112*(4), 490–500. https://doi.org/10.1007/BF00310780

Paine, J. B. (1997). Use of eitelite to reduce sidestream smoke (Patent 5699811).

Pertlik, F. (1981). Structural investigations of synthetic fairchildite, $K_2Ca(CO_3)_2$. *Zeitschrift Für Kristallographie-Crystalline Materials*, *157*(3–4), 199–205. https://doi.org/10.1524/zkri.1981.157.3-4.199

Peterson, V. K. (2005). Lattice parameter measurement using Le Bail versus structural (Rietveld) refinement: A caution for complex, low symmetry systems. *Powder Diffraction*, *20*(1), 14–17. https://doi.org/10.1154/1.1810156

Pitzer, K. S., & Sterner, S. M. (1994). Equations of state valid continuously from zero to extreme pressures for H_2O and CO_2. *The Journal of Chemical Physics*, *101*(4), 3111–3116. https://doi.org/10/dr45c9

Podborodnikov, I. V., Shatskiy, A., Arefiev, A. V., Rashchenko, S. V., Chanyshev, A. D., & Litasov, K. D. (2018). The system Na_2CO_3–$CaCO_3$ at 3 GPa. *Physics and Chemistry of Minerals*, *45*(8), 773–787. https://doi.org/10.1007/s00269-018-0961-2

Rapp, J. F., & Draper, D. S. (2018). Fractional crystallization of the lunar magma ocean: Updating the dominant paradigm. *Meteoritics & Planetary Science*, *53*(7), 1432–1455. https://doi.org/10.1111/maps.13086

Rashchenko, S. V., Goryainov, S. V., Romanenko, A. V., Golovin, A. V., Korsakov, A. V., Moine, B. N., & Mikhno, A. O. (2017). High-pressure Raman study of nyerereite from Oldoinyo Lengai. *Journal of Raman Spectroscopy*, *48*(11), 1438–1442. https://doi.org/10.1002/jrs.5152

Reeder, R., & Markgraf, S. (1986). High-temperature crystal chemistry of dolomite. *American Mineralogist*, *71*, 795–804.

Reese, C. C., & Solomatov, V. S. (2006). Fluid dynamics of local martian magma oceans. *Icarus*, *184*, 102–120. https://doi.org/10/dz4x55

Revenaugh, J., & Sipkin, S. A. (1994). Seismic evidence for silicate melt atop the 410-km mantle discontinuity. *Nature*, *369*(6480), 474–476. https://doi.org/10.1038/369474a0

Rice, M. H., & Walsh, J. M. (1957). Equation of state of water to 250 kilobars. *The Journal of Chemical Physics*, *26*(4), 824–830. https://doi.org/10.1063/1.1743415

Righter, K., Danielson, L. R., Martin, A. M., Newville, M., & Choi, Y. (2010, July 26). Iron redox systematics of shergottites and Martian magmas. Meteoritical Society meeting, New York, NY. https://ntrs.nasa.gov/citations/20120007400

Righter, K., Yang, H., Costin, G., & Downs, R. T. (2008). Oxygen fugacity in the Martian mantle controlled by carbon: New constraints from the nakhlite MIL 03346.

Meteoritics & Planetary Science, *43*(10), 1709–1723. https://doi.org/10.1111/j.1945-5100.2008.tb00638.x

Ritter, X., Sanchez-Valle, C., Sator, N., Desmaele, E., Guignot, N., King, A., Kupenko, I., Berndt, J., & Guillot, B. (2020). Density of hydrous carbonate melts under pressure, compressibility of volatiles and implications for carbonate melt mobility in the upper mantle. *Earth and Planetary Science Letters*, *533*, 116043. https://doi.org/10.1016/j.epsl.2019.116043

Rivers, M. L., & Carmichael, I. S. E. (1987). Ultrasonic studies of silicate melts. *Journal of Geophysical Research*, *92*(B9), 9247. https://doi.org/10.1029/JB092iB09p09247

Rivoldini, A., Van Hoolst, T., Verhoeven, O., Mocquet, A., & Dehant, V. (2011). Geodesy constraints on the interior structure and composition of Mars. *ICARUS*, *213*(2), 451–472. https://doi.org/10/ct6mzj

Roberts, J. H., Lillis, R. J., & Manga, M. (2009). Giant impacts on early Mars and the cessation of the Martian dynamo. *Journal of Geophysical Research: Planets*, *114*(E4). https://doi.org/10.1029/2008JE003287

Root, S., Townsend, J. P., Davies, E., Lemke, R. W., Bliss, D. E., Fratanduono, D. E., Kraus, R. G., Millot, M., Spaulding, D. K., Shulenburger, L., Stewart, S. T., & Jacobsen, S. B. (2018). The principal Hugoniot of forsterite to 950 GPa. *Geophysical Research Letters*, *45*(9), 3865–3872. https://doi.org/10.1029/2017GL076931

Rost, S., Garnero, E. J., & Williams, Q. (2006). Fine-scale ultralow-velocity zone structure from high-frequency seismic array data. *Journal of Geophysical Research: Solid Earth*, *111*(B9). https://doi.org/10.1029/2005JB004088

Rost, S., Garnero, E. J., Williams, Q., & Manga, M. (2005). Seismological constraints on a possible plume root at the core–mantle boundary. *Nature*, *435*(7042), 666–669. https://doi.org/10.1038/nature03620

Ruedas, T., & Breuer, D. (2019). Dynamical effects of multiple impacts: Large impacts on a Mars-like planet. *Physics of the Earth and Planetary Interiors*, *287*, 76–92. https://doi.org/10.1016/j.pepi.2019.01.003

Sakamaki, T. (2017). Density of hydrous magma. *Chemical Geology*, *475*, 135–139. https://doi.org/10.1016/j.chemgeo.2017.11.012

Sakamaki, T., Ohtani, E., Urakawa, S., Suzuki, A., & Katayama, Y. (2009). Measurement of hydrous peridotite magma density at high pressure using the X-ray absorption method. *Earth and Planetary Science Letters*, *287*(3–4), 293–297. https://doi.org/10.1016/j.epsl.2009.07.030

Sakamaki, T., Ohtani, E., Urakawa, S., Suzuki, A., & Katayama, Y. (2010). Density of dry peridotite magma at high pressure using an X-ray absorption method. *American Mineralogist*, *95*(1), 144–147. https://doi.org/10/dpwn7n

Sakamaki, T., Suzuki, A., & Ohtani, E. (2006). Stability of hydrous melt at the base of the Earth's upper mantle. *Nature*, *439*(7073), 192–194. https://doi.org/10.1038/nature04352

Samuel, H., Lognonné, P., Panning, M., & Lainey, V. (2019). The rheology and thermal history of Mars revealed by the orbital evolution of Phobos. *Nature*, *569*(7757), 523–527. https://doi.org/10.1038/s41586-019-1202-7

Sandu, C., & Kiefer, W. S. (2012). Degassing history of Mars and the lifespan of its magnetic dynamo. *Geophysical Research Letters*, *39*(3). https://doi.org/10.1029/2011GL050225

Santamaria-Perez, D., Pavic, L., Chuliá-Jordán, R., Ruiz-Fuertes, J., Popescu, C., & Otero-de-la-Roza, A. (2023). Phase stability of stress-sensitive Ag_2CO_3 silver carbonate at high pressures and temperatures. *Solid State Sciences*, *135*, 107068. https://doi.org/10.1016/j.solidstatesciences.2022.107068

Schaeffer, A. J., & Bostock, M. G. (2010). A low-velocity zone atop the transition zone in northwestern Canada. *Journal of Geophysical Research*, *115*(B6), B06302. https://doi.org/10.1029/2009JB006856

Schmandt, B., Dueker, K. G., Hansen, S. M., Jasbinsek, J. J., & Zhang, Z. (2011). A sporadic low-velocity layer atop the western U.S. mantle transition zone and short-wavelength variations in transition zone discontinuities. *Geochemistry, Geophysics, Geosystems*, *12*(8). https://doi.org/10.1029/2011GC003668

Seifert, R., Malfait, W. J., Petitgirard, S., & Sanchez-Valle, C. (2013). Density of phonolitic magmas and time scales of crystal fractionation in magma chambers. *Earth and Planetary Science Letters*, *381*, 12–20. https://doi.org/10.1016/j.epsl.2013.08.039

Sekhar, P., & King, S. D. (2014). 3D spherical models of Martian mantle convection constrained by melting history. *Earth and Planetary Science Letters*, *388*, 27–37. https://doi.org/10.1016/j.epsl.2013.11.047

Sekine, T., Meng, C., Zhu, W., & He, H. (2012). Direct evidence for decomposition of antigorite under shock loading. *Journal of Geophysical Research: Solid Earth*, *117*(3), 1–8. https://doi.org/10.1029/2011JB008439

Sekine, T., Ozaki, N., Miyanishi, K., Asaumi, Y., Kimura, T., Albertazzi, B., Sato, Y., Sakawa, Y., Sano, T., Sugita, S., Matsui, T., & Kodama, R. (2016). Shock

compression response of forsterite above 250 GPa. *Science Advances*, *2*(8), e1600157. https://doi.org/10.1126/sciadv.1600157

Shannon, R. D. (1976). Revised effective ionic radii and systematic studies of interatomic distances in halides and chalcogenides. *Acta Crystallographica Section A*, *32*(5), 751–767. https://doi.org/10.1107/S0567739476001551

Shatskiy, A., Borzdov, Y. M., Litasov, K. D., Sharygin, I. S., Palyanov, Y. N., & Ohtani, E. (2015). Phase relationships in the system K_2CO_3-$CaCO_3$ at 6 GPa and 900-1450°C. *American Mineralogist*, *100*(1), 223–232. https://doi.org/10.2138/am-2015-5001

Shatskiy, A., Sharygin, I. S., Litasov, K. D., Borzdov, Y. M., Palyanov, Y. N., & Ohtani, E. (2013). New experimental data on phase relations for the system Na_2CO_3-$CaCO_3$ at 6 GPa and 900-1400°C. *American Mineralogist*, *98*(11–12), 2164–2171. https://doi.org/10.2138/am.2013.4436

Sheldrick, G. M. (2008). A short history of SHELX. *Acta Crystallographica Section A*.

Shen, G., Wang, Y., Dewaele, A., Wu, C., Fratanduono, D. E., Eggert, J., Klotz, S., Dziubek, K. F., Loubeyre, P., Fat'yanov, O. V., Asimow, P. D., Mashimo, T., Wentzcovitch, R. M. M., & other members of the IPPS task group. (2020). Toward an international practical pressure scale: A proposal for an IPPS ruby gauge (IPPS-Ruby2020). *High Pressure Research*, *40*(3), 299–314. https://doi.org/10/gmhp2z

Shimizu, H. (1985). Pressure-tuning resonance between the vibron and the libron in CH_2Br_2 and CD_2Br_2 molecular solids. *Physical Review B*, *32*(6), 4120–4125. https://doi.org/10/bd8z5j

Solomatov, V. (2007). Magma oceans and primordial mantle differentiation. *Evolution of the Earth*, *9*, 91–119.

Solomatov, V. S. (2000). Fluid dynamics of a terrestrial magma ocean. In R. M. Canup & K. Righter (Eds.), Origin of the Earth and Moon (pp. 323–338). University of Arizona Press; JSTOR. https://doi.org/10.2307/j.ctv1v7zdrp.23

Solomatova, N. V., & Caracas, R. (2021). Buoyancy and structure of volatile-rich silicate melts. *Journal of Geophysical Research: Solid Earth*, *126*(2). https://doi.org/10/gkzg8f

Song, T.-R. A., Helmberger, Don. V., & Grand, S. P. (2004). Low-velocity zone atop the 410-km seismic discontinuity in the northwestern United States. *Nature*, *427*(6974), 530–533. https://doi.org/10.1038/nature02231

Stanley, S., & Glatzmaier, G. A. (2009). Dynamo models for planets other than Earth. In Planetary Magnetism (pp. 617-649). Springer, New York, NY.

Stixrude, L. (2001). First principles theory of mantle and core phases. In *Reviews in Mineralogy and Geochemistry* (Vol. 42, pp. 318–343). Mineralogical Society of America. https://doi.org/10.2138/rmg.2001.42.9

Stixrude, L., & Karki, B. (2005). Structure and freezing of $MgSiO_3$ liquid in Earth's lower mantle. *Science*, *310*(5746), 297–299. https://doi.org/10.1126/science.1116952

Stixrude, L., & Lithgow-Bertelloni, C. (2011). Thermodynamics of mantle minerals—II. Phase equilibria. *Geophysical Journal International*, *184*(3), 1180–1213. https://doi.org/10.1111/j.1365-246X.2010.04890.x

Stolper, E. (1982). The speciation of water in silicate melts. *Geochimica et Cosmochimica Acta*. https://doi.org/10.1016/0016-7037(82)90381-7

Stolper, E., Walker, D., Hager, B. H., & Hays, J. F. (1981). Melt segregation from partially molten source regions: The importance of melt density and source region size. *Journal of Geophysical Research: Solid Earth*, *86*(B7), 6261–6271. https://doi.org/10.1029/JB086iB07p06261

Suehiro, S., Ohta, K., Hirose, K., Morard, G., & Ohishi, Y. (2017). The influence of sulfur on the electrical resistivity of hcp iron: Implications for the core conductivity of Mars and Earth. *Geophysical Research Letters*, *44*(16), 8254–8259. https://doi.org/10.1002/2017GL074021

Syono, Y., Goto, T., Sato, J., & Takei, H. (1981). Shock compression measurements of single-crystal forsterite in the pressure range 15-93 GPa. *Journal of Geophysical Research: Solid Earth*, *86*(B7), 6181–6186. https://doi.org/10.1029/JB086iB07p06181

Tackley, P. J. (1998). Three-dimensional simulations of mantle convection with a thermo-chemical basal boundary layer: D''? *The Core-mantle Boundary Region*, *28*, 231–253.

Tauzin, B., Debayle, E., & Wittlinger, G. (2010). Seismic evidence for a global low-velocity layer within the Earth's upper mantle. *Nature Geoscience*, *3*(10), 718–721. https://doi.org/10.1038/ngeo969

Tian, H., Li, Y., Zhang, Q., Su, N., Sun, J., Xiao, N., Liu, Y., Zhang, J., Liu, H., & Li, Y. (2023). Pressure-dependent compressibility of $K_2X(CO_3)_2$ (X = Ca, Mg) under high pressure. *Materials Letters*, *349*, 134895. https://doi.org/10.1016/j.matlet.2023.134895

Tkachev, S. N., Manghnani, M. H., Williams, Q., & Ming, L. C. (2005). Compressibility of hydrated and anhydrous Na_2O-$2SiO_2$ liquid and also glass to 8 GPa using Brillouin scattering. *Journal of Geophysical Research*, *110*(B7), B07201. https://doi.org/10.1029/2004JB003328

Toby, B. H., & Von Dreele, R. B. (2013). GSAS-II: The genesis of a modern open-source all purpose crystallography software package. *Journal of Applied Crystallography*, *46*(2), Article 2. https://doi.org/10.1107/S0021889813003531

Tyburczy, J. A., Duffy, T. S., Ahrens, T. J., & Lange, M. A. (1991). Shock wave equation of state of serpentine to 150 GPa: Implications for the occurrence of water in the Earth's lower mantle. *Journal of Geophysical Research*, *96*(B11), 18011. https://doi.org/10.1029/91JB01573

Udry, A., Balta, J. B., & McSween Jr., H. Y. (2014). Exploring fractionation models for Martian magmas. *Journal of Geophysical Research: Planets*, *119*(1), 1–18. https://doi.org/10.1002/2013JE004445

Ueki, K., & Iwamori, H. (2016). Density and seismic velocity of hydrous melts under crustal and upper mantle conditions. *Geochemistry, Geophysics, Geosystems*, *17*(5), 1799–1814. https://doi.org/10.1002/2015GC006242

van Thienen, P., Rivoldini, A., Van Hoolst, T., & Lognonné, Ph. (2006). A top-down origin for Martian mantle plumes. *Icarus*, *185*(1), 197–210. https://doi.org/10.1016/j.icarus.2006.06.008

Vander Kaaden, K. E., & McCubbin, F. M. (2015). Exotic crust formation on Mercury: Consequences of a shallow, FeO-poor mantle. *Journal of Geophysical Research: Planets*, *120*(2), 195–209. https://doi.org/10.1002/2014JE004733

Vennari, C. E., Beavers, C. M., & Williams, Q. (2018). High-pressure/temperature behavior of the alkali/calcium carbonate shortite ($Na_2Ca_2(CO_3)_3$): Implications for carbon sequestration in Earth's transition zone. *Journal of Geophysical Research: Solid Earth*, *123*(8), 6574–6591. https://doi.org/10/gj5n83

Vennari, C. E., & Williams, Q. (2018). A novel carbon bonding environment in deep mantle high-pressure dolomite. *American Mineralogist*, *103*(1), 171–174. https://doi.org/10/gc6m2n

Vennari, C. E., & Williams, Q. (2019). High-pressure Raman and Nd^{3+} luminescence spectroscopy of bastnäsite-(REE)CO_3F. *American Mineralogist*, *104*(10), 1389–1401. https://doi.org/10.2138/am-2019-7011

Verhoeven, O., Rivoldini, A., Vacher, P., Mocquet, A., Choblet, G., Menvielle, M., Dehant, V., Van Hoolst, T., Sleewaegen, J., Barriot, J.-P., & Lognonné, P. (2005). Interior structure of terrestrial planets: Modeling Mars' mantle and its electromagnetic, geodetic, and seismic properties. *Journal of Geophysical Research: Planets*, *110*(E4). https://doi.org/10.1029/2004JE002271

Vinet, P., Ferrante, J., Rose, J. H., & Smith, J. R. (1987). Compressibility of solids. *Journal of Geophysical Research*, *92*(B9), 9319. https://doi.org/10.1029/jb092ib09p09319

Vinet, P., Ferrantef, J., Smith, J. R., & Rose, J. H. (1986). A universal equation of state for solids. *Journal of Physics C: Solid State Physics*, *19*(20), L467–L473. https://doi.org/10.1088/0022-3719/19/20/001

Vinnik, L., & Farra, V. (2007). Low S velocity atop the 410-km discontinuity and mantle plumes. *Earth and Planetary Science Letters*, *262*(3–4), 398–412. https://doi.org/10.1016/j.epsl.2007.07.051

Wadhwa, M. (2001). Redox state of Mars' upper mantle and crust from Eu anomalies in shergottite pyroxenes. *Science*, *291*(5508), 1527–1530. https://doi.org/10.1126/science.1057594

Walsh, J. B. (1969). New analysis of attenuation in partially melted rock. *Journal of Geophysical Research*, *74*(17), 4333–4337. https://doi.org/10/b2wpw2

Walsh, J. M., & Christian, R. H. (1955). Equation of state of metals from shock wave measurements. *Physical Review*, *97*(6), 1544–1556. https://doi.org/10.1103/PhysRev.97.1544

Wang, J., Takahashi, E., Xiong, X., Chen, L., Li, L., Suzuki, T., & Walter, M. J. (2020). The water-saturated solidus and second critical endpoint of peridotite: Implications for magma genesis within the mantle wedge. *Journal of Geophysical Research: Solid Earth*, 0–3. https://doi.org/10.1029/2020JB019452

Wang, M., Liu, Q., Nie, S., Li, B., Wu, Y., Gao, J., Wei, X., & Wu, X. (2015). High-pressure phase transitions and compressibilities of aragonite-structure carbonates: $SrCO_3$ and $BaCO_3$. *Physics and Chemistry of Minerals*, *42*, 517–527. https://doi.org/10.1007/s00269-015-0740-2

Wang, W., Xu, Y., Sun, D., Ni, S., Wentzcovitch, R., & Wu, Z. (2020). Velocity and density characteristics of subducted oceanic crust and the origin of lower-mantle heterogeneities. *Nature Communications*, *11*(1), 1–8. https://doi.org/10.1038/s41467-019-13720-2

Wang, X., Ye, Y., Wu, X., Smyth, J. R., Yang, Y., Zhang, Z., & Wang, Z. (2019). High-temperature Raman and FTIR study of aragonite-group carbonates. *Physics and Chemistry of Minerals*, *46*(1), 51–62. https://doi.org/10.1007/s00269-018-0986-6

Watt, J. P., & Ahrens, T. J. (1983). Shock compression of single-crystal forsterite. *Journal of Geophysical Research: Solid Earth*, *88*(B11), 9500–9512. https://doi.org/10.1029/JB088iB11p09500

Watt, J. P., & Ahrens, T. J. (1986). Shock wave equation of state of enstatite. *Journal of Geophysical Research: Solid Earth*, *91*(B7), 7495–7503. https://doi.org/10.1029/JB091iB07p07495

Watt, J. P., Davies, G. F., & O'Connell, R. J. (1976). The elastic properties of composite materials. *Reviews of Geophysics*, *14*(4), 541. https://doi.org/10/drtq3z

Weber, R. C., Lin, P. Y., Garnero, E. J., Williams, Q., & Lognonné, P. (2011). Seismic detection of the lunar core. *Science*, *331*(6015), 309–312. https://doi.org/10.1126/science.1199375

Wei, S. S., & Shearer, P. M. (2017). A sporadic low-velocity layer atop the 410 km discontinuity beneath the Pacific Ocean. *Journal of Geophysical Research: Solid Earth*, *122*(7), 5144–5159. https://doi.org/10.1002/2017JB014100

Weinstein, S. A. (1995). The effects of a deep mantle endothermic phase change on the structure of thermal convection in silicate planets. *Journal of Geophysical Research: Planets*, *100*(E6), 11719–11728. https://doi.org/10.1029/95JE00710

Wenzel, M. J., Manga, M., & Jellinek, A. M. (2004). Tharsis as a consequence of Mars' dichotomy and layered mantle. *Geophysical Research Letters*, *31*(4). https://doi.org/10.1029/2003GL019306

White, W. B. (1974). The carbonate minerals. In V. C. Farmer (Ed.), The Infrared Spectra of Minerals (Vol. 4, p. 0). Mineralogical Society of Great Britain and Ireland. https://doi.org/10.1180/mono-4.12

Williams, Q., & Garnero, E. J. (1996). Seismic evidence for partial melt at the base of Earth's mantle. *Science*, *273*(5281), 1528–1530. https://doi.org/10/fwswj8

Winbo, C., Rosen, E., & Heim, M. (1998). Thermal analytical study of the decomposition of $K_2Ca(CO_3)_2$. *Acta Chemica Scandinavica*, *52*, 431–434.

Ye, Y., Smyth, J. R., & Boni, P. (2012). Crystal structure and thermal expansion of aragonite-group carbonates by single-crystal X-ray diffraction. *American Mineralogist*, *97*(4), 707–712. https://doi.org/10.2138/am.2012.3923

Yoshino, T., Nishihara, Y., & Karato, S. (2007). Complete wetting of olivine grain boundaries by a hydrous melt near the mantle transition zone. *Earth and Planetary Science Letters*, *256*(3–4), 466–472. https://doi.org/10/bqtt8k

Yuan, L., Steinle-Neumann, G., & Suzuki, A. (2020). Structure and density of H_2O-rich Mg_2SiO_4 melts at high pressure from ab-initio simulations. *Journal of Geophysical Research: Solid Earth*, *1*, 485–494. https://doi.org/10.1029/2020JB020365

Zaitsev, A. N., & Chakhmouradian, A. R. (2002). Calcite amphibole clinopyroxene rock from the Afrikanda Complex, Kola Peninsula, Russia: Mineralogy and a possible link to carbonatites. II. Oxysalt minerals. *The Canadian Mineralogist*, *40*(1), 103–120. https://doi.org/10.2113/gscanmin.40.1.103

Zaitsev, A. N., Keller, J., Spratt, J., Jeffries, T. E., & Sharygin, V. V. (2009). Chemical composition of nyerereite and gregoryite from natrocarbonatites of Oldoinyo Lengai volcano, Tanzania. *Geology of Ore Deposits*, *51*(7), 608–616. https://doi.org/10.1134/S1075701509070095

Zaranek, S. W., & Manga, M. (2007). Mantle plumes and long-lived volcanism on Mars as a result of mantle compositional layering. *38th Lunar and Planetary Science Conference*. https://www.lpi.usra.edu/meetings/lpsc2007/pdf/2133.pdf

Zeff, G., Kalkan, B., Armstrong, K., Kunz, M., & Williams, Q. (2024). High pressure raman spectroscopy and X-ray diffraction of $K_2Ca(CO_3)_2$ bütschliite: Multiple pressure-induced phase transitions in a double carbonate. *Physics and Chemistry of Minerals*, *51*(1), 2. https://doi.org/10.1007/s00269-023-01262-5

Zhang, J., & Herzberg, C. (1994). Melting experiments on anhydrous peridotite KLB-1 from 5.0 to 22.5 GPa. *Journal of Geophysical Research: Solid Earth*, *99*(B9), 17729–17742. https://doi.org/10/b2q9kq

Zhang, Y., Sekine, T., Yu, Y., He, H., Meng, C., Liu, F., & Zhang, M. (2014). Hugoniot and sound velocity of antigorite and evidence for sluggish decomposition. *Phys Chem Minerals*, *41*, 313–322. https://doi.org/10.1007/s00269-013-0650-0

Zhao, Z., Li, Z., Wang, Q., & Wang, Y. (2015). Quantum chemical study of thermal decomposition mechanism and polymorph predict phase transitions of magnesite. *Research on Chemical Intermediates*, *41*(11), 8471–8482. https://doi.org/10.1007/s11164-014-1904-2

Zhao, Z., Wang, D., Wang, Q., Li, Z., & Fang, Z. (2013). Quantum chemical study on thermal decomposition mechanism of calcium carbonate. *Journal of Theoretical and Computational Chemistry*, *12*(06), 1350049. https://doi.org/10.1142/S0219633613500491

Zharkov, V. N., & Gudkova, T. V. (2005). Construction of Martian interior model. *Solar System Research*, *39*(5), 343–373. https://doi.org/10.1007/s11208-005-0049-7

Zhuravlev, Yu. N. (2022). Vibration spectra of double K–Ca, K–Mg, and Na–Mg carbonates under pressure. *Geochemistry International*, *60*(11), 1103–1113. https://doi.org/10.1134/S0016702922110118